

KINEMATIC CONSTRAINTS ON TREMOR AND SLOW SLIP IN CASCADIA
AND IMPLICATIONS FOR FAULT PROPERTIES

by

RANDY DUANE KROGSTAD

A DISSERTATION

Presented to the Department of Geological Sciences
and the Graduate School of the University of Oregon
in partial fulfillment of the requirements
for the degree of
Doctor of Philosophy

September 2016

DISSERTATION APPROVAL PAGE

Student: Randy Duane Krogstad

Title: Kinematic Constraints on Tremor and Slow Slip in Cascadia and Implications for Fault Properties

This dissertation has been accepted and approved in partial fulfillment of the requirements for the Doctor of Philosophy degree in the Department of Geological Sciences by:

| | |
|------------------|------------------------------|
| Eugene Humphreys | Co-Chair |
| David A. Schmidt | Co-Chair |
| Ray Weldon | Core Member |
| Douglas Toomey | Core Member |
| John Conery | Institutional Representative |

and

| | |
|----------------|-----------------------------|
| Scott L. Pratt | Dean of the Graduate School |
|----------------|-----------------------------|

Original approval signatures are on file with the University of Oregon Graduate School.

Degree awarded September 2016

© 2016 Randy Duane Krogstad

DISSERTATION ABSTRACT

Randy Duane Krogstad

Doctor of Philosophy

Department of Geological Sciences

September 2016

Title: Kinematic Constraints on Tremor and Slow Slip in Cascadia and Implications for Fault Properties

Subduction zone fault processes range from tsunami-generating megathrust events to aseismic creep along the deeper portions of the fault. Episodic tremor and slow slip (ETS) represents the transition between these two regimes, where slip occurs at semi-regular recurrence intervals of months-to-years. These events are also accompanied by low frequency earthquakes, referred to as tremor. The study of ETS in Cascadia has been made possible by the enhancement of large-scale seismic and geodetic networks. In this dissertation, I use a range of geodetic and seismic observations at sub-daily to decadal time scales to investigate the kinematic behavior of individual ETS events, as well as the long-term behavior of the ETS zone and its relationship with the updip seismogenic zone.

In Cascadia, current seismic hazard maps use the ETS zone as the downdip limit of rupture during future megathrust events. In Chapter II, I utilize uplift rates derived from 80 years of leveling measurements to explore the possibility that long-term strain accumulation exists near the ETS zone. The uplift rates are consistent with a region of 10-20% locking on the updip side of the ETS zone. The lack of

associated topography indicates that the accumulated strain must be released during the megathrust cycle. The correlation of tremor and slip in Cascadia suggests there is an inherent relationship between the two. In Chapter III, I develop a method for using tremor as a proxy for slip to assess the spatial relationship of tremor and slip. I compare predictions of tremor-derived slip models to results from static inversions of GPS offsets by modeling slip based on the density of tremor. These comparisons suggest that the correlation of tremor and slip is variable along strike and along dip. In Chapter IV, I explore how borehole strainmeters can improve our resolution of slip on the plate interface. I incorporate strainmeters into joint, time-dependent kinematic inversions with GPS data. The temporal resolution of strainmeters provides improved constraints when deriving time-dependent slip estimates during slow slip events, allowing us to better image the kinematics of slow slip.

This dissertation includes previously published and unpublished material.

CURRICULUM VITAE

NAME OF AUTHOR: Randy Duane Krogstad

GRADUATE AND UNDERGRADUATE SCHOOLS ATTENDED:

University of Oregon, Eugene, OR
University of Colorado, Boulder, CO
Montana State University, Bozeman, MT

DEGREES AWARDED:

Doctor of Philosophy, Geological Sciences, 2016, University of Oregon
Masters of Arts, Philosophy, 2010, University of Colorado
Bachelor of Science, Physics, 2006, Montana State University
Bachelor of Arts, Philosophy, 2006, Montana State University

AREAS OF SPECIAL INTEREST:

Episodic Tremor and Slip, Geodesy, Subduction Zone Processes, Fault Mechanics.

PROFESSIONAL EXPERIENCE:

Graduate Teaching and Research Fellow, Department of Geological Sciences,
University of Oregon, 2009–2016

Directed Study, Department of Philosophy, University of Colorado, 2007-2010

Directed Study, Department of Physics, Montana State University, 2002-2006

Directed Study, Department of Philosophy, Montana State University, 2002-2006

GRANTS, AWARDS AND HONORS:

Graduate Teaching Fellowship, Department of Geological Sciences, University of Oregon, 2009–2016

Johnston Scholarship Travel Grant, Department of Geological Sciences,
University of Oregon, 2011, 2013, 2014

PUBLICATIONS:

- Krogstad, R. D., Schmidt, D. A., Weldon, R. J., & Burgette, R. J. (2016). Constraints on accumulated strain near the ETS zone along Cascadia. *Earth and Planetary Science Letters*, 439, 109-116.
- Neumeier, J. J., Bollinger, R. K., Timmins, G. E., Lane, C. R., Krogstad, R. D., & Macaluso, J. (2008). Capacitive-based dilatometer cell constructed of fused quartz for measuring the thermal expansion of solids. *Review of Scientific Instruments*, 79(3), 033903.

ACKNOWLEDGEMENTS

I would like to thank my advisor David Schmidt for his continuous support and guidance throughout my time as a graduate student. Thank you to my departmental committee members Ray Weldon, Gene Humphreys, and Doug Toomey for all of their time, advice, engaging scientific discussions, and providing unique perspectives on my research. Thank you to John Conery for serving as an external member of my committee and to Reed Burgette for providing additional analysis of the leveling data used in chapter 2. I would like to thank Alan Rempel for allowing me to join meetings with his research group and a special thanks to Amanda Thomas, Quentin Bletery, and Rob Skarbek for providing insights, guidance, and great discussions on all things related to fault mechanics, tremor, and slow slip.

I am grateful to have had the enduring support of my family and friends. My parents, brothers, and extended family have always supported me, even if they don't really know exactly what I do. A special thanks to all of the current and former University of Oregon graduate students, especially Angela Seligman, Al Handwerker, Kristina Walowski, and Scott Maguffin who had provided valuable scientific support, as well as countless great times together.

Continuous and campaign GPS data has been provided by the Plate Boundary Observatory (PBO), the Pacific Northwest geodetic Array (PANGA), the United States Geological Survey (USGS), and Rob McCaffrey. Leveling and tide gauge data has been provided by the National Oceanic and Atmospheric Administration (NOAA) and the National Geodetic Survey (NGS) with additional measurements and analysis from Ray Weldon and Reed Burgette. Strainmeter data is provided by PBO. Tremor

data is provided by the Pacific Northwest Seismic Network (PNSN). This work was partially supported by the USGS under USGS award number G11AP20062.

For the pursuit of knowledge, and earthquakes fast and slow.

TABLE OF CONTENTS

| Chapter | Page |
|---|------|
| I. INTRODUCTION | 1 |
| II. CONSTRAINTS ON ACCUMULATED STRAIN NEAR THE ETS ZONE ALONG CASCADIA | 6 |
| 2.1. Introduction | 6 |
| 2.2. Data and methodology | 8 |
| 2.3. Results | 16 |
| 2.4. Discussion | 21 |
| 2.5. Conclusion | 26 |
| 2.6. Bridge | 27 |
| III. ASSESSING THE SPATIAL RELATIONSHIP OF TREMOR AND SLIP IN CASCADIA USING GPS INVERSIONS, TREMOR-DERIVED SLIP MODELS, AND STRAINMETERS | 29 |
| 3.1. Introduction | 29 |
| 3.2. Methods | 33 |
| 3.3. Results | 37 |
| 3.4. Model Validation | 49 |
| 3.5. Discussion | 54 |
| 3.6. Conclusion | 68 |
| 3.7. Bridge | 69 |

| Chapter | Page |
|--|------|
| IV. EVALUATING THE SPATIAL AND TEMPORAL EVOLUTION OF SLIP DURING THE 2012 SLOW SLIP EVENT IN CASCADIA USING GPS AND STRAINMETERS | 70 |
| 4.1. Introduction | 70 |
| 4.2. Data | 73 |
| 4.3. Methods | 74 |
| 4.4. Strainmeter Error Analysis | 76 |
| 4.5. Inversion Results | 86 |
| 4.6. Discussion and Conclusion | 92 |
| V. CONCLUSIONS | 97 |
| 5.1. Dissertation Summary | 97 |
| APPENDICES | |
| A. SUPPLEMENTARY MATERIAL FOR CHAPTER II | 100 |
| A.1. Washington uplift rate analysis | 100 |
| A.2. Figures | 103 |
| A.3. Tables | 106 |
| B. SUPPLEMENTARY MATERIAL FOR CHAPTER III | 109 |
| B.1. Figures | 110 |

| Chapter | Page |
|--|------|
| C. SUPPLEMENTARY MATERIAL FOR CHAPTER IV | 124 |
| C.1. Figures | 124 |
| REFERENCES CITED | 128 |

LIST OF FIGURES

| Figure | Page |
|---|------|
| 2.1. Vertical and horizontal velocities in Cascadia used in this study. Colored dots represent absolute uplift rates from the four eastwest trending leveling profiles. Black arrows represent horizontal velocities from permanent and campaign GPS measurements. GPS velocities are relative to North America and have been corrected for the Oregon block rotation. Error ellipses are 95% confidence. Red contour lines are depths of the subducting Juan de Fuca plate beneath North America from McCrory et al. (2004). Grey arrows indicate the Juan de Fuca to fore-arc convergence rates. | 9 |
| 2.2. Expected displacement rates in central Oregon for vertical and convergence parallel deformation. Solid lines and dashed lines depict the expected velocities with and without including partial locking near the ETS zone, respectively. The depth of the locked and transitions zones are the same. The model including locking has 15% locking at a depth of 33 km. The expected signal in the vertical component is more distinctive than that expressed in the horizontal component of surface velocity. | 11 |
| 2.3. Observed and modeled uplift rates along Cascadia. Red and blue lines indicate the best-fit modeled uplift rates at each leveling benchmark with and without including locking near the ETS zone respectively. Error bars are one sigma. Grey lines are the average topography in the region of the leveling profiles. Pink shaded regions indicate the longitudinal distribution of tremor along the leveling profiles. | 14 |
| 2.4. Weighted root mean square (WRMS) misfit plotted as a function of model parameters for all four leveling profiles. (a) Depths of the locked zone and transition zone. White areas fall outside of the modeled parameter space. (b) Depth and magnitude of coupling near the ETS zone. White diamonds mark the optimal fit (lowest WRMS). The white squares on the Bandon plots represent the preferred fit to eastern most leveling benchmarks. Magenta diamonds in the upper panels mark the optimal fit of models without secondary locking. Acceptable models fall within the white contours, which encircle model parameters within the 70% confidence level of the minimum WRMS. | 15 |

| Figure | Page |
|--|------|
| 2.5. Modeled backslip rates of the four leveling profiles in relation to tremor distribution assuming secondary locking. Black lines represent the modeled backslip along each leveling profile. Light grey lines represent the range in acceptable models within a 70% confidence interval (white contours in Figure 2.4). Red lines are the distribution of tremor locations near each leveling profile. Tremor data is from the automated tremor catalog of Wech (2010) and spans Jan. 2010–Dec. 2013. The vertical axis of the tremor data (right axis) is scaled to compare the peak tremor with the locking in the ETS zone. The relatively broader tremor distribution along the Neah Bay profile is a combination of both the curved subduction zone and the actual tremor distribution. | 20 |
| 3.1. Tremor distribution in northern and central Cascadia from mid-2009 to early-2016 from Wech (2010). Black boxes highlight the major episodic tremor and slip events analyzed in this study. | 32 |
| 3.2. Trade-off of the amplitude and the area of slip ascribed to each tremor window. Dashed black line represents the average area of the model fault patches. | 37 |
| 3.3. Slip on the fault in northern Cascadia derived from static inversions of GPS offsets. Black lines contour the tremor density associated with each event. The GPS sites used in this analysis (magenta dots) and the coastline (white line) are also shown. | 39 |
| 3.4. Slip on the fault in central Cascadia derived from static inversions of GPS offsets. Black lines contour the tremor density associated with each event. The GPS sites used in this analysis (magenta dots) and the coastline (white line) are also shown. | 40 |
| 3.5. Resolution test of inversion results for northern Cascadia. A) Input slip model with maximum slip along the 37 km depth contour. Magenta dots represent GPS locations. B) Slip on the fault derived by inverting synthetic static offsets of displacement. Red bracket bounds the slip on fault patches and the tremor locations shown in part c. C) Profiles of slip with depth along the Olympic Peninsula. Grey histogram represents the tremor distribution for the 2011 event. The red line represents the input model. Red squares represent the inversion results. The blue line and squares represent the input model and results at 34 km depth. | 52 |

| Figure | Page |
|---|------|
| 3.6. Resolution test of inversion results for central Cascadia. A) Input slip model with maximum slip along the 37 km depth contour. Magenta dots represent GPS locations. B) Slip on the fault derived by inverting synthetic static offsets of displacement. The red bracket bounds the slip on fault patches and the tremor locations shown in part c. C) Profiles of slip with depth along central and northern Oregon. Grey histogram represents the tremor distribution for the 2011 event. The red line represents the input model. Red squares represent the inversion results. The blue line and squares represent the input model and results at 34 km depth. | 53 |
| 3.7. A) Relationship of total tremor occurrences (within 5-minute time windows) and seismic moment for all events. Blue triangles represent the results from static GPS inversions and red squares represent results of tremor-derived slip distributions. B) Optimal input parameters for the tremor-derived slip for all events. Red squares represent each event. Black line represents a constant seismic moment. | 54 |
| 3.8. Total WRMS misfit of the observed surface displacements and displacements predicted by tremor-derived slip models. The colored volumes show the trade-offs between the three input parameters for the tremor-derived slip distributions. The volumes enclose all parameter combinations that result in WRMS values that are within 15% of the minimum WRMS values. Black lines converge on the optimal parameters. | 58 |
| 3.9. Cumulative relationship of tremor and slip. A) The total slip associated with all major slow slip events (2009-2016) analyzed in this study as constrained by static offsets in the GPS time series. Black contours show the total tremor density associated with all of the events. Black lines highlight the areas represented in the corresponding profiles. B-D) Grey bars show histograms of cumulative tremor counts from all major events with depth along the three profiles. Red squares present slip on individual fault patches within the boundaries of the profiles indicated in (A). | 60 |

| Figure | Page |
|--|------|
| 3.10. Observed and modeled strain during multiple ETS events. Black lines show observed strain at selective strainmeter locations during the 2010 and 2012 Washington events and the 2011 and 2016 Oregon events. Colored lines show the modeled strain from the tremor-derived slip distributions. Cool colors represent strain when the slip distributions have been shifted downdip, while warm colors represent an updip shift. Center figure shows a map of all of the Cascadia strainmeter locations. The strainmeters with timeseries shown in the figure are labeled. Contours in the inset map represent the cumulative tremor density during all of the major events analyzed in this study. | 64 |
| 4.1. Power spectra for strainmeters B004 and B941. Green line shows the combine white noise and random walk fit to the spectra. The data has been detrended, and tidal and atmospheric pressure signals have been removed. | 79 |
| 4.2. Rotated strain signals during the 2012 Cascadia slow slip event. Black lines are the observed strain, warm colors have been rotated counter-clockwise in relation of original orientation, and cool colors have been rotated clockwise in relation of original orientation. | 84 |
| 4.3. Differential and engineering shear strain at B941 during the 2010 and 2012 Cascadia slow slip events. Black lines are the observed strain, red lines are strain predicted from a tremor-derived slip model, and blue dashed lines are the observed strain rotated -65° to match the orientation suggested by Hodgkinson et al. (2013). | 85 |
| 4.4. Results of the time-dependent joint inversion of GPS and strainmeter observations. Top right panels show the observed (black with 1σ uncertainties) and predicted (red) strain at strainmeters indicated on the map. Lower panel show the observed (black with 1σ uncertainties) and predicted (blue) eastern displacements at GPS stations indicated on the map. | 86 |
| 4.5. Comparison of kinematic inversions using GPS and strainmeters (A.), GPS only (B.), and a static inversion of GPS offsets (C.). Magenta squares in A. indicate strainmeters used in the inversion. Magenta circles in the B. and C. indicate GPS locations. Red lines represent slab depth contours of 30, 40, and 50 km respectively. | 87 |
| 4.6. Model sensitivity. The color of each fault element is associated with the sum of the displacements, or strains, associated with unit slip on the fault patch (Loveless and Meade, 2011). Magenta symbols represent GPS and strainmeter locations. | 88 |

| Figure | Page |
|---|------|
| 4.7. Temporal evolution of slip during the 2012 slow slip event. Colored patches indicate slip on the fault interface. Grey dots represent tremor. | 90 |
| 4.8. Observed strain at strainmeter B022 during the 2012 slow slip event. Red and blue lines represent the differential and engineering shear strain components. Black line represents daily tremor activity. Colored dots along the x-axis show the distance of the tremor from B022. Green bar highlights increase in strain during a small burst of tremor. | 92 |
| 4.9. Rate of moment release associated with the 2012 slow slip event. Black line shows the results from the joint inversion of GPS and strainmeter observations. Blue line is from a GPS-only inversion. Red line represents the daily tremor activity. | 94 |
| A.1. Modeled fit results of the leveling profiles along Cascadia treating nearby leveling benchmark errors as correlated and implementing a full covariance in the optimization. Red and green lines indicate the best-fit modeled uplift rates at each leveling benchmark with and without including locking near the ETS zone respectively. | 103 |
| A.2. Modeled fit results of the convergent parallel GPS velocities along the leveling profiles. Red and blue lines indicate the best-fit modeled velocities at each station with and without including locking near the ETS zone respectively. Error bars are one sigma. | 104 |
| A.3. Weighted root mean square (WRMS) misfit plotted as a function of model parameters for convergent parallel GPS velocities along the four leveling profiles. (a) Depths of the locked zone and transition zone. White areas fall outside of the modeled parameter space. (b) Depth and magnitude of secondary locking near the ETS zone. White diamonds mark the optimal fits. Acceptable models fall within the white contours, which encircle WRMS values within the 70% confidence level of the minimum WRMS. | 105 |
| B.1. 2009 Oregon (August). | 110 |
| B.2. 2010 Washington (August). | 111 |
| B.3. 2011 Oregon (June). | 112 |
| B.4. 2011 Washington (August). | 113 |
| B.5. 2012 Washington (September). | 114 |
| B.6. 2013 Oregon (February). | 115 |

| Figure | Page |
|--|------|
| B.7. 2013 Washington (September). | 116 |
| B.8. 2014 Oregon (October). | 117 |
| B.9. 2014 Washington (November). | 118 |
| B.10 2015 Washington (December). | 119 |
| B.11 2016 Oregon (February). | 120 |
| B.12 Checkered board resolution test. Left panel is the input model. Right panel is the inversion result following the method described in Chapter 3. Magenta dots represent GPS stations used in the inversion. | 121 |
| B.13 Checkered board resolution test. Left panel is the input model. Right panel is the inversion result following the method described in Chapter 3. Magenta dots represent GPS stations used in the inversion. | 122 |
| B.14 Contour map of slab dip angle. Red lines represent depth contours of McCrory et al. (2012). | 123 |
| C.1. Fits to strainmeter data with the joint inversion of the 2012 slow slip event not shown in figure 4.4. | 124 |
| C.2. Tremor data during the 2012 slow slip event in Cascadia. Colors represent the projected depth of tremor. Black box highlights tremor burst shown in figure 4.8. | 125 |
| C.3. Tremor data during the 2012 slow slip event. Colors represent the timing of individual tremor occurrences. Strainmeter B022 is shown in relation to tremor locations. | 126 |
| C.4. Observed strain at strainmeter B024 during the 2012 slow slip event. Red and blue lines represent the differential and engineering shear strain components. Black line represents daily tremor activity. Colored dots along the x-axis show the distance of the tremor from B024. Green bar highlights increase in strain during a small burst of tremor. | 127 |

LIST OF TABLES

| Table | Page |
|--|------|
| 2.1. Optimal model fits of the leveling data with and without including locking near the ETS zone. # The Bandon profile is better fit with no secondary locking. The secondary locking values are included to show that 5% secondary locking provides a statistically similar fit. * Results are at the edge of the modeled parameter space. \$ Midpoint depth of Gaussian secondary locking distribution. ^ Statistical significance is calculated using an F-test. | 19 |
| 3.1. Event Parameters | 41 |
| 4.1. White noise and random walk values. | 80 |
| A.1. Comparison of results assuming uncorrelated errors associated with the leveling data with results based assuming correlated errors. | 106 |
| A.2. Model fits of the GPS data with and without including locking near the ETS zone. # The Astoria profile is better fit with no secondary locking. The secondary locking values are included to show that 10% secondary locking provides a statistically similar fit. * Results are at the edge of the modeled parameter space. \$ Midpoint depth of Gaussian secondary locking distribution. ^ Statistical significance is calculated using an F-test. | 107 |
| A.3. Northern Washington uplift rates. | 108 |

CHAPTER I

INTRODUCTION

The recent proliferation of seismic and geodetic networks around the world has revealed modes of tectonic deformation that were previously undetectable. The discovery of slow slip along subduction zones was made possible by continuous geodetic monitoring that revealed periodic transient reversals of surface displacements opposite the direction of convergence (Hirose et al., 1999; Dragert et al., 2001). The observation of slow slip, and the often associated non-volcanic tremor (Obara, 2002; Rogers and Dragert, 2003), has served to provide insights into the details of subduction zone processes, as well as the behavior of faults in general (Schwartz and Rokosky, 2007). The work presented here uses a multitude of different geodetic and seismic observations to address the slip kinematics in the ETS zone (20-50 km depth on the plate interface), which includes the long-term behavior of how strain accumulates and the short-term strain release in the form of slow slip events in Cascadia. In Chapter II, I investigate the potential for long-term strain accumulation near the region of slow slip. Chapter III focuses on the spatial relationship of tremor and slow slip during several recent slow slip events in northern and central Cascadia. Finally, in Chapter IV, I utilize observations from highly sensitive borehole strainmeters to investigate the rupture kinematics of the 2012 slow slip event in northern Cascadia.

Slip transients have received invigorated interest over the past decade given that slow slip releases significant strain on subduction plate boundaries, and that these events could potentially interact the seismogenic zone. Recent observations have identified slow slip events prior to the 2011 Tohoku earthquake in Japan (Kato et al.,

2012; Ito et al., 2013; Uchida and Matsuzawa, 2013) and the 2014 Iquique earthquake in Chile (Ruiz et al., 2014; Kato and Nakagawa, 2014). Slow slip has also been observed to affect rates of background seismicity in the Hikuarangi subduction zone in New Zealand (Delahaye et al., 2009), Cascadia (Vidale et al., 2011), Ecuador (Vallee et al., 2013), and the Boso area of Japan (Reverso et al., 2016). These observations underscore the importance of understanding the relationship of slow slip and the seismogenic zone, which is ultimately vital to understanding future geologic hazards.

The Cascadian subduction zone is sustained by the subduction of the oceanic Juan de Fuca plate beneath the continental North American plate. The along-dip component of the fault is characterized by an updip seismogenically locked zone that ruptures during large tsunami-generating megathrust events with recurrence intervals of approximately 250-600 years (Goldfinger et al., 2003). A transition zone occurs downdip of the locked zone where the fault is recognized as transitioning from being fully locked to partially coupled. The recently discovered episodic tremor and slip (ETS) zone is located at the downdip extent of the transition zone near the Moho (~ 35 km depth). Major ETS events represent large-scale (M_w 6-7) aseismic slip events that are concurrent with tremor and low frequency earthquakes (LFEs), inferred to be the seismic rupture of small-scale (10-1000s of meters) asperities (Beroza and Ide, 2011). ETS events propagate along strike at velocities of ~ 10 km/day and are confined to depths of 25-50 km on the fault interface. The recurrence interval for ETS events varies along strike, and ranges from ~ 10 months along the southern portion of the fault to ~ 20 months under central Oregon (Brudzinski and Allen, 2007).

The observation of ETS has revealed that brittle deformation can exist at depths along the subduction zone that are deeper than the brittle-ductile transition for silica-based rocks. Current seismic hazard maps use the along-dip location of the ETS zone

to delineate the downdip extent of rupture during future megathrust events. These rupture models are based on the assumption that no long-term strain is accumulated near the ETS zone. In Chapter II, I test this assumption by utilizing leveling data that has been collected over the last ~ 80 years as well as more recent GPS observations. When tied to an absolute reference frame through the use of tide gauges, leveling measurements provide precise uplift rates that can then be used to infer locking along the subduction zone. The four east-west leveling profiles in Oregon and northern Washington all exhibit a small increase in uplift at longitudes consistent with partial locking near the ETS zone. These uplift rates are then used to constrain the extent of possible locking near the ETS zone. All four profiles are consistent with up to 10-20% locking in regions slightly updip of the ETS zone, although only one profile is deemed statistically significant.

The apparent spatial and temporal correlation of tremor and slow slip in Cascadia and Japan has led to the establishment of scaling relationships that relate the duration of observed tremor to the moment release associated with slow slip events (Ide et al., 2007; Aguiar et al., 2009). Additionally, recent geodetic inversions of slow slip have suggested that slip may potentially extend beyond the extent of tremor both along-dip and along-strike in Cascadia (Dragert and Wang, 2011; Wech and Bartlow, 2014). In Chapter III, I use geodetic and seismic observations from all the major ETS events in central and northern Cascadia from 2009-2016 to investigate the spatial relationship of tremor and slip and to evaluate whether these two processes are really coincident at all scales. In order to facilitate a more direct comparison of tremor and slip, and to assess the reliability of the proposed scaling relationships, I develop a method for using tremor observations as a proxy for slip on the fault interface. Forward models from the tremor-derived slip distributions are then compared to inversions of static

GPS offsets and limited strainmeter observations. These comparisons indicate that the correlation of tremor and slip is variable along strike, with some regions showing a strong relationship between the location and density of tremor with slip, while other regions exhibit a weak correlation between the two.

The recent deployment of a network of borehole strainmeters in Cascadia provides a unique and independent geodetic observation for characterizing slow slip. The sensitivity and precision associated with these instruments provide an observational bridge between the high-rate measurements of seismometers and the long-term stability of GPS. Due to their sensitivity, these strainmeters are also highly susceptible to non-tectonic artifacts in the data. The design of the instruments requires that they be calibrated with known external sources of strain – typically from modeled tidal stresses. Recent studies have suggested that this calibration process can be prone to error and that the magnitude of observed strain transients can vary by up 30% depending on how the instrument is calibrated (Langbein, 2010).

The use of strainmeters to study slow slip has previously been restricted to detecting the occurrence of strain changes during ETS activity and comparisons with forward models (Wang et al., 2008; Dragert and Wang, 2011; Hawthorne and Rubin, 2010, 2013; Wech and Bartlow, 2014). In Chapter IV, I demonstrate, for the first time, that strainmeter and GPS data can be combined together in a joint, time dependent inversion for slow slip. I provide a full error analysis of the strain data to properly characterize the overall uncertainty of strain transients over the time scales associated with slow slip events. This enables the strain data to be combined with GPS data to perform joint time-dependent inversions. Although the spatial coverage of the strainmeter network is limited, the temporal resolution of the strain data provides an improved temporal constraint to the propagation of slip compared

to GPS-only inversions. Both the joint and the GPS-only inversions reveal some systematic differences from the tremor propagation during the 2012 slow slip event in northern Cascadia. However, the joint inversion results indicate a stronger correlation with the tremor than the GPS-only results.

This work covers methods for characterizing uncertainty in a variety of geodetic data and develops new methods for constraining the kinematic behavior of slow slip in Cascadia. Currently, each chapter is in a different stage of the publication process. Chapter I has been published in *Earth and Planetary Science Letters* and was co-authored with David Schmidt, Ray Weldon, and Reed Burgette. Chapter II is in preparation for submission to the *Journal of Geophysical Research* and is co-authored with David Schmidt. Chapter III is in preparation for *Geophysical Research Letters* and is also co-authored with David Schmidt.

CHAPTER II

CONSTRAINTS ON ACCUMULATED STRAIN NEAR THE ETS ZONE ALONG CASCADIA

Published as: Krogstad, R. D., Schmidt, D. A., Weldon, R. J., and Burgette, R. J. (2016). Constraints on accumulated strain near the ETS zone along Cascadia. *Earth and Planetary Science Letters*, 439, 109-116. As lead author, I wrote the manuscript, performed all of the analysis and interpretation, and drafted all the figures for this chapter. My co-authors, Schmidt, Weldon, and Burgette helped me with editorial assistance and the interpretation of my results.

2.1. Introduction

The Cascadia subduction zone poses a significant seismic hazard to the Pacific Northwest due to the potential of a megathrust earthquake (Atwater, 1987; Goldfinger et al., 2003). Geodetic and thermal data suggest that strain is actively accumulating along the plate boundary (Hyndman and Wang, 1995). Seismic hazard maps that quantify the expected strong motion from a megathrust event are constructed from a logic tree of rupture scenarios. One branch of these rupture scenarios implicitly assumes that seismic rupture will not extend into the zone of episodic tremor and slip (ETS) (Petersen et al., 2014). Considering the importance that this assumption has on the seismic hazard, we explore the potential for long-term strain accumulation near the ETS zone.

In Cascadia, ETS events represent the transient release of accumulated strain along the plate interface downdip from the seismogenically locked zone at 25-45 km depth. These \sim Mw 6 ETS events last approximately 10-20 days and have recurrence

intervals of 11-22 months (Dragert et al., 2001; Rogers and Dragert, 2003; Brudzinski and Allen, 2007; Schmidt and Gao, 2010). The existence of ETS demonstrates that the subducting and overriding plates are capable of storing strain at this depth for months to years, and perhaps longer. The limited resolution of slip on the deep part of the plate interface leaves considerable uncertainty as to whether any strain might accumulate over multiple ETS cycles near the ETS zone, thereby potentially elevating the seismic hazard by increasing the down-dip limit of the seismogenic locked zone and extending the rupture zone inland toward large population centers.

Geodetic inversions of major slow slip events (SSEs) in north-west Washington from 1997-2008 reveal that only 50-60% of the long-term strain accumulation is released at 25-45 km depth (Chapman and Melbourne, 2009; Schmidt and Gao, 2010). Smaller SSEs, which are difficult to resolve geodetically, may account for the remaining slip deficit within the ETS zone. Based on tremor that accompanies slow slip, Wech et al. (2009) inferred that up to 45% of the strain budget might be attributed to background activity in the inter-ETS interval. This would suggest that nearly the entire strain budget that is accumulated around the plate boundary within the depth interval of \sim 25-45 km is released in ETS activity. In contrast, rate-and-state numerical models of SSEs have predicted that a sizable portion (\sim 30-50%) of the slip deficit remains after multiple events (Segall et al., 2010; Colella et al., 2013).

In this work, we investigate the presence of elastic strain that is accumulated within the depth range of 25-45km on the plate boundary and released during a typical megathrust cycle through the optimization of locking parameters. Although the kinematic behavior of ETS has predominately been characterized using geodetic (i.e. GPS and strain gauges) and seismic measurements (i.e. tremor) from the last 1-2 decades, historical leveling and tide gauge data, which extend back nearly 8

decades, provide a means to supplement and extend these recent observations to gain a better understanding of long-term deformation in the ETS zone. When tied to an absolute reference frame with tide gauge data, leveling data provide precise uplift measurements with uncertainties significantly lower than current vertical GPS measurements. Our findings suggest that the long term accumulated strain is less than predicted by some numerical models, but the data do allow for a small portion of the slip budget to be stored over multiple ETS cycles.

2.2. Data and methodology

For this study, the vertical displacements of four east-west leveling profiles along Cascadia are analyzed: three in Oregon (Burgette et al., 2009), and one in northern Washington reprocessed with a similar methodology (Fig.1; Supplementary Text A1). Relative uplift rates are derived from National Geodetic Survey (NGS) first- and second-order leveling surveys along highways in western Oregon and Washington, spanning a time-scale from the early 1930s to the late 1980s. Burgette et al. (2009) estimated up to 80 years worth of uplift rates along the surveys in Cascadia by making secondary ties to benchmarks, correcting for sea level rise rates, and improving the data processing.

Each leveling profile is tied to benchmarks at tide gauge stations. After accounting for regional sea level rise, the tide gauge uplift rates are used to provide an absolute reference frame to the relative uplift rates from the leveling profiles. This, along with additional processing methods, helps to significantly reduce the standard error of benchmark uplift rates to $\sim 0.3 \text{ mma}^{-1}$ along the coast, with the error increasing to the east away from the tide gauge benchmarks to $\sim 1 \text{ mma}^{-1}$. Refer to Burgette et al. (2009) and the supplement for the complete details of the

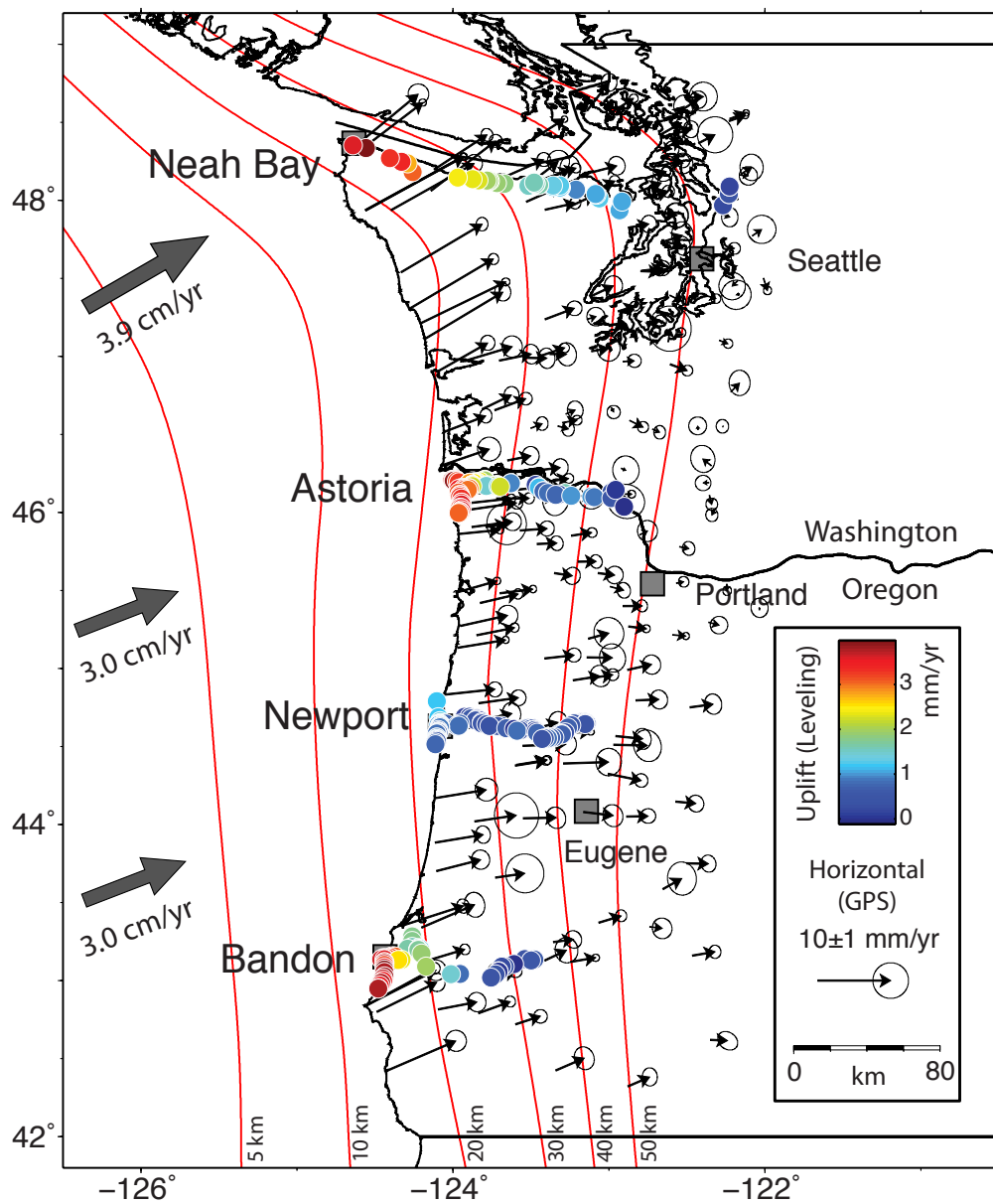


FIGURE 2.1. Vertical and horizontal velocities in Cascadia used in this study. Colored dots represent absolute uplift rates from the four eastwest trending leveling profiles. Black arrows represent horizontal velocities from permanent and campaign GPS measurements. GPS velocities are relative to North America and have been corrected for the Oregon block rotation. Error ellipses are 95% confidence. Red contour lines are depths of the subducting Juan de Fuca plate beneath North America from McCrory et al. (2004). Grey arrows indicate the Juan de Fuca to fore-arc convergence rates.

processing procedure. We have greater trust in data points with higher uplift rates, since individual benchmarks tend to subside over time and can be biased downward. However, all reported data are used in our analysis.

To complement the leveling results we also include an analysis of GPS displacements near the leveling profiles. Due to higher uncertainties and scatter in the vertical component of GPS compared to our leveling data set, we choose to only use the horizontal GPS components. We use network site velocities in Cascadia from continuous and campaign GPS observations compiled, analyzed, and made available by McCaffrey et al. (2013), which includes data from the Plate Boundary Observatory, Pacific Northwest Geodetic Array, Western Canada Deformation Array, National Geodetic Survey Continuously Operating Reference Sites, and several others. The velocities are restricted to sites with at least five years of data, and are spatially binned to coincide with the leveling profiles. Sites near major volcanic centers are removed. The rotation of Oregon and southern Washington is removed using the pole and rate of rotation derived by McCaffrey et al. (2013). The north and east oriented velocity vectors are rotated into convergence normal and convergence parallel components. This allows us to focus on the convergence parallel component, where the maximum deformation signal is observed.

Time-dependent deformation along the fault since the last major rupture (i.e. viscous relaxation of the lower crust or upper mantle) could affect the GPS and leveling data differently. Considering our model assumes an isotropic elastic medium, we do not explore how the deformation might evolve with time. Due to the difference in averaging intervals and the relative difficulty of resolving the expected signal due to secondary locking in horizontal displacements (Fig. 2) the leveling and GPS datasets are analyzed individually.

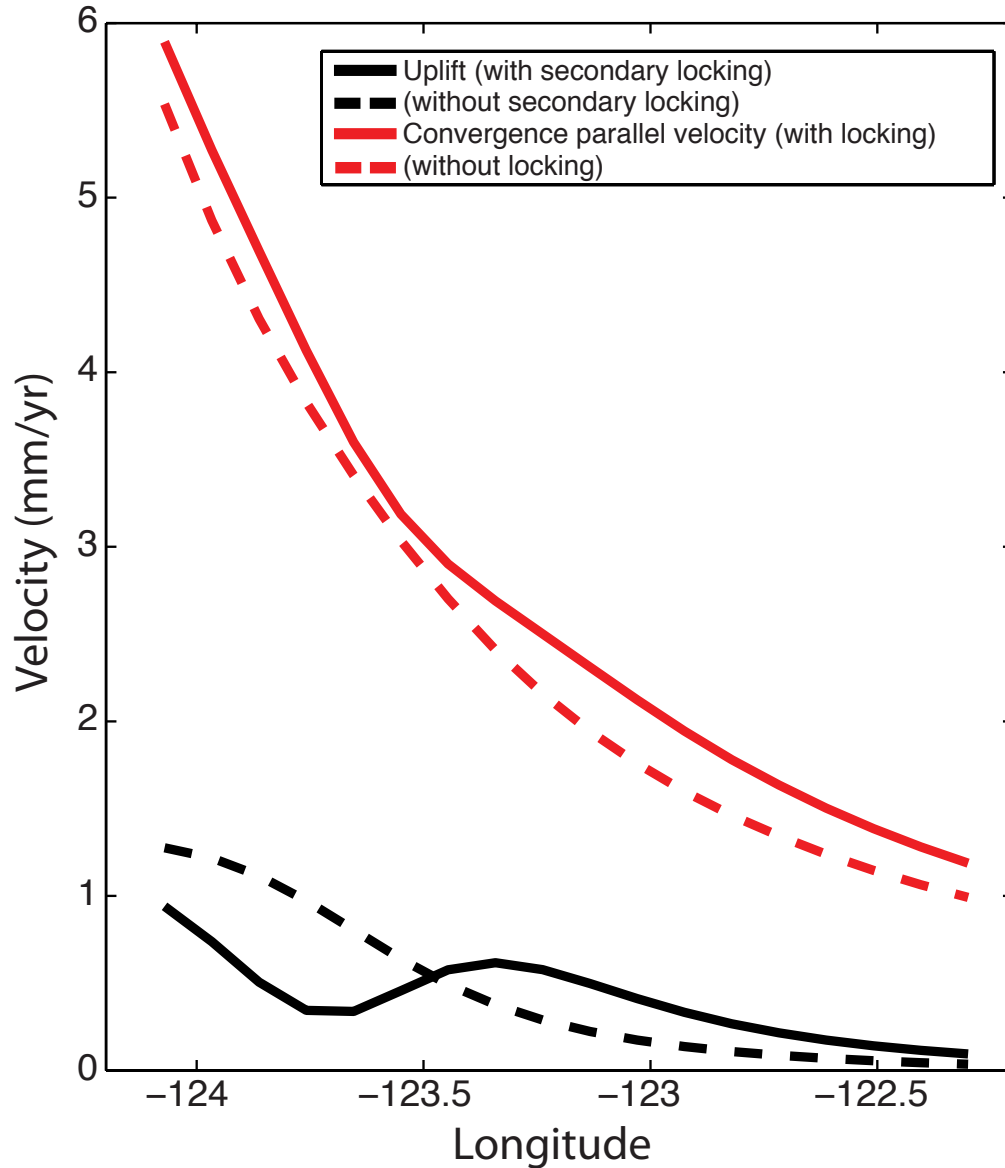


FIGURE 2.2. Expected displacement rates in central Oregon for vertical and convergence parallel deformation. Solid lines and dashed lines depict the expected velocities with and without including partial locking near the ETS zone, respectively. The depth of the locked and transitions zones are the same. The model including locking has 15% locking at a depth of 33 km. The expected signal in the vertical component is more distinctive than that expressed in the horizontal component of surface velocity.

To model the subduction zone, a backslip method is used to estimate the slip deficit on the subduction interface (Savage et al., 2000). The convergence rate is calculated using the Juan de Fuca-Oregon forearc Euler pole of Wells and Simpson (2001) for the Oregon profiles and the Juan de Fuca-North America pole of Mazzotti et al. (2007) for the Washington profile. The Juan de Fuca slab interface is modeled by discretizing the depth contours of McCrory et al. (2004) into triangular subfault patches. Surface deformation is estimated using an isotropic elastic half space with a Poisson's ratio of 0.25 and a shear modulus of 40 GPa. Greens functions are calculated using the boundary element program Poly3D (Thomas, 1993). Slip is ascribed using a combination of dip-slip and strike-slip motion to account for oblique convergence of the Juan de Fuca plate with North America. The slip deficit along the plate interface is prescribed by four free parameters: the down-dip extent of the primary seismogenic zone (locked zone), the down-dip extent of the transition zone, and a zone of partial locking near the ETS zone (also referred to as the zone of secondary locking) where the location and magnitude of the locking are allowed to vary separately.

The slip deficit rate in the seismogenically locked zone is assumed to be the full convergence rate and fully locked to the trench. Although this assumption may not hold true, our model results are insensitive to the extent of locking near the trench given that all of our observations are onshore. In the transition zone, the slip deficit rate decays exponentially from the full convergence rate to zero as described by Wang et al. (2003). We parameterize the slip deficit function near the ETS zone as a Gaussian distribution of partial locking with a 1-sigma along-dip width of 2 km. The magnitude of coupling and the location of the peak of the Gaussian are allowed to vary. This distribution of strain accumulation was chosen to correspond with the general shape of observed tremor density (Wech and Creager, 2011). A sensitivity

analysis revealed that the model results for depth and magnitude of the secondary coupling are relatively insensitive to the prescribed shape (i.e. triangular, Gaussian, or boxcar).

An iterative procedure is run to explore the full model parameter space. We consider locked zone depths ranging from 5 to 25 km, transition zone depths of 10-40 km, peak ETS zone locking depths of 25-40 km, and peak ETS zone locking of 0-40%. We forward predict the surface displacements and evaluate the goodness of fit by calculating the weighted root mean square (WRMS) using the data uncertainties for each iteration of the model parameters (Fig.3). Misfit plots show the WRMS as a function of the model parameters (Fig.4). Given that a range of model parameters produce a low WRMS, we use a t-test and consider all models within a 70% confidence interval from the model that produces the minimum WRMS to be statistically indistinguishable. Additionally, we consider models that both include and exclude a zone of secondary locking; an F-test is used to evaluate whether the increase in model parameters provides a statistically significant improvement in the WRMS values.

The WRMS approach assumes that the leveling data is composed of independent observations. However, leveling data is known to contain spatially correlated errors that propagate along leveling lines. To compare the effects of different error models, we also use the approach described in Pollitz et al. (1998) where the covariance matrix is formulated as a combination of measurement and non-measurement error. Measurement error is correlated and dependent on the distance between neighboring benchmarks, while non-measurement errors are uncorrelated and can come from many different sources (e.g. soil compaction) (Amoruso and Crescentini, 2007). The measurement error is accounted for using the method of Arndottir et al. (1992) where the covariance matrix is of a form that treats the differences of the benchmark-to-

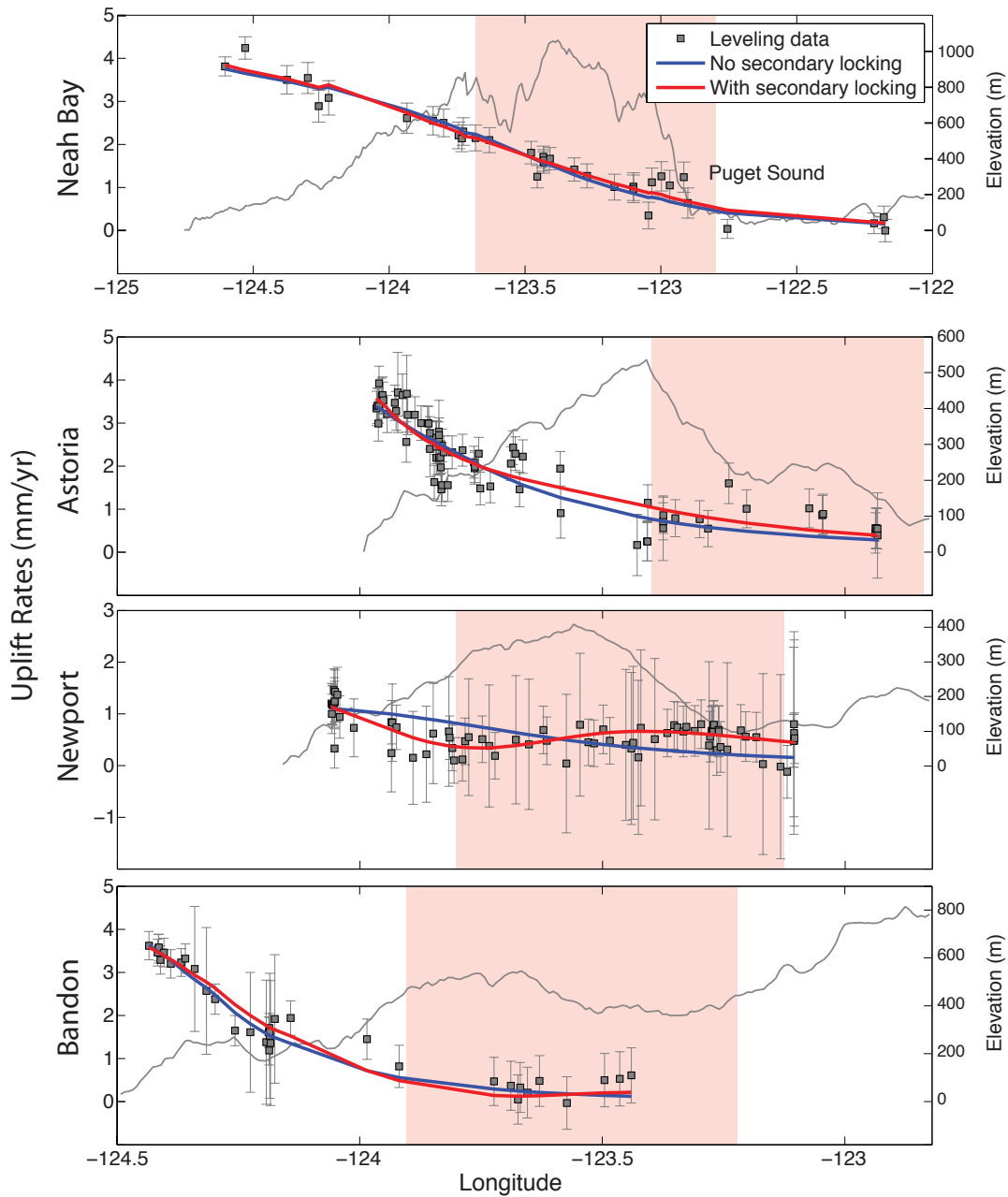


FIGURE 2.3. Observed and modeled uplift rates along Cascadia. Red and blue lines indicate the best-fit modeled uplift rates at each leveling benchmark with and without including locking near the ETS zone respectively. Error bars are one sigma. Grey lines are the average topography in the region of the leveling profiles. Pink shaded regions indicate the longitudinal distribution of tremor along the leveling profiles.

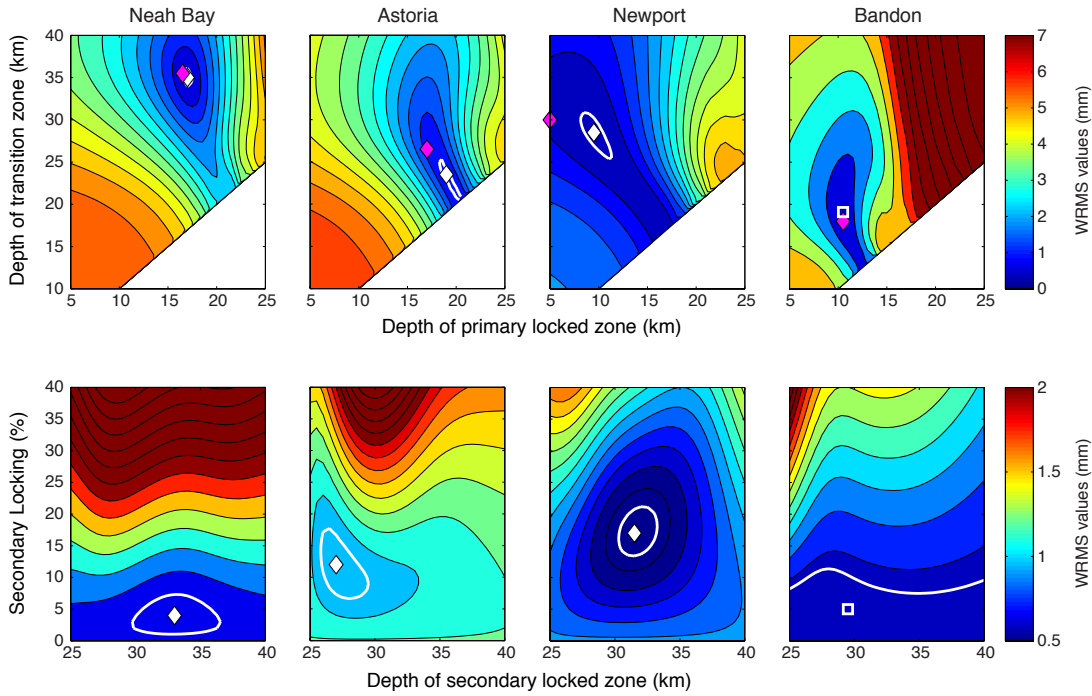


FIGURE 2.4. Weighted root mean square (WRMS) misfit plotted as a function of model parameters for all four leveling profiles. (a) Depths of the locked zone and transition zone. White areas fall outside of the modeled parameter space. (b) Depth and magnitude of coupling near the ETS zone. White diamonds mark the optimal fit (lowest WRMS). The white squares on the Bandon plots represent the preferred fit to eastern most leveling benchmarks. Magenta diamonds in the upper panels mark the optimal fit of models without secondary locking. Acceptable models fall within the white contours, which encircle model parameters within the 70% confidence level of the minimum WRMS.

benchmark heights as being measured directly. This allows for the data to be treated as independent and uncorrelated. This approach strongly weights spatially clustered benchmarks and is particularly sensitive to steep localized gradients in the uplift profile. To account for the non-measurement error, Pollitz et al. (1998) include an additional general error term of 0.5 mm/yr that is meant to account for the long-period noise levels found in vertical measurements, as described by Wyatt (1989). From this, we construct a covariance matrix that includes off-diagonal terms in the weighting matrix. The results of these two error model approaches are compared in the following section.

2.3. Results

2.3.1. Leveling Analysis

The Neah Bay, Astoria, and Newport profiles all exhibit a reduction in the WRMS when a secondary locked zone is included near the ETS zone. However, the Newport profile is the only one that provides a statistically significant improvement in WRMS values. The leveling data extending from Bandon, Oregon is the only profile that is best fit without secondary locking. Based on the 70% confidence interval limit for acceptable models described in the methods section, acceptable models show a maximum secondary locking in the range of 10-20% (Fig. 4).

The best-fit models for the Neah Bay profile have a peak locking of $\sim 5\%$ located at 33-35 km depth (Fig. 3 and 4). The eastern side of the northern Washington leveling profile has a gap where it crosses Puget Sound. The points directly west of the Puget Sound gap (longitude of $\sim 123^\circ$) show a subtle leveling-off of uplift rates, which diverges from the linear eastward trend in decreasing uplift rates observed in the western portion of the profile. A model that includes locking in the ETS zone

better fits these points on the western edge of Puget Sound, but the lack of data within the Sound makes quantifying the precise magnitude of the locking difficult.

The best-fit models for Astoria have a peak secondary locking of 5–15% located at 28–33 km depth. The high uplift values at $\sim 123.2^\circ$ are under-fit by these models because of the significantly more abundant data points on the western end of the profile (Fig. 3 and 4). We can improve the fit of the data on the eastern end of the profile by manually shifting the peak of the coupling in the ETS zone to 34 km depth and increasing the locking to 20% at a cost of $\sim 9\%$ increase in the overall WRMS for the entire dataset.

The Newport profile is statistically better fit when locking near the ETS zone is included, as indicated by an F-test. The secondary uplift is very distinct, and the relatively more dense data sampling on the eastern end of the profile compared to other profiles allows us to better constrain the locking near the ETS zone. The diminished coastal uplift suggests that the locked zone is far offshore, or is only partially locked. This leads to uncertainty in the amount of locking in the primary locked zone, as evidenced by the relatively broad misfit field in Figure 4. Decreasing the locking in the seismogenically locked zone to 50% would extend the locked zone to a depth of 16 km and would be accompanied by a similar transition zone depth of 30 km. Regardless of how locking is assigned in the primary locked zone, the secondary uplift signature is still best fit with secondary locking at approximately 32–35 km depth with 15–25% locking.

The Bandon profile is best fit with little to no locking near the ETS zone. However, the eastern most extent of the Bandon profile ends in the region where the secondary uplift is observed in the other two Oregon profiles. The easternmost points on the profile show an increasing uplift trend. Since these few points have

a minimal impact on the overall fit of the profile, the optimized parameters do not adequately fit these eastern points. When a forward model is forced to fit the eastern most points, the results indicate secondary locking at 28–32 km depth with 5–10% locking, although this leads to some systematic misfits of the data directly west of the secondary uplift. This procedure raises the WRMS by $\sim 9\%$ compared to the optimal model with no coupling. Alternatively, increasing the locking gradient of the transition zone can better fit the eastern data without adversely affecting the fit of the western data. While models with steep transition zones result in similar locked zone and secondary locking depths, the transition zone extends significantly deeper to $\sim 30\text{--}35$ km.

The results using the full covariance matrix (Table A1 and Fig. A1) provide a close match with the results assuming independent data for each benchmark. We find that the differences between the two sets of model results are insignificant at the 90% confidence interval for all of the profiles except Bandon. The Astoria profile has the largest difference in optimal secondary locking values, with an increase of 15% when using the full covariance matrix. Additionally, the best-fit locked and transition zones depths for Astoria are likely physically unrealistic, with both being located at 21 km. This method works well for leveling profiles that have approximately evenly spaced benchmarks such as the Neah Bay and Newport profiles. However, the Astoria and Bandon profiles have many closely spaced benchmarks near the coast and relatively few distantly spaced benchmarks extending inland, which results in a much lower weighting of the eastern most data where the largest signal from the secondary locking would be expected. Thus the heterogeneous sampling along the Astoria profile may explain why the results differ between the two weighting schemes. This optimization using the full covariance is also more sensitive to outliers that create steep gradients

| Leveling Results | Neah Bay | Astoria | Newport | Bandon [#] |
|--|----------|---------|---------|---------------------|
| No Locking in ETS zone | | | | |
| Locked zone depth (km) | 16.5 | 17 | 5* | 10.5 |
| Transition zone depth (km) | 35.5 | 26.5 | 30 | 18 |
| WRMS (mm/yr) | 0.85 | 1.02 | 0.7 | 0.57 |
| Including Locking in ETS zone | | | | |
| Locked zone depth (km) | 17 | 19 | 9.5 | 10.5 |
| Transition zone depth (km) | 35 | 23.5 | 28.5 | 19 |
| Optimal ETS zone locking (%) | 4 | 12 | 17 | 5 |
| Depth [§] of ETS zone locking (km) | 33 | 27 | 31.5 | 29.5 |
| WRMS (mm/yr) | 0.8 | 0.96 | 0.41 | 0.62 |
| Statistically Significant [^] (90%) | No | No | Yes | na |

TABLE 2.1. Optimal model fits of the leveling data with and without including locking near the ETS zone.

[#] The Bandon profile is better fit with no secondary locking. The secondary locking values are included to show that 5% secondary locking provides a statistically similar fit.

* Results are at the edge of the modeled parameter space.

[§] Midpoint depth of Gaussian secondary locking distribution.

[^] Statistical significance is calculated using an F-test.

in the uplift profile. All of the Cascadia profiles contain outliers that are likely due to localized non-tectonic subsidence, which affect the overall fit to varying degrees depending on the location of the neighboring benchmarks. Although this approach better accounts for the correlated nature of leveling data and is suitable for profiles such as Neah Bay and Newport, we have found that it may not be appropriate for characterizing the secondary locking in the Astoria and Bandon profiles. (See Table 2.1)

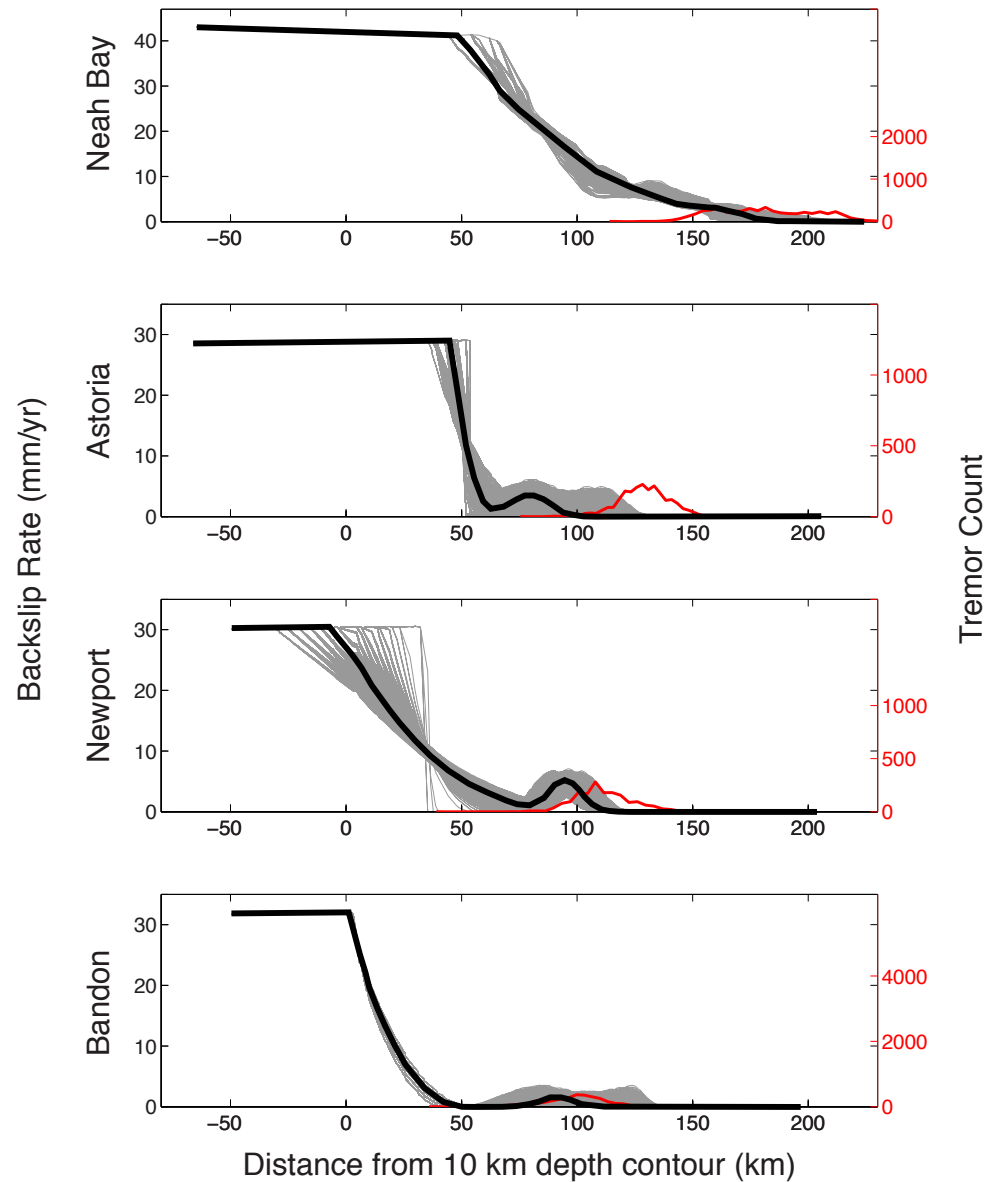


FIGURE 2.5. Modeled backslip rates of the four leveling profiles in relation to tremor distribution assuming secondary locking. Black lines represent the modeled backslip along each leveling profile. Light grey lines represent the range in acceptable models within a 70% confidence interval (white contours in Figure 2.4). Red lines are the distribution of tremor locations near each leveling profile. Tremor data is from the automated tremor catalog of Wech (2010) and spans Jan. 2010–Dec. 2013. The vertical axis of the tremor data (right axis) is scaled to compare the peak tremor with the locking in the ETS zone. The relatively broader tremor distribution along the Neah Bay profile is a combination of both the curved subduction zone and the actual tremor distribution.

2.3.2. GPS Analysis

The subtle change in the horizontal surface deformation due to a secondary locked zone makes detection difficult with current GPS data, when considering the signal-to-noise (Fig. 2). As can be seen with the Neah Bay profile in particular, a model containing a moderate ($\sim 10\text{--}15\%$) amount of coupling near the ETS zone does not provide a significantly different fit to the data (Table A2). For all the profiles, except Newport, the GPS results have a shallower seismogenically locked zone than the leveling results. This could, in part, be due to the fact that the GPS and leveling data are averaged over different time intervals, and are thus disproportionately affected by viscoelastic effects. The best-fit Newport and Bandon profiles have especially shallow locked zones, although models that have deeper locked zones and shallower transition zones can adequately fit the data as well (Fig. A2 and A3). The relatively short averaging interval of the GPS data, which covers a limited number of ETS cycles, might also affect the modeled long-term coupling in the ETS zone. For example, if a site velocity is derived using an averaging interval of 6 years and the ETS cycle is ~ 18 months the modeled results could show up to a 40% long-term strain accumulation in the ETS zone even if there is no long-term strain in that region. This likely explains why some GPS profiles have higher coupling ratios near the ETS zone compared to the leveling results. The location of the modeled peak coupling tends to match fairly well with the leveling results, although the coupling in the Neah Bay profile is best fit a few kilometers farther updip.

2.4. Discussion

We find supportive evidence for secondary locking along the Newport leveling profile. While the leveling profile near Bandon shows a small increase in WRMS

values when secondary locking is included, the profiles near Neah Bay and Astoria show an overall improvement with the addition of secondary locking. For these three profiles, models with or without a small amount of secondary locking are statistically indistinguishable, and thus we cannot rule out models with a limited amount of long-term strain accumulation near the ETS zone.

If long-term secondary locking exists within the ETS zone, our analysis suggests it is only a small fraction of the plate rate. The leveling data can be adequately fit with models that range from virtually no long-term locking, to models with an upper bound of about 20% of the plate rate. Chapman and Melbourne (2009) found that up to 15% percent locking might persist below 25 km depth when using the ETS zone to constrain the downdip extent of the transition zone in northern Washington. These results are compatible with the findings of Holtkamp and Brudzinski (2010) who analyzed long-term and transient signals in the GPS timeseries. A few studies have also explored interseismic locking models with variable locking along dip, and they inferred a double locked zone, suggestive of a primary and secondary locked zone (McCaffrey et al., 2000; Verdonck, 2005). Thus, the existence of a secondary locked zone would be broadly consistent among these previous geodetic studies.

Secondary locking is expected to produce a broad, interior uplift signal, as illustrated by the forward model in Figure 2. This interior uplift is most evident in the Newport leveling profile. However, the interior uplift may be difficult to identify in the other profiles either because it is masked by the primary locking signal from the seismogenic zone (i.e. Neah Bay profile), or because of insufficient data coverage to the east (i.e. Bandon profile). There are other possible explanations for this interior rise in the leveling data. It could represent a long wavelength artifact originating from the propagation of errors along the leveling line. Our error analysis is designed

to compensate for this, as uncertainties increase along the leveling line and we explore the impact of spatially correlated data. We also see hints of an upward interior uplift for the Astoria profile, which should be independent from the Newport profile.

If we assume that 0-20% long-term strain is accumulating in the ETS zone, then we propose that this strain must be released at some point in the megathrust earthquake cycle. It is possible that this locking signal originates from some other tectonic process. For example, the underplating of sediment beneath the forearc, or vertical uplift by a buoyant mantle wedge could result in a subtle uplift of the forearc. However, these processes would produce long-term uplift that would result in elevated topography if the uplift persists over geological time scales. The broad uplift evident in the Newport profile is spatially offset from the topography of the coast range (Fig. 3). Thus, we conclude that the secondary strain accumulation, if present, must be an elastic process. What is unknown is when during the megathrust earthquake cycle this accumulated strain would be released, and whether it is released aseismically.

The small component of long-term locking modeled at all four profiles appears to be shifted relative to the peak tremor activity. The approximate large-scale relationship between SSEs and tremor activity in Casacadia has been shown to correlate well both spatially and temporally, although inferences from geodetic observations in northern Washington tend to locate slip slightly updip of the peak tremor activity (Wang et al., 2008; Wech et al., 2009; Dragert and Wang, 2011; Bartlow et al., 2011). When the distribution of tremor is plotted with the modeled backslip profiles of the leveling data assuming secondary locking, the peak locking in the ETS zone is also located slightly updip of the peak tremor activity, placing the locking near the geodetically inferred slow slip (Fig. 5).

While there are tradeoffs in the locking parameters for the seismogenic zone, we find that the magnitude of the secondary locking in the ETS zone is generally insensitive to the amount of up-dip locking. McCaffrey et al. (2013) noted that it is possible to satisfy the surface deformation data in Oregon if maximum locking is reduced in the seismogenic zone. The assumption that the slip deficit rate in the seismogenically locked zone equals the full convergence rate does affect the depth of the locked zone and transition zone in our results. For example, the Astoria leveling profile can be fit reasonably well with levels of locking down to 70% on the updip portion of the interface, while the Newport profile can be reasonably fit with locking as low as 50% in the primary locked zone. However, the degree of locking in the seismogenic zone only has a minor effect on the amount of partial locking near the ETS zone. Additionally, the use of a heterogeneous elastic model, or a model that incorporates viscoelastic effects, may also help reduce the over WRMS values (Williams and Wallace, 2015; Wang et al., 2001). However, it is unlikely that the use of these models would affect the overall findings shown here.

One important additional relationship to note is that when the primary locked zone is assumed to be fully locked, models that include secondary locking tend to have modeled locked zones that are slightly deeper and shifted to the east. The difference in locked zone depths is typically only 1-2 km, but considering the seismic hazard imposed by the depth of the locked zone, this may be an important consideration for future seismic hazard maps.

A possible explanation for any residual strain accumulation in the ETS region is that the combination of large and inter-ETS SSEs, which are smaller ETS events not readily resolvable with geodetic methods, are not accommodating the total slip deficit of the subducting Juan de Fuca plate. While the combination of ETS and inter-ETS

events is inferred to account for a nearly all of the remaining strain budget in this region (Ide et al., 2007; Aguiar et al., 2009), inter-ETS tremor is found downdip of regular ETS tremor (Wech et al., 2009; Wech and Creager, 2011), so may only accommodate the remaining slip deficit in the downdip portion of the ETS zone leaving a fraction of the slip deficit in the updip portion of the ETS zone.

The secondary locking along the subduction zone may be linked to the intersection of the Moho of the North American plate with the subducting plate interface. The physical and compositional changes near the Moho could result in an increase in locking by affecting several parameters, such as fluid migration from the dehydrating slab, a change in frictional stability, or a change in bulk strength of materials. In one possible explanation, which has also been proposed by Holtkamp and Brudzinski (2010), the increase in locking could be due to a rheological difference at the Moho, where the subducting slab encounters the stronger, potentially brittle, overriding mantle. Chen and Molnar (1983) showed that the composition of the upper mantle near the Moho allows for seismic deformation at higher temperatures (600°C–800°C) than the lithosphere (250°C–450°C). The area of secondary locking would then be constrained to the along-dip section of the plate boundary between the Moho and the high temperature onset of crystal plasticity in the mantle. The difference in temperatures at the Moho among subduction zones could help explain why different subduction zones exhibit different ETS behaviors.

Although there is some variability among studies, the Moho in Cascadia is typically thought to be at a depth of 30–40 km, with additional variability along strike (Bostock et al., 2002; Nedimović et al., 2003; Nicholson et al., 2005; Wang et al., 2008; Peacock et al., 2011; Gao et al., 2011). This range in depth is consistent with the depth of tremor (Brown et al., 2009), as well as the modeled depth of the

secondary locking found in the leveling data. The strength of the over-riding mantle would be at a maximum at the Moho and decrease with depth. This could explain why the modeled secondary locking, as well as geodetically derived slip distribution of SSEs, are located on the updip extent of the tremor distribution, while the inter-ETS tremor is located downdip of the peak secondary locking where the overriding mantle is weaker. Finer tomographic imaging of the Moho near the slab interface and more precise source locations of tremor may help to elucidate the spatial relationship of the mantle corner with ETS and the secondary locking.

While the model of Chen and Molnar (1983) provides a useful conceptual framework for understanding a region of locking in the ETS zone, we acknowledge that the fault interface is likely more complex than this simplified view. The fault zone is likely composed of heterogeneous materials that are sheared along the surface. The actual transition in fault properties and behaviors in this area is likely more diffuse. The overriding material along the fault in the ETS zone is thought to have low permeability which allows for elevated pore fluid pressures, decreasing the effective normal stress (Audet et al., 2009; Ghosh et al., 2010a; Peacock et al., 2011). The ability to hold even a small amount of long-term strain in the ETS zone appears counter to the low effective stress that has been inferred for the ETS zone. A successful conceptual model must account for the how the fault is able to be temporarily weakened, while also maintaining partial long-term locking on the updip edge of the ETS zone that persists over many ETS cycles.

2.5. Conclusion

We have explored the potential of long-term strain accumulation near the ETS zone on Cascadia. Based on our findings, the assumption that ETS delineates the

down-dip extent of possible megathrust rupture may not be definite. However, we only have clear evidence of secondary locking from the Newport leveling profile. If locking exists near the ETS zone, it must be a small fraction of the plate rate. This small amount of partial locking is consistent with, but difficult to resolve in the GPS data, and may have significant implications on the kinematic behavior of the Cascadian subduction zone.

Secondary locking in the ETS zone must be released within the megathrust earthquake cycle. This could be accomplished by megathrust earthquakes propagating into the ETS zone, effectively extending the rupture area farther down-dip than previous models predict and increasing the moment magnitude by up to 5%. Alternatively, the accumulated strain could be released through aseismic processes, such as in future large ETS events, long-term ETS events, or as afterslip.

2.6. Bridge

In this chapter, I used decadal-scale leveling measurements constrained by tide-gauge observations, and multi-year GPS observations to quantify a zone of partial secondary locking along the Cascadia subduction zone. Optimization of iterative forward models shows that this zone of secondary locking is located slightly up-dip of tremor for all four of the profiles. Including secondary locking provides a statistically significant improvement to fits of the leveling data in central Oregon. The inclusion of secondary locking requires a slightly deeper locked zone, which could potentially affect future hazard maps in the region. This zone of secondary locking must be released at some point within the megathrust cycle through a mechanism that remains unknown.

In the next chapter, I investigate the spatial relationship of tremor and slip during slow slip events in Cascadia through the use of static slip inversions of GPS time series

data, forward modeled slip distributions based on tremor locations, and strainmeter observations. To assess the utility of using tremor as a proxy for slip, I develop a method of using the temporal and spatial characteristics of tremor observations to model slip on the fault interface. I then use the tremor-derived slip model to compare tremor distribution and density to geodetic observations of slow slip to investigate the along dip and along strike variability of tremor and slip.

CHAPTER III

ASSESSING THE SPATIAL RELATIONSHIP OF TREMOR AND SLIP IN CASCADIA USING GPS INVERSIONS, TREMOR-DERIVED SLIP MODELS, AND STRAINMETERS

In preparation for submission to *Journal of Geophysical Research: Solid Earth*. Co-authored with David Schmidt. As lead author, I wrote the manuscript, performed all of the analysis and interpretation, and drafted all the figures for this chapter. My co-author, David Schmidt, helped me with editorial assistance and the interpretation of my results.

3.1. Introduction

Since the discovery of transient slow slip in subduction zones (Hirose et al., 1999; Dragert et al., 2001) and associated non-volcanic tremor in Japan and Cascadia (Obara, 2002; Rogers and Dragert, 2003), episodic tremor and slow slip (ETS) has been observed in many different tectonic settings worldwide (Peng and Gomberg, 2010). In subduction zones, slow slip is associated with the release of stress along a transitional regime between the shallower seismogenic locked zone and the deeper, aseismic slipping zone. The proximity of the slow slip zone to the seismogenic zone, and stress transfer from slow slip events to the seismogenic zone, makes the characterization of tremor and slow slip vital to understanding the behavior of the megathrust cycle (Rogers and Dragert, 2003; Kato et al., 2012; Kato and Nakagawa, 2014).

Tectonic tremor that is associated with ETS is characterized by a frequency spectrum that is dominant in the lower frequencies (1-10 Hz) (Obara, 2002).

Katsumata and Kamaya (2003) identified the existence of low-frequency earthquakes (LFEs) associated with tectonic tremor, and later studies have suggested that tremor is a superposition of LFEs (Shelly et al., 2007b). Source locations derived from the observable P- and S-wave arrivals in LFEs place them, and the associated tremor, at or near the plate interface (Shelly et al., 2006; La Rocca et al., 2009). The characteristics of tremor and LFEs suggest that they are associated with low shear stress and the presence of fluids (Shelly et al., 2007b).

The Cascadian subduction zone is characterized by the subduction of the oceanic Juan de Fuca plate beneath the continental North American plate at a convergence rate of ~ 4 cm/yr (Miller et al., 2001). In central and northern Cascadia, major slow slip events (SSEs) occur along the plate interface at depths of 25–40 km, have recurrence intervals of 10–22 months, and durations of weeks to months (Miller et al., 2002; Rogers and Dragert, 2003; Szeliga et al., 2008; Holtkamp and Brudzinski, 2010). Each major event typically results in ~ 3 –6 mm of surface displacement, which is inferred to be associated with ~ 2 –6 cm of slip on the fault interface (Schmidt and Gao, 2010).

The spatial and temporal correlation of tremor and slow slip in Japan and Cascadia has led to scaling relations that relate the duration of tremor to the geodetically inferred moment release (Ide et al., 2007; Aguiar et al., 2009). In Cascadia, tremor and slip have been shown to be correlated at tidal frequencies and sub-daily periods using borehole strainmeters (Hawthorne and Rubin, 2010, 2013). While the correlation of tremor and slip is observed at large scales, the detailed relationship of tremor and slip is not apparent. Dragert and Wang (2011) inverted GPS data from a slow slip event from 2008 in northern Washington and suggested that slip may extend further updip than the tremor. Although there appears to

be a prevalent spatial-temporal correlation between tremor and slip in Japan and Cascadia, a clear along-dip offset between tremor and slip has been observed along subduction zones in Alaska and Mexico, with slip occurring updip of a majority of the tremor (Peterson and Christensen, 2009; Kostoglodov et al., 2010; Brudzinski et al., 2010). Instances of tremor without detectable slip have been observed in southwest Japan (Obara et al., 2010), while slow slip has been observed without tremor in the Hikurangi subduction zone in New Zealand (Delahaye et al., 2009). Recently, Wech and Bartlow (2014) observed a small area of slip not associated with tremor during a large ETS event in Cascadia.

This disassociation of tremor and slip suggests that the two phenomena may be controlled by distinct physical mechanisms that may, or may not, be intrinsically linked. Fundamental questions still remain as to why certain subduction zones, like Japan and Cascadia, have a strong correlation of tremor and slip, while other subduction zones exhibit very different relationships. Additionally, considering tremor and slip occur along a transitional regime between the locked and freely slipping zone, it is unclear whether the same segment of a fault can behave both seismically and aseismically at different times.

In this study, we evaluate the spatial relationship of tremor and slip for all major slow slip events in central and northern Cascadia from 2009 to 2016 using static GPS inversions, tremor-derived slip distributions, and strainmeter observations (Fig. 1). Static and kinematic inversions of GPS data in Cascadia have been performed in several previous studies (McGuire and Segall, 2003; Szeliga et al., 2004; Melbourne et al., 2005; Szeliga et al., 2008; Wang et al., 2008; McCaffrey, 2009; Wech et al., 2009; Schmidt and Gao, 2010; Bartlow et al., 2011; Dragert and Wang, 2011; Wech and Bartlow, 2014). We expand on this work by providing an up-to-date catalog of

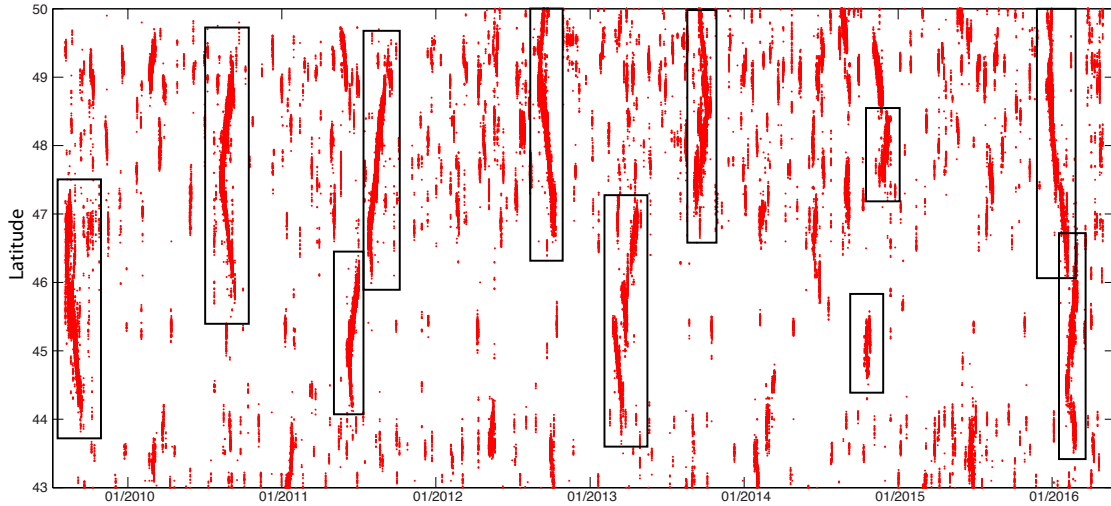


FIGURE 3.1. Tremor distribution in northern and central Cascadia from mid-2009 to early-2016 from Wech (2010). Black boxes highlight the major episodic tremor and slip events analyzed in this study.

slip distributions for recent slow slip events. The increase in geodetic instrumentation and the inclusion of the comprehensive tremor catalog of Wech (2010) since many of these early studies has increased our ability to resolve finer spatial details of slip and the associated tremor. We compare the slip distributions from inversions of observed surface displacements with the occurrence of tremor, as well as tremor-derived slip distributions that use tremor as a proxy for slip. We also include several strainmeter observations as an independent geodetic constraint on the relationship of tremor and slip. Our findings suggest that the one-to-one relationship between aseismic slip and tremor observed at large scales (over 100 km) likely breaks down when examined at smaller scales.

3.2. Methods

3.2.1. Static GPS Slip Inversions

Slip distributions during 11 major ETS events in Washington and Oregon from 2009 to 2016 are estimated using a weighted least-squares inversion of static offsets from GPS time series data. Daily GPS positions are provided by the Plate Boundary Observatory (PBO) and the Pacific Northwest Geodetic Array (PANGA). The three-component GPS data is detrended to remove the long-term interseismic signal due to the buildup of strain near the plate boundary. Time series with sparse data (missing data on more than $\sim 20\%$ of days) and/or significant scatter in the daily positions (day-to-day displacements greater than two times the daily uncertainties) are omitted from the inversions. GPS stations near volcanic centers, particularly Mount St. Helens, are excluded for multiple events due to the presence of non-tectonic artifacts (i.e. bias from snowfall). Significant common-mode signals were removed from the vertical data for the 2013 and 2015 ETS events near Puget Sound following the methods of Wdowinski et al. (1997). For these events, multiple vertical time series from stations located away from the expected surface displacements are stacked and averaged. The average vertical signal is then removed from all of the GPS stations. This process may introduce artifacts into the data, so it is only used for events that have significant common-mode signals. Static offsets are calculated by differencing the weighted averages of GPS positions 10 days before and after the events for all three components of displacement. The weights are determined by the daily uncertainties. The final offset uncertainties are calculated by combining the uncertainties of the weighted averages before and after the event following the methods of Taylor (1997). The offset uncertainties are then used to weight the data

in the inversion. The number of GPS stations used for each event ranges from 54 to 165 depending on the availability of data and the size of the event.

We use a three-dimensional discretized fault model constrained by the slab geometry of McCrory et al. (2012). The fault model is composed of triangular fault patches with side lengths of approximately 10 km. Greens functions relating slip on the triangular fault patches to surface displacements in an elastic medium are calculated using the boundary element code Poly3D (Thomas, 1993). Slip is assumed to be along the direction of convergence. The convergence rate and direction is calculated using the Juan de Fuca-North America pole of rotation of Mazzotti et al. (2007) for the Washington and Canadian sections on the fault and the Juan de Fuca-Oregon forearc Euler pole of Wells and Simpson (2001) for the Oregon section.

Considering the inverse problem is underdetermined, we apply additional positivity and smoothness constraints. Positivity is enforced using the nonnegative least squares method of Lawson and Hanson (1995). Smoothness is imposed by adding a finite-difference approximation of the Laplacian operator to the design matrix with a corresponding number of zeros added to the data vector. The preferred amount of smoothing is determined by looking at the tradeoff between the overall misfit and roughness of the slip on the fault patches.

3.2.2. Tremor-derived Slip Distributions

To assess the spatial and temporal relationship of tremor and slip, we create time-dependent slip models based on the distribution and propagation of tremor. Previous studies have suggested that tremor may be a useful proxy for slip on the fault interface in Japan and Cascadia (Hiramatsu et al., 2008; Wech and Creager, 2008; Aguiar et al., 2009; Wech et al., 2009; Wech and Creager, 2011). We use tremor data provided by

the Pacific Northwest Seismic Network (PNSN) from mid-2009 to mid-2016 (Wech, 2010). The tremor times and locations are calculated by using a cross-correlation technique that identifies coherent 5-minute envelopes of tremor signal within a sub-network of seismic stations (Wech and Creager, 2008). The tremor catalog contains possible duplicate tremor locations due to the overlap of seismic station sub-networks. We account for the duplicates by finding contemporaneous tremor that occur within 25 km of each other and average their locations. This procedure is consistent with the reported location uncertainty in tremor of (Wech, 2010). We then spatially and temporal bin the tremor associated with major ETS events in Cascadia (Fig. 1). The tremor data does not contain individual magnitude estimates.

The tremor distribution for each major event is used as a proxy for slip by assuming each tremor occurrence represents some amount of slip over some amount of area. This is not meant to provide actual estimates of the moment associated with individual tremor bursts; rather, it is simply meant to construct a slip distribution from the distribution and density of tremor. Although the tremor catalog does not contain depth estimates, we also assume that the tremor is located on the plate boundary interface. This is consistent with studies of tremor and low-frequency earthquakes in Cascadia (La Rocca et al., 2009; Bostock et al., 2012) and Japan (Shelly et al., 2006).

Slip on the fault interface is modeled by ascribing a specified amount of slip on model fault patches that are located within a specified distance of each tremor location. An additional third parameter is added that shifts the tremor-derived slip distribution along the convergence direction to assess whether shifting the slip in relation to the tremor can improve the data fits. The same fault model is used for the static inversions and the tremor-derived slip models. The ascribed slip is binned into

daily slip estimates based on the temporal record of tremor. The daily slip values are then used to forward predict the surface displacements at GPS station locations using the same Greens functions described in the previous section. The model parameters are constrained using an iterative forward parameter search. WRMS values are used to identify the optimal parameters and are calculated by differencing the GPS offsets described in the previous section and the predicted offsets from the tremor-derived slip distribution. We choose to exclude the vertical GPS data in the optimization due to their relatively high uncertainties compared to the horizontal components and the tendency for the vertical data to contain multi-day artifacts. The same GPS time series data and offsets are used for both the static inversions and the tremor-derived slip optimization.

The trade-off between the slip per tremor window and the area per tremor window effectively acts as a smoothing criterion based on the density of tremor. Slip models with a relatively high amount of slip over a small area can result in approximately the same WRMS values as models with a relatively low amount of slip over large areas, which limits our ability to resolve the roughness of slip (Fig. 2). We limit the upper bounds of the slip per tremor window to values that result in overall slip magnitudes that are less than approximately two times the convergence rate, considering it is physically unlikely that an area with a recurrence interval of approximately 16 months can have slip that is significantly more than the accumulated slip budget.

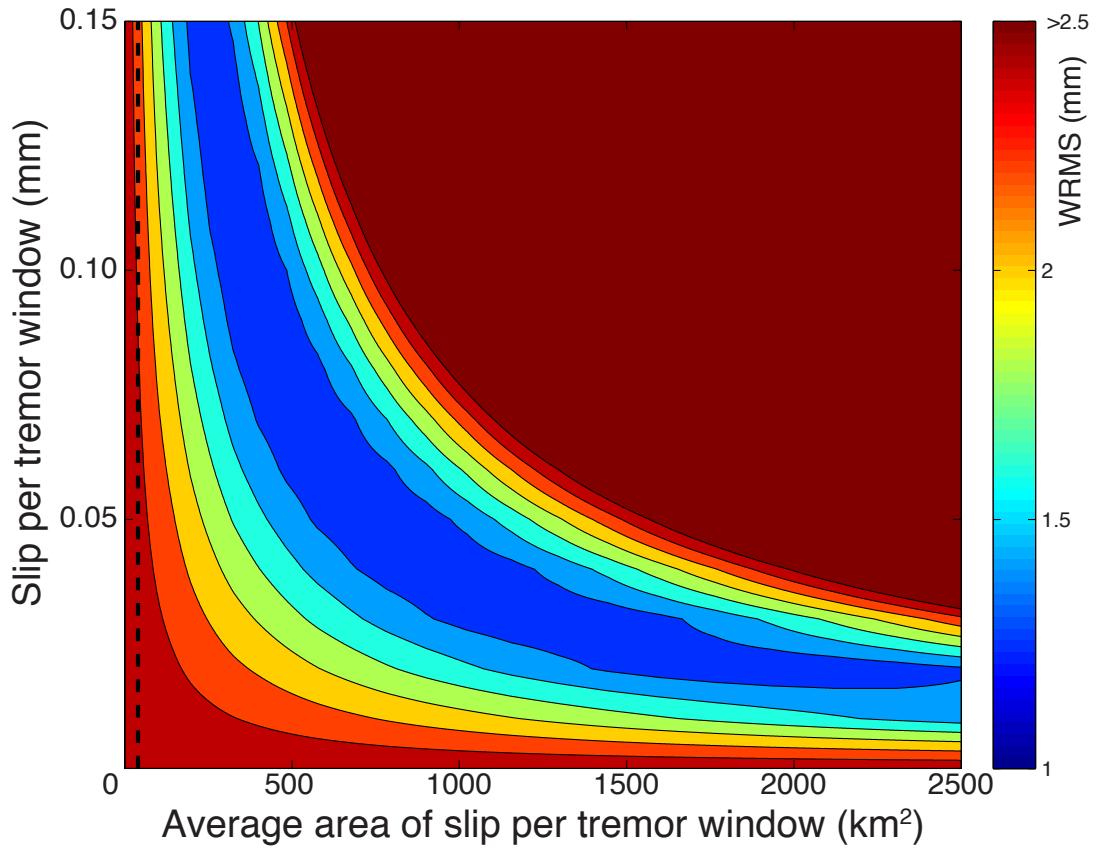


FIGURE 3.2. Trade-off of the amplitude and the area of slip ascribed to each tremor window. Dashed black line represents the average area of the model fault patches.

3.3. Results

We focus on the 11 major ETS events in Oregon and Washington from 2009 to 2016; the time span of the tremor catalog provided by the PNSN (Wech, 2010) (Fig. 2 and 3). The magnitude of these events range from a $\sim M_w$ 6.8 for the 2010 and 2012 Washington events, to $\sim M_w$ 6.1 for the 2014 Oregon event. Small bursts of tremor, known as inter-ETS tremor, occur between large ETS events. Inter-ETS tremor is typically smaller in duration and extent, and occurs downdip of tremor associated with larger ETS events (Wech and Creager, 2011). The selection criterion

for determining a major ETS event is somewhat arbitrary, but we try to include all events that are large enough to be reasonably resolved with GPS data (i.e. is observable in multiple GPS time series). Some events that we consider, such as the 2013 Oregon event and the 2013 Washington event, may actually be a combination of smaller events. The temporal and spatial proximity of these events makes it difficult to separate smaller sub-events as represented in the surface displacement time series. For these reasons, we choose to treat them as a single event rather than several smaller events.

In general, there is a decrease in the resolution of the inversions and the tremor-derived slip models north of the southern-most portion of Vancouver Island due to relatively sparse GPS coverage (Fig. B1-B11). Although a significant amount of tremor activity occurs in this area, the lack of resolution of slip on the fault makes drawing definite conclusions difficult. For this reason, we primarily focus on regions south of Vancouver Island in Washington and Oregon. A full analysis of the model and data resolution is provided in the following section.

We characterize each ETS event by analyzing a combination of the tremor distributions, static inversions of GPS offsets, and tremor-derived slip models. A summary of all of the events can be found in Table 1. The proceeding sections detail each individual event and highlight the similarities and differences between the tremor, static GPS inversion, and tremor-derived slip. In general, the GPS inversions and the tremor-derived slip results are consistent on a large scale, although there are discrepancies for multiple events (Fig. 3 and 4). Details of each event, including the GPS inversion slip distributions, tremor-derived slip distributions, tremor, model sensitivity, and fits to the GPS data can be found in the supplementary figures B1–B12.

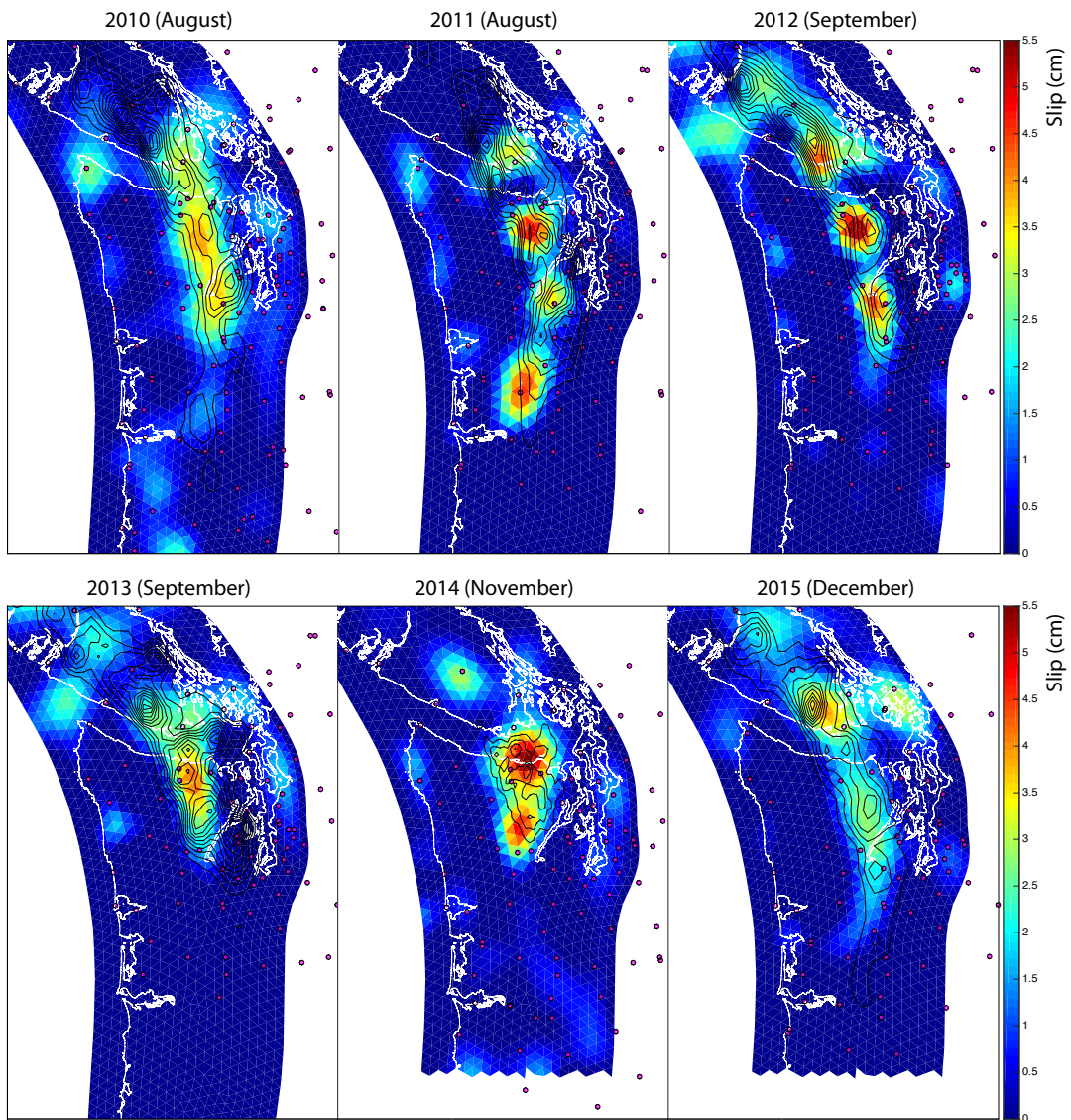


FIGURE 3.3. Slip on the fault in northern Cascadia derived from static inversions of GPS offsets. Black lines contour the tremor density associated with each event. The GPS sites used in this analysis (magenta dots) and the coastline (white line) are also shown.

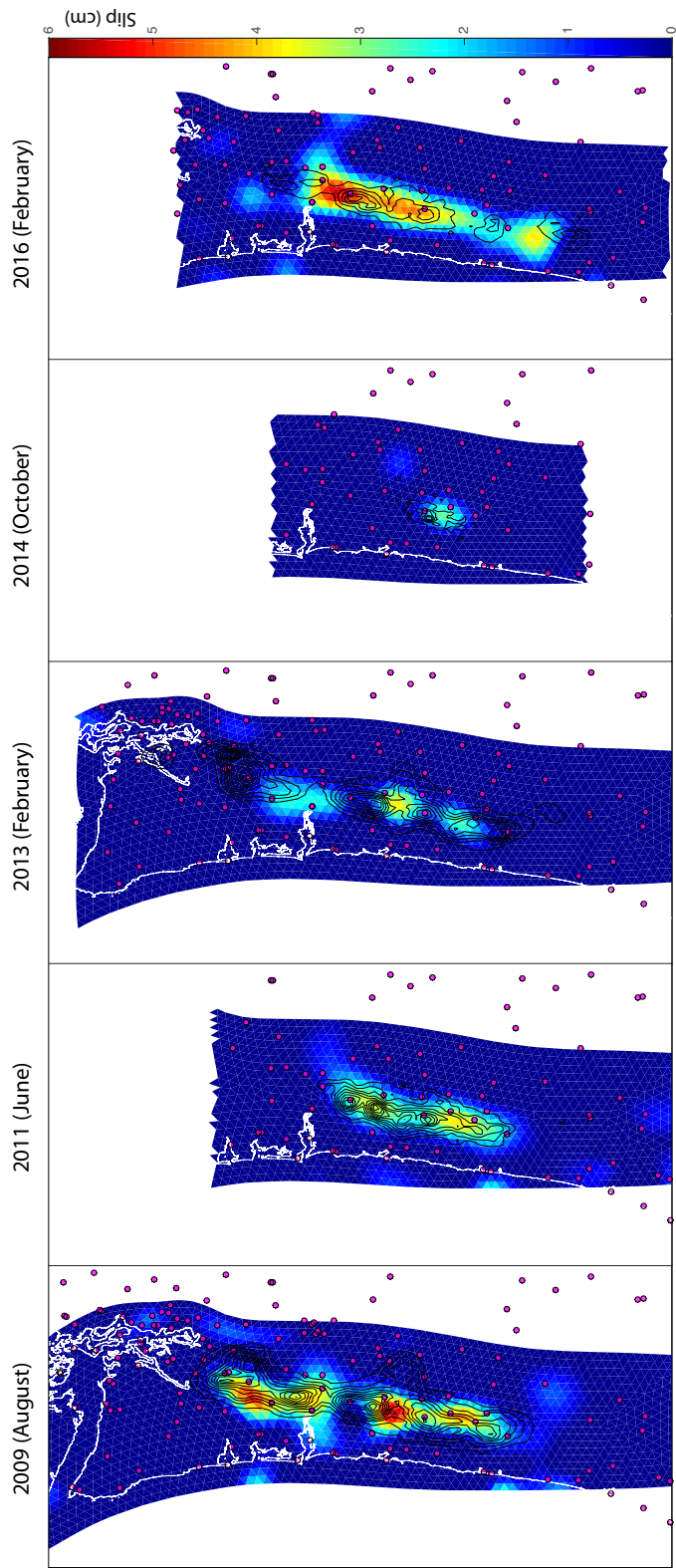


FIGURE 3.4. Slip on the fault in central Cascadia derived from static inversions of GPS offsets. Black lines contour the tremor density associated with each event. The GPS sites used in this analysis (magenta dots) and the coastline (white line) are also shown.

| | Moment (Nm x 10 ¹⁹) Inversion | Moment (Nm x 10 ¹⁹) Tremor- derived | M _w Inversion | M _w Tremor- derived | Stress Drop (Mpa) Inversion | Stress Drop (Mpa) Tremor- derived | WRMS Inversion | WRMS Tremor- derived | # of GPS stations |
|----------------|---|--|-----------------------------|--------------------------------------|-----------------------------------|--|-------------------|----------------------------|----------------------|
| 2009 OR (Aug) | 1.98 | 2.34 | 6.80 | 6.85 | 0.289 | 0.305 | 0.934 | 1.397 | 165 |
| 2010 WA (Aug) | 2.52 | 2.25 | 6.87 | 6.84 | 0.212 | 0.272 | 0.939 | 1.532 | 154 |
| 2011 OR (June) | 1.07 | 0.91 | 6.62 | 6.57 | 0.256 | 0.314 | 0.650 | 1.260 | 89 |
| 2011 WA (Aug) | 1.63 | 1.43 | 6.75 | 6.71 | 0.237 | 0.281 | 0.997 | 1.392 | 124 |
| 2012 WA (Sept) | 2.45 | 1.87 | 6.86 | 6.78 | 0.246 | 0.308 | 1.070 | 1.245 | 120 |
| 2013 OR (Feb) | 0.66 | 0.72 | 6.48 | 6.50 | 0.228 | 0.192 | 0.904 | 1.377 | 124 |
| 2013 WA (Sept) | 2.10 | 1.15 | 6.82 | 6.64 | 0.237 | 0.202 | 0.854 | 1.285 | 96 |
| 2014 OR (Oct) | 0.15 | 0.20 | 6.06 | 6.14 | 0.210 | 0.215 | 1.055 | 1.145 | 54 |
| 2014 WA (Nov) | 1.68 | 0.98 | 6.76 | 6.60 | 0.229 | 0.312 | 0.702 | 1.113 | 106 |
| 2015 WA (Dec) | 1.89 | 1.59 | 6.79 | 6.74 | 0.218 | 0.246 | 1.321 | 1.958 | 90 |
| 2016 OR (Feb) | 1.74 | 1.76 | 6.76 | 6.77 | 0.333 | 0.265 | 1.120 | 1.947 | 100 |

TABLE 3.1. Event Parameters

3.3.1. August 2009 (Oregon)

The tremor during the August 2009 ETS event in Oregon initiates near 46.4°N and propagates to the north and south (Supplementary Figure B1). A significant portion of the northern propagating tremor occurs at depths below 40 km, while a majority of the southern propagating tremor occurs at depths around 35 km. There are several bursts of deep (~45 km) tremor near 45.5°N during the event that do not follow the main propagation front.

The overall along-strike extent of slip matches well with the extent of tremor, although there appears to be variations between the tremor and slip at multiple locations. The northern segment of slip is concentrated on the updip edge of tremor, indicating that the large amount of deep tremor is not associated with much slip on the fault. The central segment has a region containing an area with a relatively high (~4.5 cm) amount of slip, but relatively low tremor density. This slip patch is also located at the same latitude as the deep tremor bursts. The distribution of slip in the southern segment matches well with the tremor distribution. Our results also match

well with the time-dependent GPS inversion of Bartlow et al. (2011), although the results here have a higher amount of slip located west of Portland.

The optimal slip per tremor and area per tremor parameters for the tremor-derived slip result in a relatively smooth slip distribution. The surface displacements can be best fit if the tremor-derived slip model is shifted along the convergence direction 4 km (toward the trench), indicating that the overall distribution of tremor might be located slightly downdip of the overall slip. Considering the southern and central segments of slip appear to be correlated along dip, this preferred shift is likely the result of the apparent offset of tremor and slip in the northern segment.

3.3.2. August 2010 (Washington)

Tremor during the August 2010 ETS event in Washington initiates near 47.5°N and propagates at a similar rate to the north and south (Supplementary Figure B2). The density of tremor is the highest under the southern part of Vancouver Island. Although there are multiple GPS stations located on the southern part of Vancouver Island, the static inversion does not locate much slip in this area. The overall slip associated with this event appears to be relatively smoothly distributed in relation the 2011 and 2012 events in Washington. The optimal tremor-derived slip distribution is also relatively smooth. The surface displacements can be better fit if the tremor-derived slip distribution is shifted along the convergence direction 7 km.

3.3.3. June 2011 (Oregon)

Tremor from the June 2011 Oregon event initiates near 45°N and propagates to the south and north (Supplementary Fig. B3). The southern extent of tremor terminates at $\sim 44.3^{\circ}\text{N}$, while the northern extent extends to $\sim 46.2^{\circ}\text{N}$. The

distribution of the slip, both along dip and along strike, matches well with the distribution of tremor. The optimal parameter values for slip and area per tremor associated with the tremor-derived slip model are relatively intermediate values compared to the rest of the events. The optimal shift in the tremor-derived slip is -1 km, indicating that shifting the tremor-derived slip distribution does not improve the fit to the data.

Using a time-dependent inversion of GPS data and observations from two strainmeters, Wech and Bartlow (2014) suggest that while the tremor associated with the 2011 Oregon event stops near the Washington-Oregon border, a small amount of slip continues to propagate along strike into Washington, at which point tremor occurs once again and the tremor and slip then continue to propagate further north to the southern portion of Vancouver Island. Wech and Bartlow (2014) suggest the low magnitude slip during the tremor quiescence is likely below the detection threshold of GPS, which may explain why we do not resolve it with our static inversions. For this reason, we choose to treat the 2011 Oregon and Washington events as separate in our analysis while recognizing that they may be continuously linked.

3.3.4. August 2011 (Washington)

The tremor associated with the August 2011 Washington event initiates near 46.5°N and propagates north to the southern portion of Vancouver Island (Supplementary Figure B4). There is a small burst of tremor that propagates south to $\sim 46.1^{\circ}\text{N}$ approximately 10 days after the initiation of tremor. This southern burst of tremor is associated with the thin tail in the southern most tremor contours of figure 3. While there is a relatively small amount of tremor in this region, the static

inversion places ~ 3.5 cm of maximum slip centered on the updip edge of the tremor. Further to the north, the slip is relatively patchy with larger amounts of slip located near areas of high tremor density. The slip patch under Vancouver Island is slightly downdip of the peak tremor density, but the lower resolution in that region may influence the accuracy of the distribution.

The optimal parameters for the tremor-derived slip results in a relatively coarse slip distribution. Shifting the tremor-derived slip along the convergence direction by 8 km results in the minimum misfit, indicating that a majority of slip might be updip of the peak tremor distribution. While these optimal parameters are calculated using the overall misfit to the data, there appears to be a significant variation along-strike in the relationship of tremor and slip during this event. Simply comparing the static inversion result and the distribution of tremor, it appears that the southern portion of slip (near the Oregon border) is significantly updip of the tremor, the slip patches under the Olympic Peninsula are relatively collocated with the peak tremor density, and the northern slip patch might be slightly downdip of the peak tremor density.

3.3.5. September 2012 (Washington)

Tremor for the 2012 Washington event starts near 49°N and propagates north under Vancouver Island and south below Puget Sound (Supplementary Figure B5). The southerly propagation is fairly consistent in both velocity and depth until it reaches 47°N , at which point the propagation velocity slows and the remaining tremor occurs at deeper (≥ 40 km) depths. The slip patches determined by the GPS inversion are strikingly similar to the northern slip patches of the 2011 Washington event. The slip patches match well with the along-strike variation in tremor density, although the two patches under the Olympic Peninsula appear to be slightly updip of the peak

tremor density. The optimal tremor-derived slip model has a correspondingly coarse distribution of slip. The best-fit model also has an along-convergence shift of 7 km, indicating a slight downdip offset of tremor from slip.

3.3.6. February 2013 (Oregon)

The tremor for the 2013 Oregon event is composed of three relatively distinct events that are closely related in space and time (Supplementary figure B6). The initial event starts on the deeper (~ 40 km) portion of the fault at $\sim 45.5^\circ\text{N}$ and propagates to the south for ~ 16 - 17 days. As the first event stops, another event initiates at $\sim 46^\circ\text{N}$ and propagates south to $\sim 45.1^\circ\text{N}$, spatially overlapping with the first event. After the second event stops, a brief burst of tremor occurs north of the initiation location of the second event. This is then followed a few days later by a northward propagating front that is composed of many events below 40 km.

The slip associated with the static GPS inversions has multiple characteristics that are distinct from the tremor. The maximum amount of slip is located near the initiation of the first event ($\sim 45.5^\circ\text{N}$). This slip patch also corresponds to an area with a relatively less dense amount of tremor that extends deeper on the fault interface. Both the slip and the tremor distribution in this area are very similar to the 2009 Oregon event. Another slip patch is located further to the north in an area of very low tremor density. Interestingly, this is the same area that Wech and Bartlow (2014) identified as having tremor-less slip during the 2011 event. Additionally, the northernmost extent of tremor does not seem to be associated with much slip. This can be seen at the GPS station P430, which is just west of the tremor, where little to no surface displacement is evident.

The tremor-derived slip model provides a relatively poor fit to the data and a wide range of model parameters can equally fit the data. The tremor-derived slip model best fits the data with an along-convergence shift of 1 km, indicating that the model is not improved by an along dip shift. Considering the relatively significant difference in the tremor and slip distributions and the variability along strike, it is unlikely that a small shift in the location of the tremor-derived slip model will result in a significant improvement in the fits to the data.

3.3.7. September 2013 (Washington)

The tremor during the 2013 Washington event is the most complex of all of the events (Supplementary Figure B7). What we treat as one single event is likely two events that initiate at different locations and merge. The southern portion of the event starts near 47.5°N at $\sim 40\text{-}45$ km depth and propagates ~ 0.5 degree south over about 7 days. A deep tremor burst then occurs further north at $\sim 48.4^{\circ}\text{N}$ while there is a quiescence of tremor near $\sim 47.5^{\circ}\text{N}$ for several days. The tremor then starts again at 47.5°N and propagates north to $\sim 48.5^{\circ}\text{N}$ near the southern portion of Vancouver Island, where it meets the northern portion of the event. The northern portion of the event initiates near 50°N and propagates south until it merges with the southern portion. This event is unique in that the deeper bursts of tremor seem to migrate along strike earlier than the shallow tremor. Being there are spatial and temporal gaps among the deeper bursts of tremor, this interpretation would require that the deeper bursts are related through aseismic slip processes or are triggered by stress changes.

The slip derived from the static inversion matches fairly well with the updip extent of tremor as well as an area that extends further downdip on the southern edge

of Vancouver Island. However, the inversion does not result in slip that corresponds with a deep patch of tremor near the southern portion of Puget Sound. This is an area of relatively dense GPS coverage (good resolution) so it is unlikely this deep tremor is associated with a significant amount of slip. The tremor-derived slip model is best fit with an along convergence shift of 10 km, the highest of all the events. This could be due to the relatively large amount of deeper tremor that does not seem to be associated with much slip.

3.3.8. October 2014 (Oregon)

The October 2014 event is the smallest event we consider (Supplementary Figure B8). A small amount of tremor activity initiates near 45°N at a depth of ~ 40 km. A few days later the activity increases and propagates north and south, as well as updip, for several days. This is followed by multiple small bursts in the same general location. The entire event only lasts ~ 2 weeks.

The slip determined by the static inversion generally matches well with the distribution of tremor. The tremor-derived slip is best fit with an along-convergence shift of -4 km, indicating that there may be some amount of slip that occurs slightly downdip of the tremor. This result corresponds well with the location of slip from the GPS inversion. Although several GPS stations are located near this event, the details are less resolved due to the small size and duration of this event.

3.3.9. November 2014 (Washington)

The tremor associated with the November 2014 ETS event initiates under the southern portion of the Olympic Peninsula ($\sim 47.6^{\circ}\text{N}$) at depths between 40 and 45 km (Supplementary Figure B9). After a few days of quiescence, the tremor

activity begins again at shallower depths and propagates north to the southern edge of Vancouver Island. There is another tremor episode that occurs further to the north under Vancouver Island and ends at approximately the same time the event under Puget Sound begins. Due to the limited resolution on Vancouver Island and the temporal discontinuity of these two events, we chose to only consider the southern event (Fig. 1).

The slip associated with the GPS inversion matches well with the tremor distribution, although the southern-most extent of slip appears to be located slightly updip of much of the tremor. The tremor-derived slip model is best fit by shifting the slip along the convergence direction 6 km (updip).

3.3.10. December 2015 (Washington)

Tremor associated with the December 2015 ETS event in Washington begins under the southern portion of Vancouver Island at depths of 40–45 km (Supplementary Figure B10). After several days the tremor migrates updip and northwest under Vancouver Island as well as south. The southern portion of tremor migrates at a steady rate until it reaches $\sim 47.5^\circ\text{N}$, at which point there are several days of quiescence before tremor begins to again migrate south to approximately the Washington-Oregon border ($\sim 46.1^\circ\text{N}$). This last portion of tremor tends to be more sparse and mostly occurs at deeper depths (40–45 km) than the earlier propagation.

Slip derived from inverting GPS displacements matches the tremor well for this event. An area of high slip near the southern edge of Vancouver Island corresponds with an area of high tremor density. The slip patch downdip of this area is likely an artifact of the inversion. A small amount of slip is associated with the southern extent

of tremor as well. The tremor-derived slip is best fit with a small along-convergence shift of 3 km, indicating good match between the tremor and slip.

3.3.11. February 2016 (Oregon)

The most recent event we consider is the February 2016 ETS event in Oregon (Supplementary Figure B11). This event starts before the termination of the late-2015 event in Washington. Tremor initiates further south than the other Oregon events at $\sim 44.5^\circ\text{N}$ and migrates north and south. The northward migration continues to $\sim 46.5^\circ\text{N}$ and spatially overlaps with the southern extent of the 2015 Washington event. The southern migration is characterized by sparse amounts of tremor before terminating near $\sim 43.5^\circ\text{N}$ in an area with a relatively high density of tremor.

The along-dip distribution of slip derived from inverting the GPS data matches well with the tremor distribution. An area of high slip near Portland, OR extends north into an area of relatively low tremor density. A small amount of slip to the south extends through areas of low tremor density. The southern-most patch of slip is located further north than a majority of the tremor, but the lack of GPS observations in this area makes constraining the exact location of slip difficult. The tremor-derived slip best fits the data with a relatively smooth distribution of slip and an along-convergence shift of -2 km, indicating a good match between the tremor and slip.

3.4. Model Validation

We use a range of resolution tests to explore the resolvability of both the along-strike and the along-dip variability of fault slip on the subduction interface. We first use a standard checkerboard test in which we impose a time dependent distribution

of slip in a checkerboard pattern, where the slip patches have a duration and slip magnitude similar to a typical slow slip event. Surface displacements are then forward modeled at the locations of GPS stations used for the 2011 Oregon event and the 2012 event in northern Cascadia. Random-walk ($1 \text{ mm}/\sqrt{\text{yr}}$ for horizontal and $3 \text{ mm}/\sqrt{\text{yr}}$ for vertical) and white noise (0.7 mm for horizontal and 2.5 mm for vertical) are added to the predicted displacements. These values are consistent with Langbein (2008) and the errors reported for the PBO and PANGA processed data. The displacement offsets are then calculated using the same method that is used for the observed data (see section 2). The modeled noise levels tend to underestimate the observed variability in the vertical data due to the effects of non-tectonic processes such as atmospheric disturbances. To compensate for this, the actual uncertainties from the 2011 and 2012 offsets are used after calculating the horizontal and vertical synthetic offsets. This decreases the weight of the vertical offsets in the synthetic static inversions to the same relative level as in the inversions using actual data. The synthetic data is then inverted following the method described in section 2. As is expected, our inversions for the checkerboard input models are better resolved in areas with dense GPS coverage, and less resolved in areas of low coverage such as Vancouver Island (Fig. B12-B13). The relatively denser distribution of GPS stations on the eastern edge of the model space helps to compensate for the decreased resolution due to increased fault depth.

Considering we are primarily concerned with the ability of our inversions to resolve an along-dip offset between the peak tremor density and the peak slip, we create a generic synthetic slip distribution that initiates in the north and propagates south with a rupture velocity and magnitude similar to a typical slow slip event in both the northern (Washington) and central (Oregon) sections of the fault. The along-

dip slip is created assuming a Gaussian slip distribution centered at 37 km, which is meant to imitate the approximate along-dip distribution of tremor during an ETS event (Fig. 5 and 6). We forward predict synthetic time series, add random noise, and invert static surface displacements using the same method as the checkerboard tests. The inversion results tend to do a good job resolving this simple input slip model in the Puget Sound area, while the Oregon section tends to underpredict fault slip in areas with limited GPS coverage. The Oregon section also tends to slightly overestimate the width of the along dip distribution of slip (Fig. 6).

To assess our ability to resolve an along-dip difference in peak fault slip, we repeat the procedure using the same slip distribution, but shift it up to a depth of 34 km. Although the updip edge of slip is less resolved in the Puget Sound area for the shifted input model, a clear distinction between the 34 and 37 km input models can be resolved (Fig. 5c and 6c). In Oregon, a distinction between the two input models is evident, but to a lesser degree than the Puget Sound region, particularly with the estimates of maximum slip. The angle of the subducting slab is steeper under Oregon than under the Olympic Peninsula, which results in a shorter horizontal distance on the surface between two depth contours on the fault (Supplementary Figure B14). The decrease in resolvability of any offset between tremor and slip in Oregon is likely due to a combination of both the decreased resolution of the GPS data and the higher slab dip angle along Oregon.

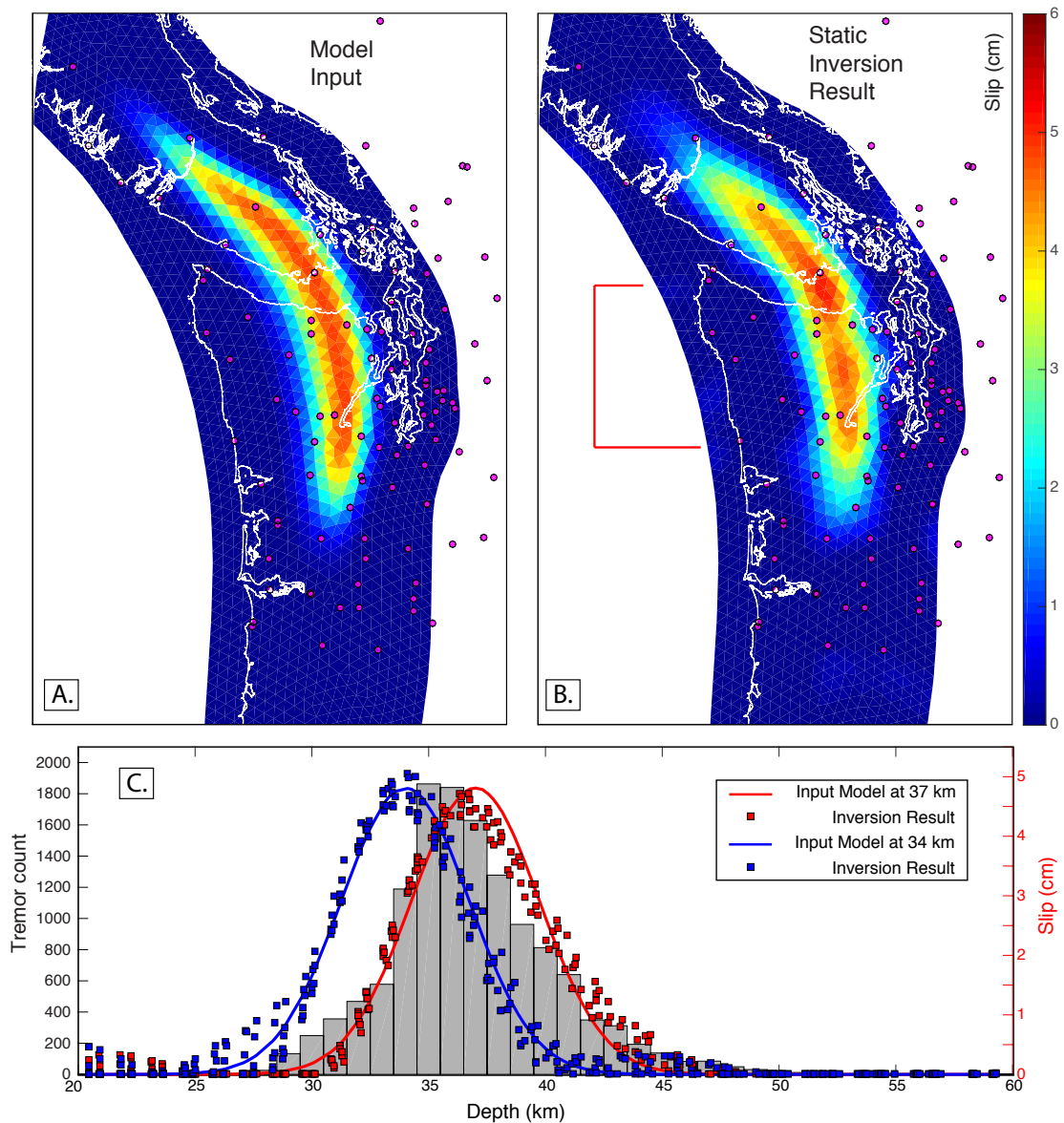


FIGURE 3.5. Resolution test of inversion results for northern Cascadia. A) Input slip model with maximum slip along the 37 km depth contour. Magenta dots represent GPS locations. B) Slip on the fault derived by inverting synthetic static offsets of displacement. Red bracket bounds the slip on fault patches and the tremor locations shown in part c. C) Profiles of slip with depth along the Olympic Peninsula. Grey histogram represents the tremor distribution for the 2011 event. The red line represents the input model. Red squares represent the inversion results. The blue line and squares represent the input model and results at 34 km depth.

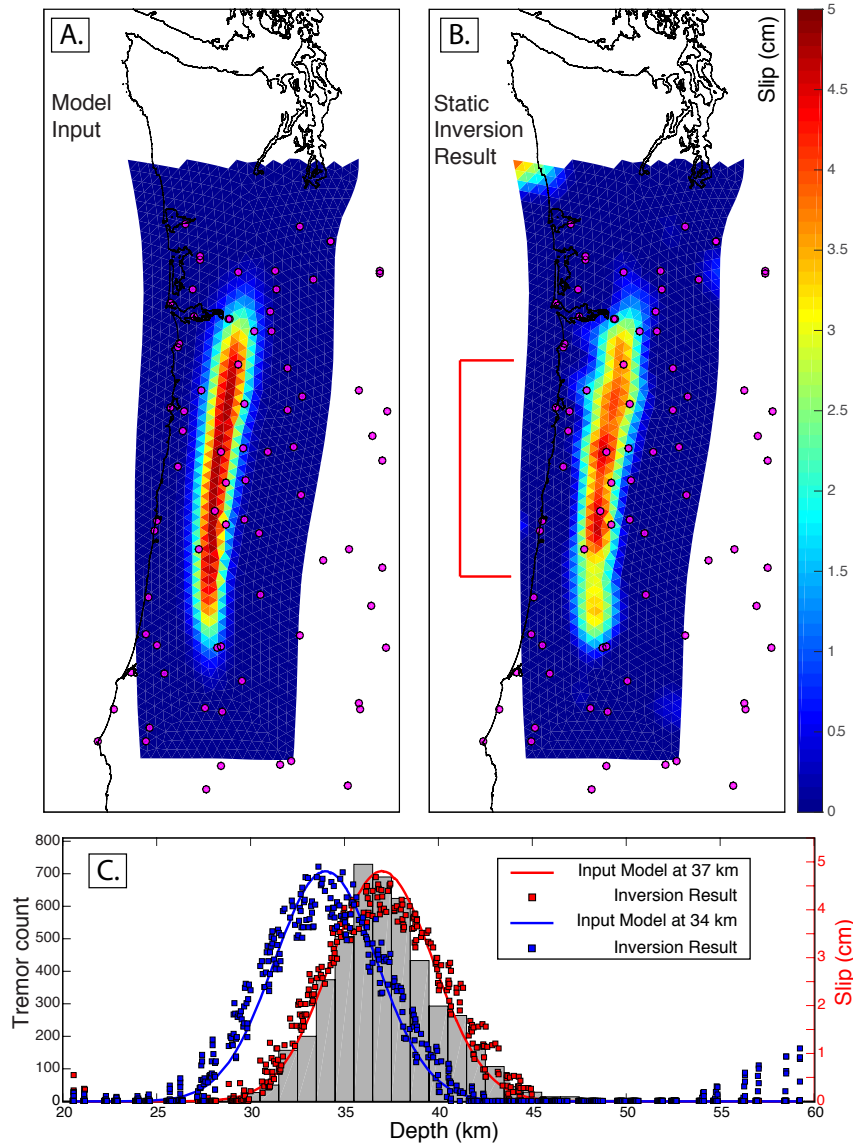


FIGURE 3.6. Resolution test of inversion results for central Cascadia. A) Input slip model with maximum slip along the 37 km depth contour. Magenta dots represent GPS locations. B) Slip on the fault derived by inverting synthetic static offsets of displacement. The red bracket bounds the slip on fault patches and the tremor locations shown in part c. C) Profiles of slip with depth along central and northern Oregon. Grey histogram represents the tremor distribution for the 2011 event. The red line represents the input model. Red squares represent the inversion results. The blue line and squares represent the input model and results at 34 km depth.

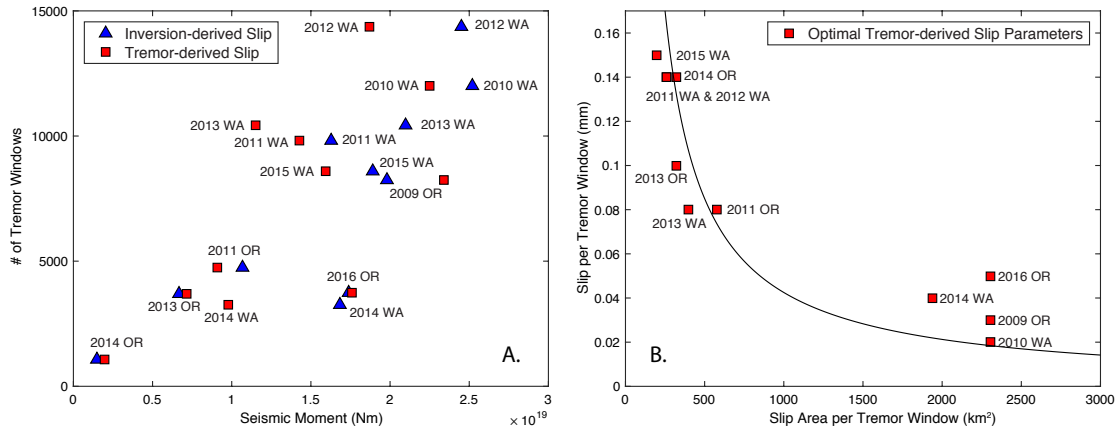


FIGURE 3.7. A) Relationship of total tremor occurrences (within 5-minute time windows) and seismic moment for all events. Blue triangles represent the results from static GPS inversions and red squares represent results of tremor-derived slip distributions. B) Optimal input parameters for the tremor-derived slip for all events. Red squares represent each event. Black line represents a constant seismic moment.

3.5. Discussion

3.5.1. Slip and Tremor Characteristics

Considering the tremor-derived slip models are scaled to fit the GPS displacements, it is expected that the overall moment release associated with the tremor derived-slip models is similar to the moment associated with the results from GPS inversions (Fig. 7A). The relatively large discrepancy for the 2014 Washington event is likely due to the patch of slip located on Vancouver Island that is to the north of the main slip patch (Supplementary Figure B9), while the discrepancy for the 2013 Oregon event could be do to a systematic difference between areas of high amount of slip and areas of increased tremor density.

For the relatively small range of moments of these events ($\sim M_w$ 6-7), the moment to total tremor duration relationship appears to be linear (Fig. 7A). This relationship generally agrees with the scaling relationships proposed by Ide et al. (2007) and Aguiar

et al. (2009). As was mentioned earlier, there is a tradeoff between the two primary input parameters used in the tremor-derived slip distributions, namely the slip per 5-minute tremor window and the area of slip per 5-minute tremor window (Fig. 2). The relationship of these two parameters effectively acts as a smoothing condition on the overall slip, with large areas and low amounts of slip per tremor window producing a smoother slip distribution than small areas with high amounts of slip per tremor window. The optimal parameters for a majority of the events (7 of 11) result in relatively coarse slip distributions, while the remaining 4 events are best fit with smooth slip distributions (Fig. 7B). Although there is typically only a small difference in the WRMS values for smooth versus coarse slip distributions, the range of optimal parameters might be indicative of a range in actual slip distribution on an event-by-event basis.

To investigate the possible spatial offset of tremor and slip, we add an additional third parameter to the tremor-derived slip models that shifts the distribution of slip a specified distance along the convergence direction. Considering the tremor distribution for major ETS events in Cascadia forms an approximately Gaussian shape with depth, this additional parameter provides a simple way to assess any systematic offset between the peak in slip and the peak in tremor distribution. Shifting the slip distributions along the convergence direction has a very minor effect on the optimal area and slip per tremor window parameters (Fig. 8).

In general, systematically shifting the tremor-derived slip southwest along the convergence direction (updip) results in a small decrease in WRMS values for a majority of the events in Washington (Fig. 8). Surface displacements for the Oregon events are best fit with little to no shift in the tremor-derived slip distributions; 4 of the 5 events are best fit with a small (1-3 km) northeast (downdip) shift. This small

amount of shift is likely not resolvable for individual events. As can be seen in Figure 8, the relatively small size and the decreased resolution for the 2014 Oregon event makes constraining the input parameters difficult.

Comparison of the GPS inversion-derived slip and the tremor-derived slip for individual events suggests that a simplistic systematic offset between tremor and slip does not adequately describe the possible spatial differences of tremor and slip, particularly for large events (Figures B1-B11). The 2009 and 2013 Oregon events in particular seem to exhibit different spatial relationships between tremor and slip depending on the location along-strike. Both events extend north to the southern edge of Puget Sound where there is a large amount of tremor on the deeper (~ 40 km) portion of the fault. The GPS inversions do not image much slip in this region while the tremor-derived slip has 4-5 cm of slip. Considering the depth of the fault significantly affects the resolution of the inversions, it is possible that the inversions simply can't resolve slip that is actually there.

These two events also reveal a difference in tremor and slip near the Oregon-Washington border. The tremor density in this region is significantly lower than the surrounding areas, while the GPS inversions result in a larger amount of slip. The slip in the region is also updip of a majority of the tremor for the 2013 event (Fig. 4 and Supplementary Figures B1 and B6). This can also be seen on the southern extent of the 2011 Washington event (Fig. 3 and Supplementary Figure B4). This corresponds well with the area Wech and Bartlow (2014) identified as having aseismic slip during the full along-strike extent of the 2011 event. Lastly, in a region southwest of Portland, both of these events have a large patch of slip on the updip edge of an area of tremor that is not very dense, but extends significantly further downdip than the surrounding regions. These characteristics are unique to the 2009 and 2013 Oregon

events and are not evident in the 2011 and 2016 Oregon events, suggesting that this region may exhibit different preferred modes of slip on the fault on an event-by-event basis.

Discrepancies in the along-strike characteristics of tremor and slip do not seem to be as evident in northern Washington (Fig. 3). For all of the events, areas of increased tremor density appear to be correlated with areas of higher slip. This can be seen particularly well for the 2011, 2012, and 2015 events. However, there does appear to be a small along-dip contrast between tremor and slip in these areas of high slip and tremor density. This is likely the reason for the preferred updip shift of the tremor-derived slip distributions shown in figure 8.

Although individual events might exhibit unique spatial relationships between tremor and slip, looking at cumulative behaviors helps to identify potential systematic differences in tremor and slip both along-strike and along-dip. Figure 9 represents both the cumulative slip, derived from GPS inversions for all the major events, and the total tremor associated with these events. Along-dip profiles in northern Washington show that in the region of high slip on the eastern side of the Olympic Peninsula the cumulative slip is resolved slightly updip of the peak in cumulative tremor distribution. In the region near the Oregon-Washington border, the cumulative tremor has a relatively abrupt updip limit while the slip tapers off further updip. Although the peaks of the cumulative tremor and slip are only slightly offset, the slip extends significantly further updip than the tremor. The peaks of cumulative slip and tremor in Oregon appear to be aligned, although the tremor appears to taper off more abruptly on the downdip side than the slip.

Similar to earlier observations by Schmidt and Gao (2010), one cursory result of the cumulative slip associated with the major ETS events analyzed in this study

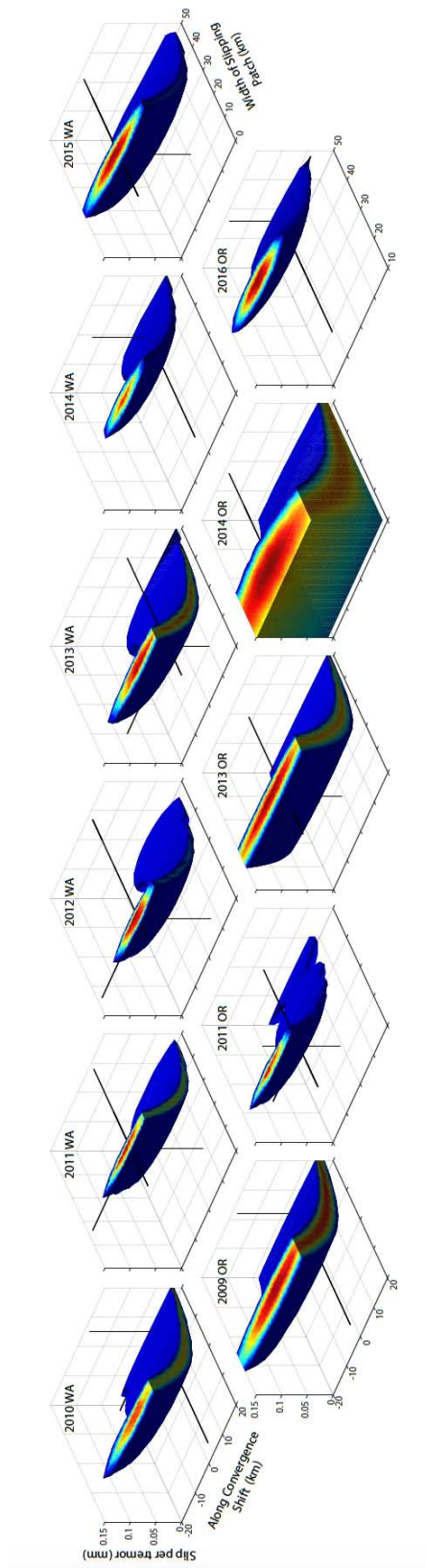


FIGURE 3.8. Total WRMS misfit of the observed surface displacements and displacements predicted by tremor-derived slip models. The colored volumes show the trade-offs between the three input parameters for the tremor-derived slip distributions. The volumes enclose all parameter combinations that result in WRMS values that are within 15% of the minimum WRMS values. Black lines converge on the optimal parameters.

is that the region on the eastern edge of the Olympic Peninsula experiences much more cumulative slip than surrounding areas. The total slip in this region is over twice that of other areas along the subduction zone, such as the area near the Oregon-Washington border. This supports the idea that the overall strain release associated with large ETS events can vary along strike. The cumulative slip in northern Washington during major ETS events only accommodates $\sim 50\text{-}80\%$ of the convergence rate. Assuming inter-ETS tremor represents a similar amount of slip on the fault as larger tremor events, Wech et al. (2009) have suggested that inter-ETS events could account for the remaining slip deficit.

In contrast to northern Washington, the cumulative slip associated with major ETS events in central Oregon only accounts for a maximum of $\sim 60\text{-}65\%$ of the convergence rate. Using 80 years worth of historical tide gauge and leveling records, Krogstad et al. (2016) constrained the maximum interseismic strain accumulation in the region to be 10-20%. This leaves approximately 25% of the convergence rate to either be accommodated during inter-ETS events, or during aseismic creep events. Considering the sparse inter-ETS tremor activity in Oregon (Fig. 1), it is likely that a majority of the remaining convergence rate is accommodated during aseismic creep. This would suggest that the same area of the fault can rupture both seismically and aseismically.

3.5.2. Strainmeter Constraints

Borehole strainmeters provide an independent geodetic constraint for constraining the spatial relationship of tremor and slip. The Plate Boundary Observatory (PBO) provides strain time series data from Gladwin Tensor Strainmeters, which are comprised of 4 independent linear gauges that are arranged along different azimuths

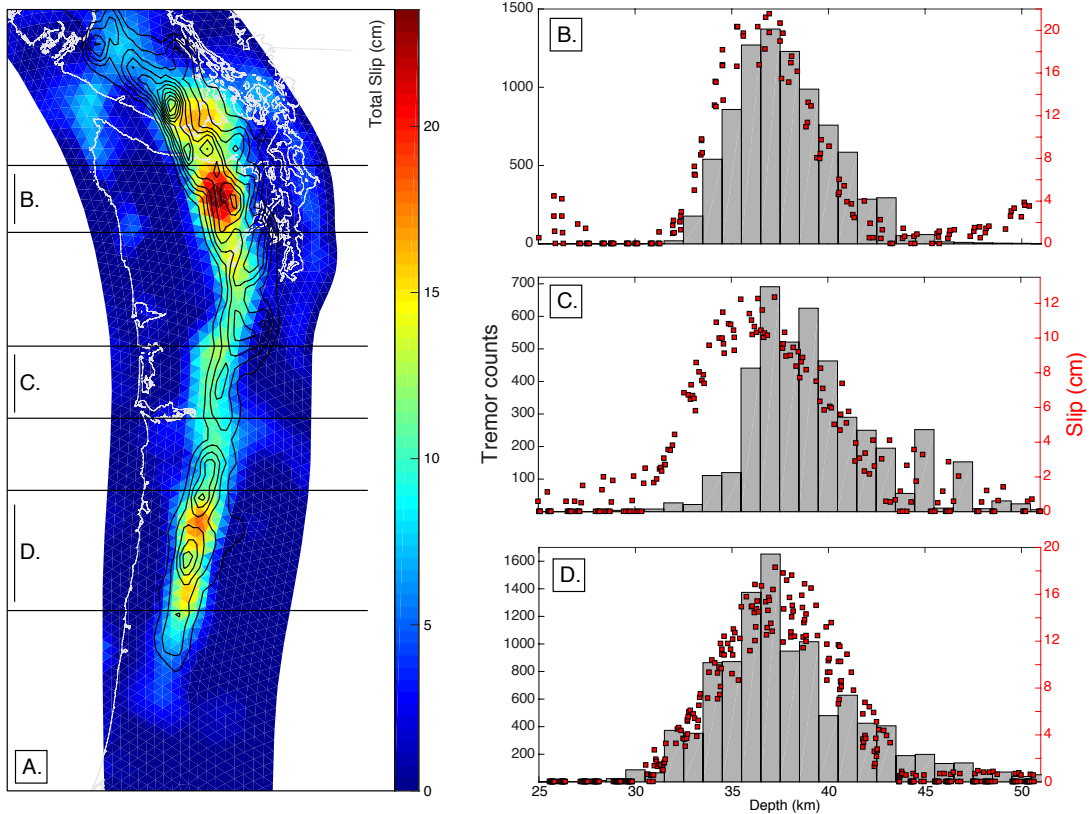


FIGURE 3.9. Cumulative relationship of tremor and slip. A) The total slip associated with all major slow slip events (2009-2016) analyzed in this study as constrained by static offsets in the GPS time series. Black contours show the total tremor density associated with all of the events. Black lines highlight the areas represented in the corresponding profiles. B-D) Grey bars show histograms of cumulative tremor counts from all major events with depth along the three profiles. Red squares present slip on individual fault patches within the boundaries of the profiles indicated in (A).

(Gladwin and Hart, 1985). Three gauges are required to derive differential and shear strains; the fourth gauge provides redundancy. A map showing the location of PBO operated strainmeters in Cascadia is provided in figure 10. The strains are reported in differential strain, where $\gamma_1 = \varepsilon_{EE} - \varepsilon_{NN}$, and shear strain, where $\gamma_2 = 2\varepsilon_{EN}$. The strain data have large non-tectonic signals due to borehole curing, tidal, and atmospheric effects (Roeloffs, 2010; Hodgkinson et al., 2013). These known non-tectonic signals have been removed using the coefficients provided in the processed level 2 data from PBO. Additionally, apparent linear trends have been removed for approximately half of the time series. Finally, the strain data are averaged over daily intervals.

We use the tremor-derived slip distributions to forward model strain at each strainmeter using the optimal area and slip parameter values for each event. To assess a potential offset between tremor and slip, we also show forward modeled strain that results from tremor-derived slip models that have been shifted along the convergence direction. Neither the observed strains nor the predicted strains have been scaled in the comparison. The absolute offset in the strain measurement is not necessarily the most appropriate way to interpret comparisons of observed and predicted strains due to the propensity for strainmeter time series to contain non-tectonic artifacts, the relatively high level of random walk noise over weeks-to-months, and the potential errors associated with the calibration of the instrument (Langbein, 2010). The temporal resolution of strainmeters allows for a more robust daily comparison of tremor and slip, particularly in regards to the relative strain change.

For the 2010 event, strainmeters B004 and B012 appear to be better fit with slip that has been shifted downdip from tremor. The differential and shear strain

components for B004, B007, and B018 appear to show contrasting results. The differential components are better fit with small downdip shifts while the shear components are better fit with updip shifts. An interesting feature of the shear component of B007 and B018, is that the initial strain during the event matches the expected signal from the predicted strain with a downdip shift, but after a couple weeks the observed strain is better predicted with slip that has been shifted updip. These stations are more closely located with the initiation location of tremor for this event. These observations might indicate that slip initiates downdip of tremor, but then propagates updip during the event.

During the 2011 Oregon event, the timing and sign of the strain at B024 seems to indicate an updip shift, but the magnitude of the signal appears to be off by an order of magnitude. This could be due to an area of slip to the north that was identified by Wech and Bartlow (2014). The general shape to the strains at B028 also seems to indicate an updip shift, but artifacts in the data makes drawing definite conclusions from the data problematic. For the 2012 Washington event, B004 is best fit with an updip shift, B007 is best fit with little to no shift in slip, and B012 is best fit with a downdip shift, but the form the observed strain is significantly different than the predictions. The timing of observed strain during the 2016 Oregon event matches well with predicted strain, although the sign and scale of the signals do not match as well. B028 is located near the latitude of the initiation of tremor during this event. In contrast to stations B007 and B018 during the 2010 event, the initial observed differential strain of B028 matches well with the updip shifted prediction, while the later strain matches with the predictions that have been shifted downdip. The total shear strain at B028 is predicted by slip that has been shifted downdip, but the initial strain is not predicted by any of the tremor-derived slip models.

In general, the tremor-derived slip models do an adequate job of predicting observed strains. Discrepancies between the observed and predicted strain are evident both along-strike and along-dip, and even from event-to-event, as is seen at B004 and B012 for the 2010 and 2012 events. Simply shifting the slip in relation to tremor does not provide a systematic improvement in the fits to the observed strain. One benefit of the tremor-derived slip is that it provides a good way to resolve the temporal relationship of tremor and slip. While most time-dependent GPS inversions add an additional temporal smoothing parameter, the temporal aspect of tremor-derived slip models is only dependent on the timing of tremor occurrences (McCaffrey, 2009; Schmidt and Gao, 2010; Bartlow et al., 2011). Of the strainmeter observations presented here, there is a good match between the initiation of tremor and slip, times of peak strain, and times of strain sign changes. This indicates that the incorporation of tremor-derived slip and strainmeter observations helps elucidate the temporal relationship of tremor and slip. In particular, it appears that although slip might occur in areas with little to no tremor, areas with increased tremor density tend to yield higher amounts of slip and that the temporal propagation of tremor and slip are typically highly correlated.

3.5.3. Implications

It is likely that some tremor envelopes represent more or less moment release than others. One of the assumptions in our model of tremor-derived slip, as well as previously mentioned scaling relationships, is that each 5-minute tremor envelope scales with a similar moment of slip. Considering our slip estimates per tremor window already vastly overestimate the actual moment associated with the seismic source patch, this variation is likely insignificant. Additionally, Bostock et al. (2015)

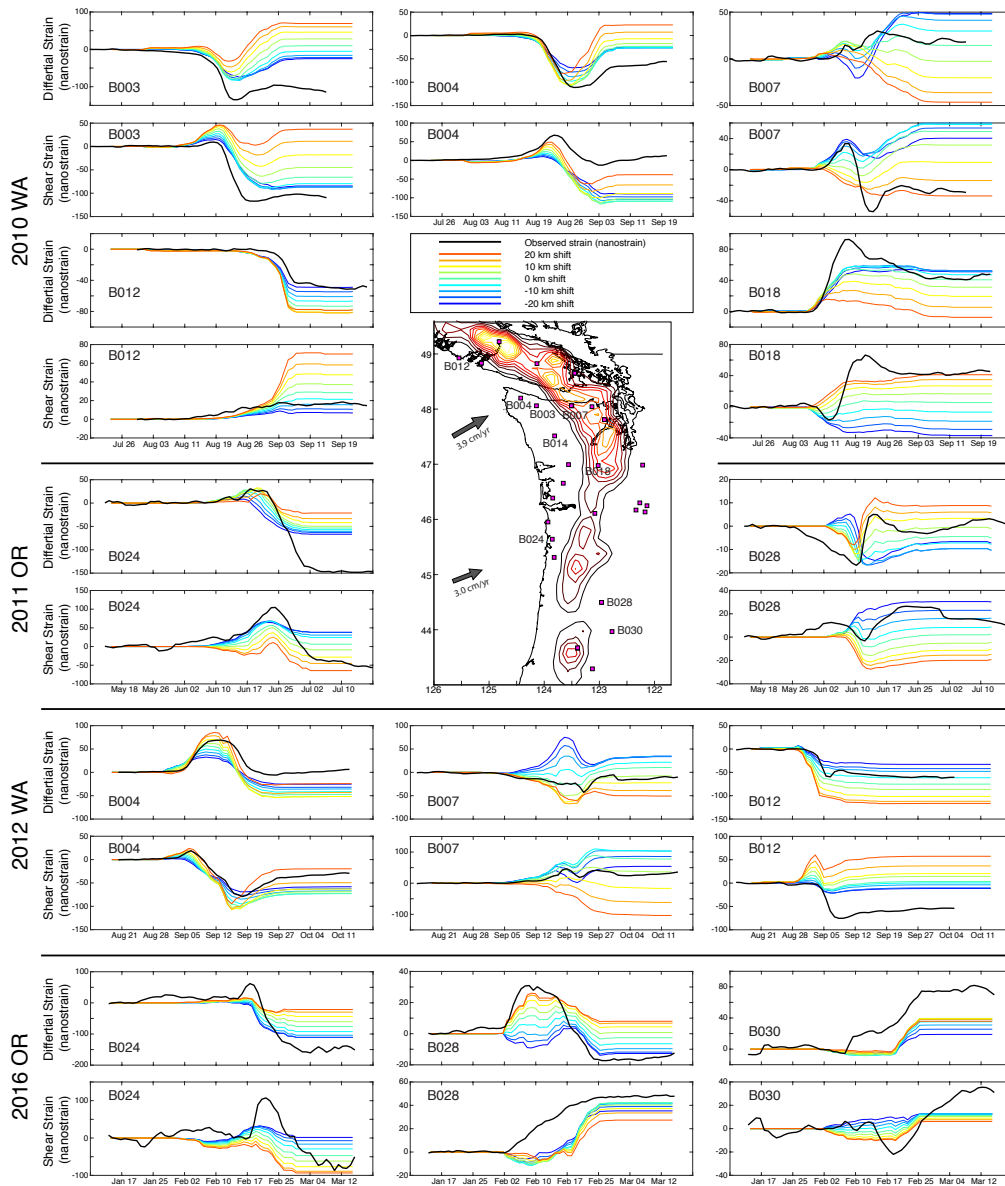


FIGURE 3.10. Observed and modeled strain during multiple ETS events. Black lines show observed strain at selective strainmeter locations during the 2010 and 2012 Washington events and the 2011 and 2016 Oregon events. Colored lines show the modeled strain from the tremor-derived slip distributions. Cool colors represent strain when the slip distributions have been shifted downdip, while warm colors represent an updip shift. Center figure shows a map of all of the Cascadia strainmeter locations. The strainmeters with timeseries shown in the figure are labeled. Contours in the inset map represent the cumulative tremor density during all of the major events analyzed in this study.

found that there is no significant depth dependence in the magnitude of LFEs beneath southern Vancouver Island. However, it may be the case that there is a systematic increase in the moment represented per tremor window with location along dip. If tremor is a superposition of many LFEs, it is possible that the updip tremor is composed of many more LFEs than the downdip tremor, which in turn would represent more moment release. If the updip tremor represents more moment release than the downdip tremor, our model may be biased by placing a disproportionately large amount of moment on the downdip side of the tremor distribution. This bias may explain the small offset of tremor and slip in northern Washington, but it is unlikely to be able to explain the large offset seen near the Oregon-Washington border where the slip extends further updip than most of the detected tremor. This also wouldn't adequately explain the good match of the along-dip extent of tremor and slip in Oregon. In contrast with the possibility that our model is biased by applying more moment release to the downdip extent of tremor, it may be the case that the depth dependent resolvability of locating tremor systematically identifies more tremor on the updip extent of the ETS zone. This would have the opposite effect of the previous argument.

The offset of tremor and slip observed along the southern Washington and northern-most Oregon segment of Cascadia is significantly smaller than offsets observed in other subduction zones, namely Mexico and Alaska. The Middle America subduction zone along Mexico is perhaps the ideal setting for looking at the relationship of tremor and slip. A clear offset has been identified along the Guerrero gap region (Kostoglodov et al., 2010) and the Oaxaca segment (Brudzinski et al., 2010). The Guerrero Gap region is characterized by flat slab subduction once the subducting Cocos plate reaches depths of approximately 40 km (Kim et al.,

2010). Although the dip angle of the slab decreases at a similar depth in the Oaxaca segment, it is not nearly as significant. The detected offset of tremor and slip is much more apparent in the Guerrero Gap area, indicating the dip of the subducting slab could play a role in our ability to resolve the spatial difference in tremor and slip. Additionally, the dip of the fault may play a role in controlling other behaviors near the fault zone, such as fluid migration.

Payero et al. (2008) identified two relatively distinct areas of tremor along the Guerrero Gap; a dense active area on the downdip side with characteristic repeating intervals known as the "sweet spot", and a less dense region on the updip side that is spatially and temporal correlated with long-term slow slip Husker et al. (2012). Stacking continuous GPS measurements during repeating tremor episodes on the downdip side, Frank et al. (2015) identified small-scale slip transients that were associated with the tremor activity in the "sweet spot". This suggests that the total amount of tremor activity does not directly relate to the amount of associated slip, and that the along-dip location can influence the behavior of both tremor and slip.

Applying these observations to Cascadia, we suggest that the relatively small observable offset of tremor and slip is at least partially explained by the steeper dip angle of the subducting slab. This could possibly explain why we don't resolve any offset in Oregon, where the dip angle is about twice as steep as in northern Washington (Supplementary Figure B14). The dip of the subducting slab ultimately controls the horizontal distance at which the slab reaches deeper depths. Tremor and slow slip are thought to represent tectonic deformation along the transitional regime from seismic stick-slip behavior to aseismic stable sliding, which is likely affected by depth-dependent parameters such as temperature, pressure, fluid pressure, etc. (Peng

and Gombert, 2010). The evolution of this transitional regime is simply more readily observable in subduction zones with shallower dip angles.

This explanation does not explain why we see the most significant offset of tremor and slip near the Washington-Oregon border. It could be the case that other factors affect the along-dip extent of slip and tremor in this region; such as a variation in subducted sediments (Calvert et al., 2011), the location of the forearc mantle corner (McCroory et al., 2014), or the effect of the northern termination of the rotating Oregon block (Wells and Simpson, 2001). Ultimately, it is likely that multiple related factors influence the behavior of tremor and slip, while the dip angle serves to influence their relative effect as well as our ability to resolve their distributions.

Previous studies have suggested tremor represents the seismic manifestation of rupture on small asperities that are surrounded by freely slipping regions during SSEs (Ito et al., 2007; Schwartz and Rokosky, 2007; Ghosh et al., 2012). The relative areal ratio of seismic asperities to aseismic freely slipping regions is likely not constant with depth in the ETS zone. The extent of these asperities likely diminishes with depth as the fault transitions to a freely slipping regime. This would explain the shorter recurrence intervals for inter-ETS events that are located further downdip than major ETS events, considering there are fewer, or smaller, asperities resisting continuous slip (Wech et al., 2009). Assuming constant slip, an area with more seismic asperities would produce more tremor in relation to the overall slip than an area with fewer asperities. One possible explanation for slip being imaged updip of tremor could be that there is an updip limit to the location of tremor producing asperities, but not to the slipping region. It is then not necessarily the case that there is a complete offset of tremor and slip, but rather that slip is capable of extending further updip than a significant amount of tremor. This could also explain why many long-term slow

slip events observed in other subduction zones, which are located updip of short-term slow slip, are not imaged with much tremor (Hirose and Obara, 2005; Ochi and Kato, 2013).

3.6. Conclusion

The location and frequency of tremor provides a useful proxy for slip on the fault interface in Cascadia. The use of scaling relationships and subsequent tremor-derived slip models, can provide a useful approximation of the moment release of slip on the fault interface associated with contemporaneous slow slip events. We have shown that tremor-derived slip models can adequately predict surface displacements during major ETS events. However, comparisons with highly sensitive strainmeter observations indicate that using tremor locations as a direct proxy for slip cannot readily resolve many of the small-scale characteristics of slow slip. Analyzing slip inversions of individual SSEs, as well as cumulative slip estimates, we have shown that an along dip offset of tremor and slip likely exists in northern Oregon and Washington. Along strike heterogeneity of tremor and slip also exist along the Cascadian subduction zone, further indicating a regionally specific difference in the behaviors of tremor and slip.

As has been suggested by others, we propose that tremor is likely associated with the seismogenic release of stored strain on asperities along the fault interface, while slow slip is mostly an aseismic process that propagates along with the repeating rupture of closely located seismogenic asperities. While the occurrence of tremor is isolated to these asperities, slow slip can migrate updip, or downdip, of the asperities giving rise to an observable offset of tremor and slip.

3.7. Bridge

In this chapter, I investigated the spatial relationship of tremor and slow slip through the use of newly developed tremor-derived slip models, static inversions of GPS offsets, and strainmeter observations during all the major slow slip events in central and northern Cascadia from 2009-2016. Although the tremor-derived slip models can provide an approximate estimate of the moment release during a slow slip event and can adequately fit GPS displacements, inconsistencies between the geodetic observations and the tremor-derived slip predictions are evident. Both along dip and along strike variability exists between tremor and slip when examined on a fine scale.

In the following chapter, I investigate the temporal and spatial evolution of slow slip during the 2012 event in northern Cascadia by performing a joint time-dependent inversion using GPS and strainmeter observations. Previous studies have used strainmeter observations to indicate slip on the fault, while little work has been done to incorporate the data into an inversion to model slip. In order to incorporate strain measurements into the inversion, I first provide an error analysis of all the known sources of uncertainty in the strain measurements. From here, I investigate the influence including strain measurements into geodetic inversions has on resolving the spatial and temporal propagation of slow slip and its relationship with tremor.

CHAPTER IV

EVALUATING THE SPATIAL AND TEMPORAL EVOLUTION OF SLIP DURING THE 2012 SLOW SLIP EVENT IN CASCADIA USING GPS AND STRAINMETERS

In preparation for submission to *Geophysical Research Letters*. Co-authored with David Schmidt. As lead author, I wrote the manuscript, performed all of the analysis and interpretation, and drafted all the figures for this chapter. My co-author, David Schmidt, helped me with editorial assistance and the interpretation of my results.

4.1. Introduction

Slow slip and nonvolcanic tremor have been observed at several subduction zones worldwide (Gomberg et al., 2010). These events can have recurrence intervals of months-to-years and can last from several days to several years (Schwartz and Rokosky, 2007). In Cascadia, slow slip is almost always accompanied by tremor (Rogers and Dragert, 2003; Aguiar et al., 2009; Wech et al., 2009). Typically, major slow slip events in Cascadia have magnitudes of M_w 6-7, last several weeks, propagate along strike at speeds of 5-10 km/day, and have recurrence intervals of approximately 10-20 months, with the duration of recurrence being dependent on location along strike (Schmidt and Gao, 2010; Brudzinski and Allen, 2007).

The distribution and propagation of Episodic Tremor and Slow slip (ETS) events in Cascadia have primarily been characterized with observations from a broad network of GPS and seismic stations. Many previous studies have inverted surface displacements to derive slip on the fault interface in Cascadia. Static inversions have been performed by Szeliga et al. (2008), Aguiar et al. (2009) and Krogstad and

Schmidt (in prep), while kinematic inversions have been performed by McGuire and Segall (2003), Melbourne et al. (2005), McCaffrey (2009), Schmidt and Gao (2010), Bartlow et al. (2011), Dragert and Wang (2011), Wech and Bartlow (2014). Although the Pacific Northwest now hosts a large network of continuous GPS stations, these inversions still require the application of spatial smoothing constraints, and scatter in the daily averaged GPS time series limits their temporal resolution.

In contrast with the smoothed interpretation of slip, the accompanying tremor in Cascadia is much more complex both temporally and spatially (Wech and Creager, 2008; Ghosh et al., 2009; Boyarko et al., 2015). Tremor consists of repeating clusters, bursts, and down-dip streaks, with some streaks propagating in the opposite direction of the main slip front (Shelly et al., 2007a; Ghosh et al., 2010b; Houston et al., 2011). While tremor is generally recognized as representing shear slip on the fault interface, it remains unclear whether slip is primarily localized to tremor producing asperities, or if slip is a more expansive process and tremor only occurs along isolated patches within a larger slipping area. GPS inversions comparing slow slip and tremor indicate a general correlation between the two on a spatial scale >10 s of kilometers and a temporal scale of days (Dragert and Wang, 2011; Bartlow et al., 2011; Wech and Bartlow, 2014). In an effort to address the detailed relationship of tremor and slip, Hawthorne and Rubin (2013) used strainmeter observations during several major slow slip events to show that slip and tremor are correlated on a sub-daily scale, namely that the amount of slip, and the associated strain, is related to the contemporaneous amount of tremor. While this indicates that a relative amount of tremor can indicate a relative amount of slip, other studies have suggested that some regions of slip may exist without large amounts of tremor (Dragert and Wang, 2011; Wech and Bartlow, 2014).

Borehole strainmeters located in Cascadia provide an independent geodetic constraint for resolving slow slip and provide greater temporal resolution and precision than GPS. Due to their sensitivity, strainmeters are also more susceptible to non-tectonic artifacts, which requires that greater care be taken when interpreting observations. The Plate Boundary Observatory (PBO) operates a network of Gladwin Tensor strainmeters that are capable of measuring horizontal strains at high frequencies and nanostrain precision. These borehole instruments are also equipped with pressure sensors to facilitate the estimation of strain induced by atmospheric conditions.

Previous studies have highlighted the ability of the strainmeters to resolve fine scale details of slow slip in Cascadia. Wang et al. (2008) used the strainmeter B012 to identify and constrain a small slow slip event under Vancouver Island. Dragert and Wang (2011) compared the observed transient strain signals from multiple strainmeters to the strain predicted from a time-dependent inversion of GPS data during the 2008 slow slip event. Wech and Bartlow (2014) used observations from two strainmeters to discern whether slip occurred during a period of low tremor activity for the 2011 slow slip event. Hawthorne and Rubin (2010, 2013) used strainmeter observations to show that strain is correlated with tidal frequencies and the relative amount of tremor, respectively. These studies have primarily been exploratory in nature and have focused on the detection of relative strain changes during slow slip events.

In this paper, we seek to use borehole strainmeter observations in a combined inversion. To our knowledge, this is the first effort to accomplish this goal, which is complicated by the inherent technical challenges when working with strainmeter observations. Our analysis focuses on the 2012 slow slip event in Cascadia, which has

one of the best sets of strainmeter signals. The spatial coverage of the GPS network, coupled with the increased sensitivity and temporal resolution of strainmeters allows for a more complete interpretation of slow slip and its relationship with tremor. Additionally, we characterize the major sources of uncertainty in strain measurements, which is needed in order to properly weight the strain observations in a joint inversion.

4.2. Data

Daily GPS position solutions were obtained from both the Pacific Northwest Geodetic Array (PANGA) and the Plate Boundary Observatory (PBO). The three-component GPS time series were clipped to include a 3-month interval that spans the slow slip event. Trends in the displacements due to interseismic locking along the subduction zone were removed by fitting a linear function to the first 10 days of data before any transients from the slow slip event occur. We omit GPS stations where >50% of the data values are missing or show significant scatter (>3 sigma). Daily error estimates are provided by both PANGA and PBO. In total, 120 stations are used.

Strain data were obtained from a network of borehole Gladwin Tensor Strainmeters maintained by PBO (Gladwin and Hart, 1985). These instruments were installed down \sim 100-250 m deep boreholes and grouted in place, along with a pore pressure and temperature sensor. The strainmeter instruments consist of four linear strain gauges that measure linear horizontal strain aligned at different azimuths. PBO provides level 2 processed data in which the strain gauge measurements have been processed and converted into 3 components of strain; areal strain $\varepsilon_{EE} + \varepsilon_{NN}$, differential shear strain $\varepsilon_{EE} - \varepsilon_{NN}$, and engineering shear strain $2\varepsilon_{EN}$. This requires the conversion of linear strain observations into tensor components

through an inversion that solves for coupling coefficients. In particular, the areal coupling coefficients have been problematic and may not accurately reflect tectonic strains (Roeloffs, 2010; Hodgkinson et al., 2013). Roeloffs (2010) noted that many instruments in the Pacific Northwest do not reliably record areal strains. Therefore, we choose to omit the areal strains from the inversion and focus on the two shear strain components.

We utilize 12 strainmeters in the joint inversion, two of which (B005 and B007) are co-located. Due to their sensitivity, these instruments are highly susceptible to non-tectonic artifacts such as hydraulic loading and other non-tectonic signals (Segall et al., 2003). Strainmeters with significant non-tectonic artifacts (i.e. unexpected steps in the time series) have been omitted. Estimates of strain due to solid and ocean tides, atmospheric pressure changes, and the curing of the grout that couples the instrument to the bedrock have been removed. Additionally, the strain signals have been detrended by fitting a linear function to the data several days before the event.

4.3. Methods

Slip on the subducting Juan de Fuca plate at depth is estimated by incorporating GPS and strainmeter time series data into the time-dependent, Kalman-filter-based Extended Network Inversion Filter (ENIF) (Segall and Matthews, 1997; McGuire and Segall, 2003). The filter incorporates uncorrelated white noise and benchmark motion from geodetic time series while estimating fault slip from spatially and temporally correlated surface deformation. The slip is further constrained by enforcing positivity, as well as temporal and spatial smoothing constraints. The ENIF has successfully been used in several studies of slow slip in Cascadia (McGuire and Segall, 2003;

Schmidt and Gao, 2010; Bartlow et al., 2011; Wech and Bartlow, 2014). A comprehensive description of the filter methodology can be found in McGuire and Segall (2003). Here we provide a brief overview.

The ENIF is an iterative least squares estimator approach where the state variable (which includes all the variables required to describe the system) is predicted and updated for each epoch in the inversion. As it is implemented here, the positions and strains from GPS and strainmeters are modeled as a function of time by the following equation.

$$d_r(x, t) = \int_A s_p(\xi, t) G_{pq}^r(x, \xi) n_\xi dA(\xi) + L_r(x, t) + \epsilon \quad (4.1)$$

Time dependent surface deformation d is related to fault slip s using the Greens functions G_{pq}^r , where p , q , and r represent the slip component, fault element, and deformation component, respectively. n is the unit normal to the fault element surface area A . L is local benchmark motion, which is modeled as random walk, and is scaled by a factor τ . ϵ represents observational error, which is modeled as white noise with zero mean and covariance $\sigma^2 \Sigma$, where Σ is the covariance matrix for the GPS positions and strain observations and σ^2 is the scale factor to account for unmodeled errors.

Fault slip rate is assumed to follow a random walk noise model and is scaled with the hyper-parameter α , allowing for slip to be described as an integrated random walk process and slip accelerations being modeled as white noise. Spatial smoothing is enforced using a Laplacian operator ∇^2 following the methods of Segall et al. (2000) and is scaled using the hyper-parameter γ . Positivity is enforced by introducing a dummy variable λ to set the difference of the slip rate and λ^2 to zero and is scaled by the hyper-parameter ρ (Hel-Or and Werman, 1996).

There are several benefits to using the ENIF (McGuire and Segall, 2003). First, the methodology formally includes a statistical treatment of the data and model parameters. The ENIF can model spatially and temporally correlated deformation by estimating and accommodating the presence of white noise and random walk within geodetic time series, which are specific to individual geodetic sites. Second, we do not have to pre-define the temporal variation of slip, which is critical for slow slip events that occur over multiple weeks and might exhibit variable slip rates. Third, the temporal and spatial smoothing constraints can be optimized by allowing the ENIF to solve for them. This helps to avoid arbitrarily ascribing smoothing values in the inversion. It should be noted however, that although the ENIF can solve for these parameters, it is necessary to have appropriate *a priori* estimates of the state vector and hyper-parameters to initialize the filter, particularly in regards to relative noise and uncertainty levels in the geodetic data.

The fault interface is modeled based on the slab geometry of McCrory et al. (2012) from depths of 20-60 km. The fault model consists of triangular fault elements with areas of approximately 90-100 km² and side dimensions ~ 15 km. Greens functions relating slip on the fault to surface deformation for an elastic half-space are calculated using the boundary element program Poly3d (Thomas, 1993). The rake is defined by the oblique convergence direction of Mazzotti et al. (2007) and Wells and Simpson (2001).

4.4. Strainmeter Error Analysis

The Network Inversion Filter requires approximate a priori estimates of the hyper-parameters to use at the first time step. This includes hyper-parameters that scale the noise of the data. Therefore, it is important to have reasonable estimates

of noise levels to input into the filter. Here we assume the total uncertainty in strainmeter time series is a combination of calibration error and noise inherent in the time series data. We consider four main sources of uncertainty in the strain signals over the duration of slow slip events, namely the statistical white and colored noise in addition to systematic biases from instrument calibration error and instrument orientation error.

Noise in geodetic time series can be described as a power law process of the form

$$P_x(f) = P_o(f/f_o)^n \quad (4.2)$$

Where f is the frequency, P_o and f_o are normalizing constants, and n is the spectral index (Agnew, 1992). White noise is frequency independent and is defined by a spectral index of $n = 0$. Colored noise (i.e. frequency dependent noise) is referred to as power-law noise and is characterized by $n > 0$ values, with the special cases of flicker noise where $n = 1$, random walk where $n = 2$, and integrated random walk where $n = 4$. There is still some debate as to whether multi-year GPS measurements are best described by flicker or random walk models (Langbein and Johnson, 1997; Zhang et al., 1997; Mao et al., 1999; Williams et al., 2004; Amiri-Simkooei et al., 2007; Langbein, 2012). Although the difference in noise models can have a significant impact on uncertainty estimates over multi-year durations (Langbein, 2008), the difference is small over the duration of slow slip events in Cascadia (weeks to months). We treat the overall noise in the GPS times series as a combination of white and random walk noise in the ENIF (Segall and Matthews, 1997).

Although both GPS and strainmeters contain white noise and random-walk error, over the duration of slow slip events (days to weeks) the white noise tends to dominate the net GPS uncertainty, while the random-walk error dominates the

noise in strainmeter data (Langbein, 2010). Over the period of days to weeks the power spectra of strainmeter data can be adequately fit with a random walk model with a spectral index of $n = 2$ (Johnston and Linde, 2002; Langbein, 2010) (Fig. 2). While the noise may be best fit with a different power-law model or an integrated random walk model at longer periods ($>$ year), we assume the frequency dependent noise is random walk and is treated as such in the ENIF.

To estimate the magnitude of the random walk and white noise components in the strainmeter time series data, we calculate the power spectrum for each strainmeter used in this study (Fig. 2, Table 1). The power spectra is calculated from strain data after the previous August 2011 slow slip event and prior to the 2012 event to avoid the effects of large tectonic strains in the spectral analysis. Strainmeters B003, B005, and B927 are analyzed between the 2012 and 2013 events due to uncharacteristically high noise levels in 2011 and early 2012. Strain data that has been flagged by PBO during processing and data that represent significant outliers (i.e. spikes, greater than 5 times the standard deviation of the time series) have been removed and replaced through spline interpolation to facilitate the spectral analysis. The sum of the random walk and white noise components are then fit to the spectra. Methods for fitting the power spectra, such as maximum-likelihood analysis (Langbein, 2004), have been demonstrated. But considering that the ENIF treats the colored noise as a single additional hyper-parameter, we choose to estimate the magnitudes of the noise sources by a simple least-squares fit to a linearized form of the spectra.

At the sampling periods analyzed here (5 minutes to several months), the white noise values are typically <0.20 nanostrain, which is negligible in comparison to the daily uncertainty due to the calibration of the instruments. There are peaks in the power spectra at tidal frequencies for most of the strainmeters due to the effect of

higher order tidal constituents that are not completely removed in the processing (Fig. 2). At higher frequencies than what we include here, the power spectra of these instruments contain peaks due to instrumental noise, such as power sources and the finite precision of the data (Barbour and Agnew, 2011). A majority of the random walk values are between 20 and 50 nanostrain/yr^{1/2} with two anomalously large values of >100 nanostrain/yr^{1/2} due to large transients in the sampled time series data (Table 1). We use an average of the values below 100 nanostrain/yr^{1/2} to estimate the typical random walk value of the strainmeters used in this study, which results in 45 nanostrain/yr^{1/2} to incorporate into the ENIF.

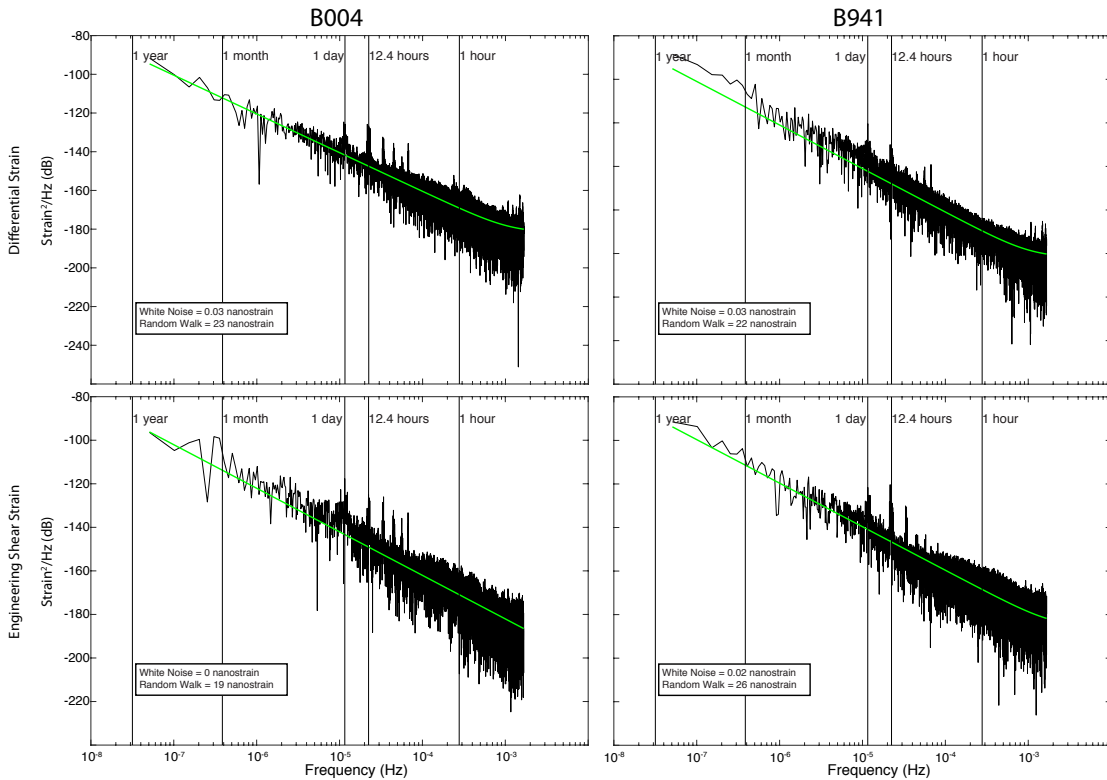


FIGURE 4.1. Power spectra for strainmeters B004 and B941. Green line shows the combine white noise and random walk fit to the spectra. The data has been detrended, and tidal and atmospheric pressure signals have been removed.

| Strainmeter | Component | White Noise (nanostrain) | Random Walk (nanostrain/yr ^{1/2}) |
|-------------|-------------------|-----------------------------|--|
| B003 | Differential | 0.06 | 66 |
| | Engineering Shear | < 0.01 | 37 |
| B004 | Differential | 0.03 | 23 |
| | Engineering Shear | < 0.01 | 19 |
| B005 | Differential | 0.04 | 42 |
| | Engineering Shear | < 0.01 | 30 |
| B007 | Differential | 0.09 | 76 |
| | Engineering Shear | < 0.01 | 40 |
| B012 | Differential | 0.14 | 50 |
| | Engineering Shear | 0.14 | 60 |
| B013 | Differential | 0.2 | 178 |
| | Engineering Shear | 0.09 | 87 |
| B014 | Differential | 0.08 | 72 |
| | Engineering Shear | < 0.01 | 18 |
| B018 | Differential | 0.04 | 22 |
| | Engineering Shear | 0.03 | 35 |
| B022 | Differential | 0.15 | 142 |
| | Engineering Shear | < 0.01 | 97 |
| B926 | Differential | 0.06 | 47 |
| | Engineering Shear | < 0.01 | 23 |
| B927 | Differential | < 0.01 | 31 |
| | Engineering Shear | < 0.01 | 35 |
| B928 | Differential | 0.07 | 58 |
| | Engineering Shear | 0.02 | 54 |
| B941 | Differential | 0.03 | 22 |
| | Engineering Shear | 0.02 | 26 |

TABLE 4.1. White noise and random walk values.

Apart from the noise inherent in the time series data itself, another significant source of uncertainty comes from the calibration of the strainmeters (Hart et al., 1996; Roeloffs, 2010; Langbein, 2010; Barbour and Agnew, 2011; Hodgkinson et al., 2013). These sources of uncertainty are not easily prescribed using a noise model. PBO currently processes strainmeter data using estimates of the strain associated with the

M2 and O1 tidal constituents based on software, such as BAYTAP-G and SPOTL, that calculates theoretical strain values resulting from ocean loading and atmospheric forces (Tamura et al., 1991; Hart et al., 1996; Agnew, 1996, 1997; Roeloffs, 2010; Hodgkinson et al., 2013). This process of calibration works well for strainmeters located in areas where the theoretical tide is accurately calculated by the software packages and where there is little effect from ocean loading (Hodgkinson et al., 2013; Barbour et al., 2015). Data from strainmeters located outside these regions, such as near complicated coastlines and bathymetry, typically have higher levels of uncertainty due to errors in the calibration method (Roeloffs, 2010). Langbein (2010) showed that the theoretical tides can differ by as much as 10-30% from surface-mounted strain measurements. This results in the uncertainty of sub-daily strain transients being dominated by error in the tidal calibration, while the uncertainty of strain transients with durations of >day is dominated by random walk. Despite these errors, Langbein (2010) demonstrated the signal produced by long-term transient signals (greater than a day), such as slow-slip events, can be well resolved. To account for the uncertainty associated with the tidal calibrations, we include an additional component of error into the strainmeter covariance matrix that is approximately equal to 10% of the observed daily strain offset during an ETS event (typically 5-10 nanostrain) which is consistent with Langbein (2010).

The last source of uncertainty we consider is the effect of error in the orientation of the borehole instruments. Although the orientations of all the borehole strainmeters are measured during installation, the magnetic properties of the surrounding rock and casing, and erroneous measurements of the instruments compasses can lead to errors in the actual orientation of the strainmeters (Roeloffs, 2010; Hodgkinson et al., 2013). The same tidal model predictions that are used to

calibrate the strainmeters can also be used to assess their orientation by comparing the predicted and observed phases of the tidal strains. While including the orientation of the instruments as an unknown parameter in the coupling matrix for calibration with tidal strains, Roeloffs (2010) and Hodgkinson et al. (2013) found that several strainmeters might have significant errors associated with their orientation. As was addressed earlier, the tidal models have limitations depending on the location and regional geology of the strainmeters, and errors inherent in the tidal models can propagate into the calibrations of strainmeters. Additionally, Roeloffs (2010) found that the optimal orientation is dependent on the tidal constituent being considered as well as the component of strain.

Alternative methods utilizing known sources of external strains can potentially be used to calibrate and orient strainmeters. Using the strain associated with large teleseismic waves in southern California, Grant and Langston (2009) found that the calibration coefficients used for the PBO strainmeters were generally consistent with the seismic strains. This includes the orientation of the strainmeters, which were typically within 10° of the orientation measured during installation. Unfortunately, due to the sparse coverage of broadband seismometers, a similar investigation has not yet been done in Cascadia.

Of the strainmeters used in this study, B003 and B004 were included in both of the tidal calibration studies, B014, B926, and B941 were included in Hodgkinson et al. (2013), and B005 and B007 were included in Roeloffs (2010). Nevertheless, it is difficult to access what the optimal orientation should be given that there is significant scatter in the corrected orientation depending on the analysis method. Additionally, this leaves five strainmeters used in this study with no independent estimate of orientation. With the exception of B941, all of the preferred model

orientations based on the tidal strain phases fall within 20° of the measured orientation during installation. For these reasons, we add an additional error term for each strainmeter time series that is determined by the range in strain values associated with an orientation change of $\pm 5^\circ$ for each strainmeter to remain consistent with the findings of Grant and Langston (2009) and a majority of the variations found by Roeloffs (2010) and Hodgkinson et al. (2013) (Fig. 2). In terms of differential and engineering shear strain, the rotation equations are

$$\varepsilon_{x_i x_i} - \varepsilon_{y_i y_i} = (\varepsilon_{x_1 x_1} - \varepsilon_{y_1 y_1}) \cos(2\theta_i) + 2\varepsilon_{x_1 y_1} \sin(2\theta_i) \quad (4.3)$$

$$2\varepsilon_{x_i y_i} = -(\varepsilon_{x_1 x_1} - \varepsilon_{y_1 y_1}) \sin(2\theta_i) + 2\varepsilon_{x_1 y_1} \cos(2\theta_i) \quad (4.4)$$

Where ε is the linear strain, and θ_i is the orientation of the strain, counter-clockwise from north. The observed strain is then rotated $\pm 5^\circ$ and the difference between the rotated strains is then incorporated into the daily covariance matrix. This process has little impact on the strain before a major transient, but increases the uncertainty during and immediately after a large strain change (Fig. 2).

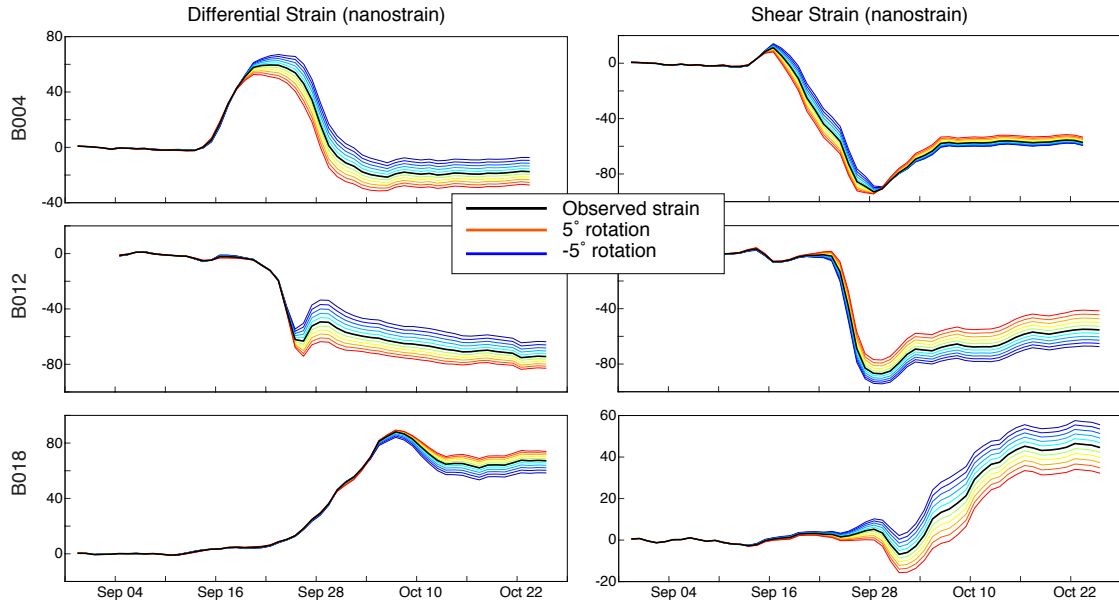


FIGURE 4.2. Rotated strain signals during the 2012 Cascadia slow slip event. Black lines are the observed strain, warm colors have been rotated counter-clockwise in relation of original orientation, and cool colors have been rotated clockwise in relation of original orientation.

In their tidal calibration of B941, Hodgkinson et al. (2013) found that the predicted tidal phases could best fit the observed strains by reorienting the strainmeter $>60^\circ$. This is significantly more than the rest of the strainmeters used in this study. To assess whether B941 provides a reliable estimate of strain change during slow slip events, we compare the observed strain to modeled strain based on tremor data as described in Krogstad and Schmidt (in prep) during the 2010 and 2012 slow slip events. Although the strain signal at B941 is contaminated with a periodic nontectonic signal, the observed strain in 2012 is very similar to what is observed during the 2010 event, suggesting consistency across multiple events and that the long wavelength signal in the differential strain is related to the slow slip events (Fig. 3). When the orientation of the observed strain is rotated, it can do a better job of fitting the predicted strain from the tremor-derived slip model for the 2012 event, but

not the 2010 event. Due to the inconsistency in the fits to the model predictions, we chose to include the original non-rotated strain values into our analysis, but increase the overall uncertainty by a factor of two to account for the additional uncertainty in the orientation.

Although the relative effects vary from strainmeter to strainmeter, the sources of uncertainty and error estimates presented here can be applied to all of the borehole instruments used in this study. However, there are additional sources of error that are not uniformly applicable. Due to their sensitivity, strainmeters contain many nontectonic artifacts. Strainmeters located near the coast are more susceptible to ocean tides that are difficult to model, while strainmeters located near rivers and agricultural areas that use irrigation can contain strain signals of the same order-of-magnitude and duration as signals due to slow slip. These artifacts, coupled with the effect of random walk noise, can make identifying contaminated data difficult, especially if they occur concurrently with slow slip events. Several strainmeters, such as B003, B004, B012, and B018 provide relatively clean data during the 2012 event, while other strainmeters such as B941 are likely affected by external sources of strain.

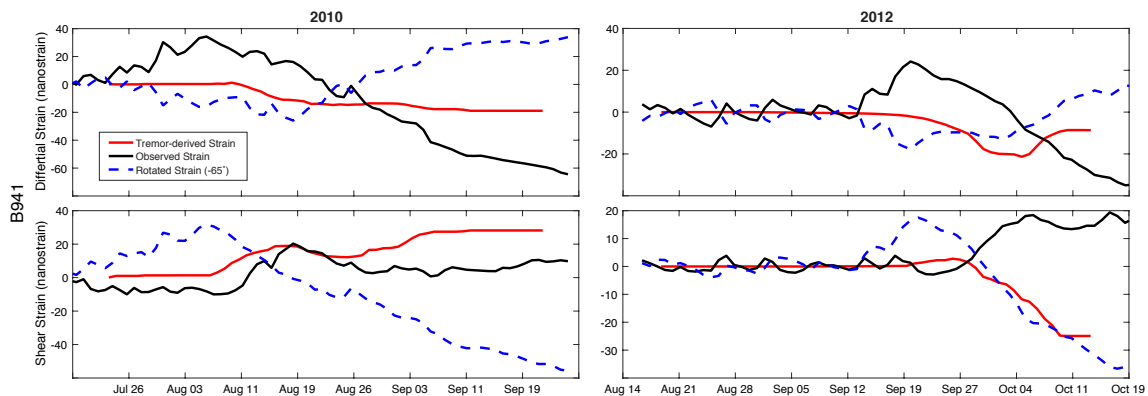


FIGURE 4.3. Differential and engineering shear strain at B941 during the 2010 and 2012 Cascadia slow slip events. Black lines are the observed strain, red lines are strain predicted from a tremor-derived slip model, and blue dashed lines are the observed strain rotated -65° to match the orientation suggested by Hodgkinson et al. (2013).

4.5. Inversion Results

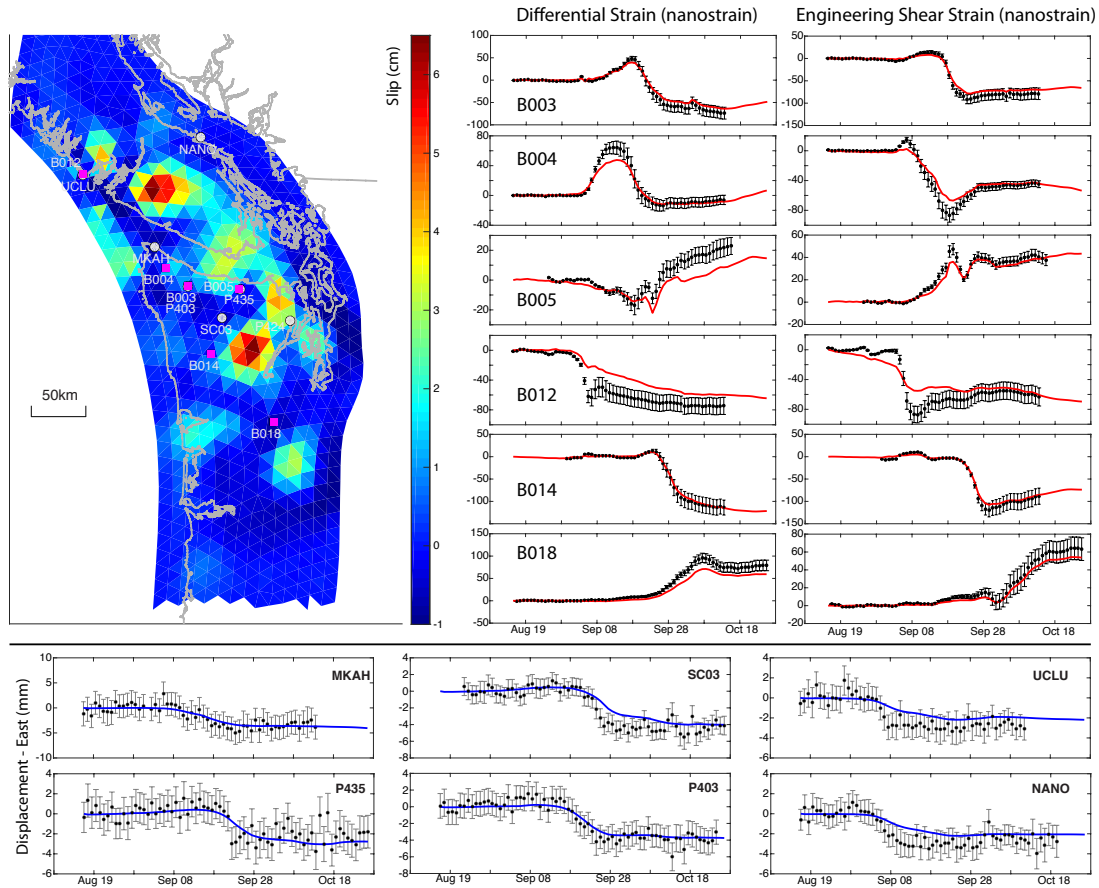


FIGURE 4.4. Results of the time-dependent joint inversion of GPS and strainmeter observations. Top right panels show the observed (black with 1σ uncertainties) and predicted (red) strain at strainmeters indicated on the map. Lower panel show the observed (black with 1σ uncertainties) and predicted (blue) eastern displacements at GPS stations indicated on the map.

The results of the joint inversion can be seen in Figure 4 and Figure C1. The resolved slip is spatially variable along strike, but is generally consistent with the extent and density of tremor provided by the Pacific Northwest Seismic Network (Wech and Creager, 2008). There are a few regions of contrasting results when compared to a similar time-dependent inversion only using GPS data and a static

inversion of the GPS offsets (see chapter 3 for methodology) (Fig. 5). In particular, the joint inversion results in a large amount of slip (up to 6 cm) between 30 and 40 km depth beneath Vancouver Island that is not captured in the GPS-only inversion. This northern region benefits from the increased model sensitivity provided by the strainmeter network (Fig. 6). Even though a large amount of slip is associated with this region beneath Vancouver Island, the observations at strainmeter B012 and the collocated GPS station UCLU are still under-fit and the inversion does not accurately fit the temporal abruptness of the observations (Fig. 4).

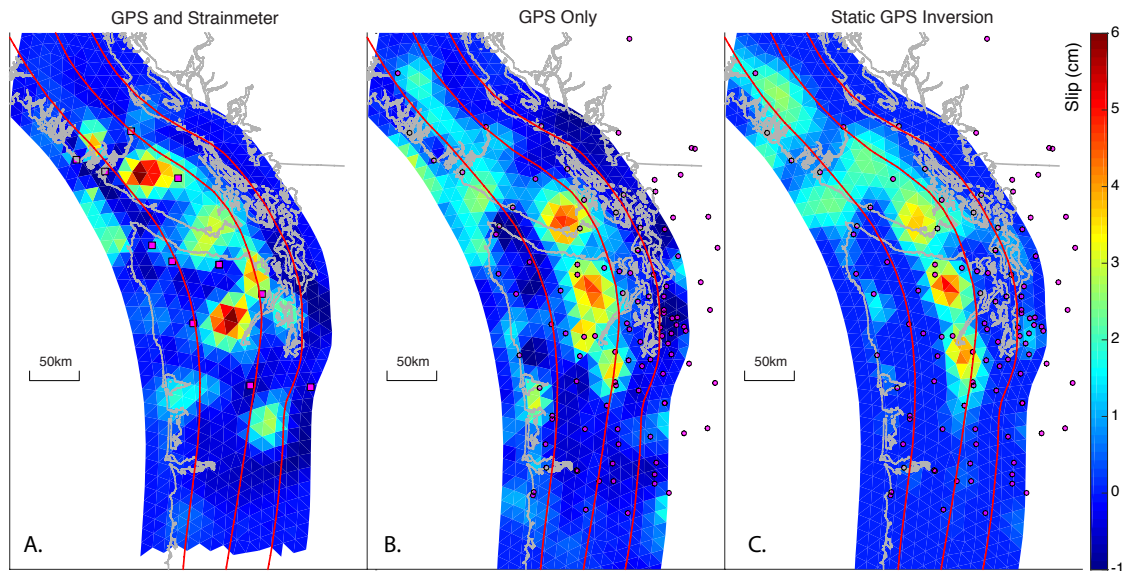


FIGURE 4.5. Comparison of kinematic inversions using GPS and strainmeters (A.), GPS only (B.), and a static inversion of GPS offsets (C.). Magenta squares in A. indicate strainmeters used in the inversion. Magenta circles in the B. and C. indicate GPS locations. Red lines represent slab depth contours of 30, 40, and 50 km respectively.

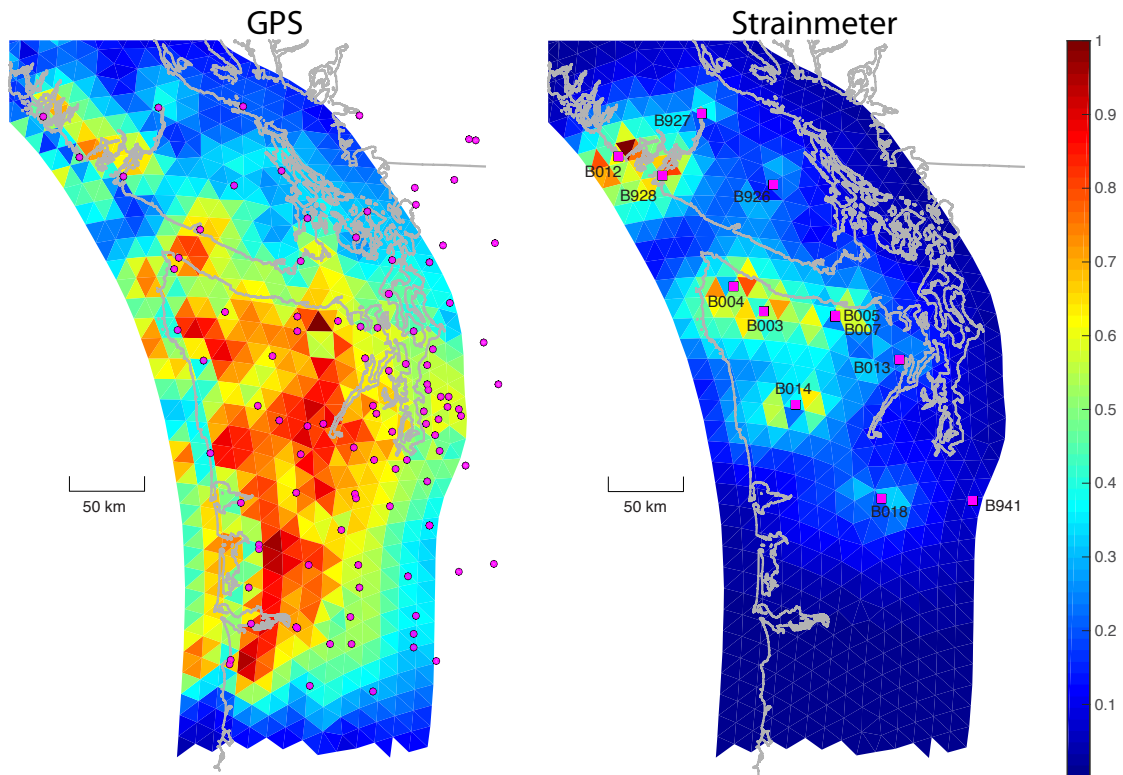


FIGURE 4.6. Model sensitivity. The color of each fault element is associated with the sum of the displacements, or strains, associated with unit slip on the fault patch (Loveless and Meade, 2011). Magenta symbols represent GPS and strainmeter locations.

The inversion results for all combinations of data show a patch of slip under the southern edge of Vancouver Island and the Strait of Juan de Fuca, although the amplitude of this slip patch is relatively higher for the GPS-only kinematic inversion. The slip patch under the Olympic Peninsula has a higher amount of slip and is slightly further south for the joint inversion results. The inversion provides a good fit to the strain observations and nearby GPS stations in this area, of which P435 is collocated with B005 and B007, and P403 is collocated with B003. The joint inversion also results in a small slip patch to the south of Puget Sound that is not imaged in the GPS-only inversions. This region of slip is slightly south of the associated tremor,

although nearby tremor is also located at deeper depths of 40-50 km (Fig. 7 and Supplementary Figure C2-C3). Strainmeters B018 and B941 are located north of this slip patch. The inversion provides a good fit to B018, but B941 is significantly under-fit, which could potentially be due to error in orientation described in the previous section.

Results from the joint inversion show that the propagation of tremor and slip are generally correlated, although slip appears to lag behind the leading tremor front (Fig. 7). There is a relatively large amount of dense tremor at the beginning of the event that is not associated with much slip. The region where tremor initiates continues to slip for several days even after the main tremor front passes. This may be a smoothing artifact of the inversion considering that the temporal aspects of B012 and UCLU time series are not adequately fit.

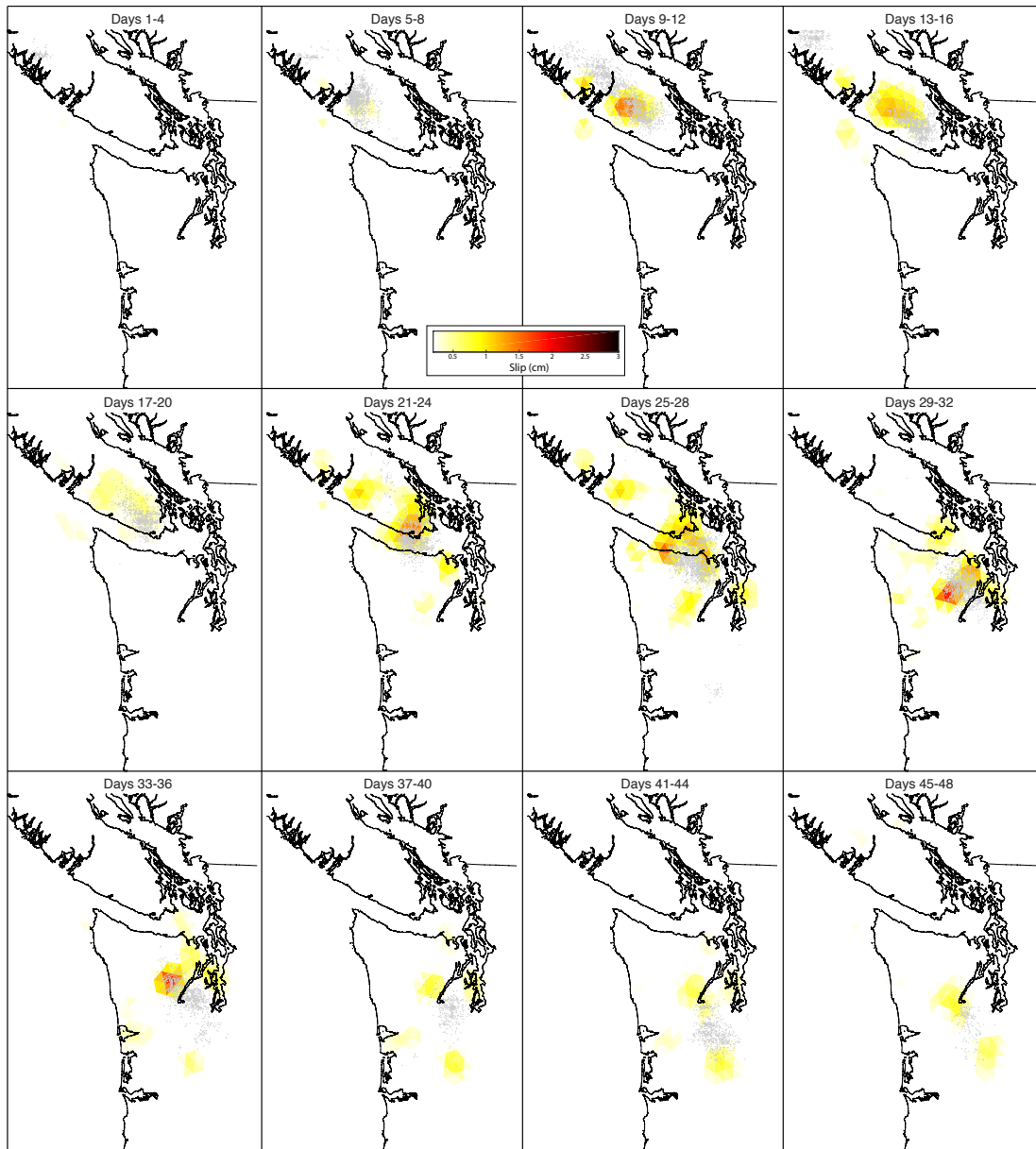


FIGURE 4.7. Temporal evolution of slip during the 2012 slow slip event. Colored patches indicate slip on the fault interface. Grey dots represent tremor.

Although the main tremor front terminates in southern Washington, there is a small burst of tremor in northern Oregon just west of Portland a few days after the main event (Supplementary Figures C2-C3). Using the scaling relationship of

Aguiar et al. (2009), this small amount of tremor would only represent an $\sim M_w$ 5.3. Typically, tremor bursts this small are not associated with much strain change, but observations at the relatively nearby strainmeter B022 show a distinct peak in strain of >50 nanostrain in the differential component during this small tremor burst (Fig. 8). After a brief strain reversal there is a large transient signal over several days of >250 nanostrain in the differential component and >100 nanostrain in the engineering shear component. This large strain signal is significant considering the stable behavior of the strainmeter prior to the small tremor burst, even as tremor from the main front was relatively close. A smaller strain signal can also be observed at B024 which is located to the south of B022, although the noisier data makes it more difficult to discern (Supplementary Figure C4).

When we include the strain from B022 into the joint inversion, a slip patch of 10-15 cm of slip is required to fit the data from B022. The predicted surface displacements from this amount of slip are significantly greater than what is observed at nearby GPS stations, which is why we choose not to include in it the final inversion results. The disproportionately large strain signal could be due to an erroneous calibration of the strainmeter, which is located near the ocean. If this is the case, this observation might indicate that a small amount of aseismic slip that lasted several days was initiated by slip on a small tremor-producing asperity. This is the same region where Wech and Bartlow (2014) inferred aseismic slip during the 2011 ETS event and where it was shown in Chapter 3 that there is a relatively weaker correlation of tremor and slip. Alternatively, the large transient after the spike in strain could be due to pore-fluid interactions near the borehole (Segall et al., 2003). Whatever the source of the large multi-day transient, the temporal correlation of the spike in strain and the small

burst in tremor indicates that even a small amount of tremor can be associated with observable surface deformation.

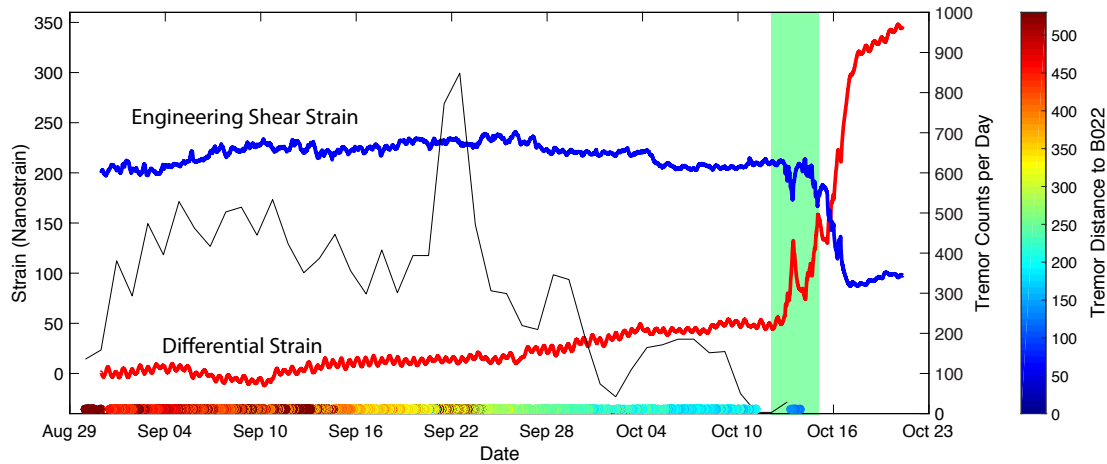


FIGURE 4.8. Observed strain at strainmeter B022 during the 2012 slow slip event. Red and blue lines represent the differential and engineering shear strain components. Black line represents daily tremor activity. Colored dots along the x-axis show the distance of the tremor from B022. Green bar highlights increase in strain during a small burst of tremor.

4.6. Discussion and Conclusion

Observations from the strainmeters included in the joint inversion appear to be generally compatible with observed surface displacements and produce a stable inversion result. This is particularly evident at collocated geodetic instruments. Using observations from similar strainmeters in southern California, Langbein (2015) found that observed coseismic strain changes during the 2014 Napa earthquake differed by up to 30% from the predicted strain associated with the event. Here, with the exception of B941 and B022, all of the strainmeters can be adequately fit within their associated error range in a manner that is consistent with the surface displacements. However, due to the relatively larger scatter and uncertainty in

the GPS observations, this does not exclude the potential for errors in the tidal calibrations for the instruments used in this study.

As has been shown by Ide et al. (2007) and Aguiar et al. (2009), there is a general correlation between the moment associated with slow slip and the duration of tremor. The results from time-dependent inversions allow us to compare the daily moment release of the slow slip event with the daily tremor (Fig. 9). Similar to what can be seen in Figure 7, the tremor precedes the initial increase in rate of moment release. However, the reverse is shown during the middle of the event where there is another increase in the rate of moment release that precedes the spike in tremor activity around September 23. Later in the event, there is a good match between the total tremor activity and the associated moment release. Although there are noticeable temporal offsets between the moment release associated with the joint inversion and tremor activity, the results from the joint inversion provide a much closer match than the results from the GPS-only time-dependent inversion during the early and middle portions of the event. This is likely due to the increased temporal resolution of the strain data. This might also indicate that the difference of the moment release from the joint inversion and the tremor activity is due to biases associated with the inversion process.

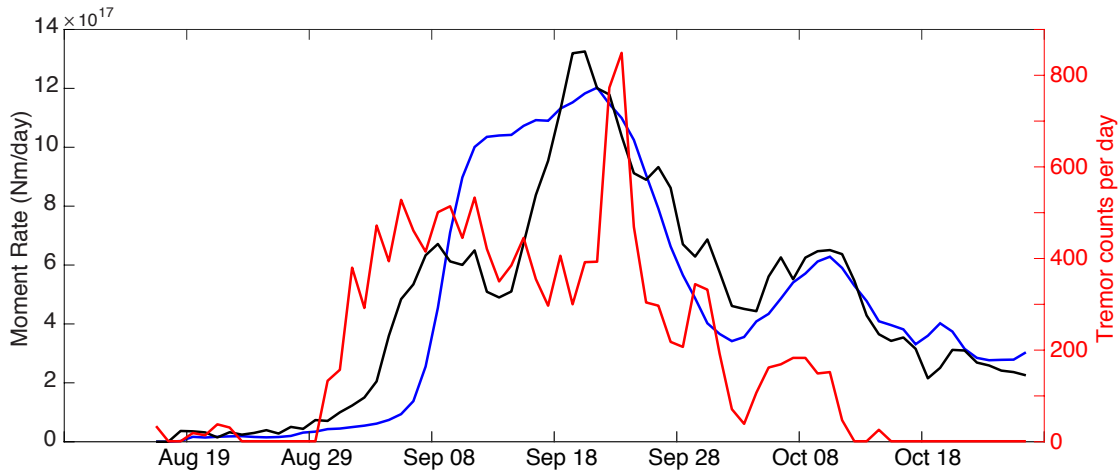


FIGURE 4.9. Rate of moment release associated with the 2012 slow slip event. Black line shows the results from the joint inversion of GPS and strainmeter observations. Blue line is from a GPS-only inversion. Red line represents the daily tremor activity.

An interesting feature of the joint inversion results is that there is not much slip located near a majority of the strainmeters. The slip patch under Vancouver Island matches well with the tremor density, but the slip patches in Washington tend to be offset from the peak tremor density and the slip patches inferred by the GPS-only inversions. This could be due to the fact that slip on the fault results in a more complex strain field than the displacement field. This could mean that the strain values are fit among a range of potential local minima associated with multiple lobes of the strain field. This is a potential source of error when using strain data in inversions, although a series of time-dependent forward models based on the GPS-inversion results may help to discern this possible effect. This may also indicate that the joint inversion is currently weighting the strainmeter data too heavily.

This highlights the relative impact that each geodetic data set has on the inversion. While the spatial coverage of the GPS network provides a better constraint on the location of slip compared to the sparse distribution of reliable strainmeters,

the higher sensitivity of strainmeters provides a tighter constraint near individual strainmeters. However, as we have seen, the higher sensitivity and the complex strain field may provide problematic results. The higher temporal resolution of the strain data provides an improved constraint on the propagation of slip, considering the GPS data is limited by daily scatter in the time series that makes discerning the onset of slip difficult. Lastly, the overall moment is more constrained by the large number of GPS stations and the relatively lower uncertainty in the overall displacements compared to the uncertainty in strain measurements. Together, these two geodetic networks can provide complimentary observations when constraining slow slip, although greater care must be taken when interpreting results when using strainmeters.

While other studies have compared strainmeter observations with forward models, which interpret surface strain observations based on predefined slip models (Wang et al., 2008; Dragert and Wang, 2011); our results show that strainmeters, coupled with GPS, can be used to infer slip on the fault. By including an estimate of uncertainty that accounts for a broad range of error sources, we have shown that combining strainmeter observations with GPS measurements can provide stable inversion results that are consistent between both data sets. This highlights the need for future work to provide better calibration constraints and orientation corrections to fully utilize the potential benefits these instruments provide. Although the inclusion of strainmeter observations has the potential to improve the resolvability of geodetic inversions, our ability to resolve the precise temporal evolution and the small-scale features associated with the complex behavior of tremor is still limited. The underdetermined nature of the inversion, coupled with the limited resolution of the model limits our ability to resolve fine scale features at the level of individual LFEs and tremor. However, incorporating strainmeters into joint inversions can provide an

improved constraint on the propagation and location of large-scale features of slow slip.

CHAPTER V

CONCLUSIONS

5.1. Dissertation Summary

This dissertation uses an array of different geodetic measurements to investigate slow slip and its relationship with the broader subduction zone over a large spatial and temporal range. The overarching theme of this work has been focused on constraining the long- and short-term behavior of the ETS zone. Here I provide a brief summary of each chapter and address future questions and developments pertaining to each project.

In Chapter II, I use GPS, tide gauges, and 80 years of leveling data to investigate potential long-term strain accumulation near the ETS zone. This project highlights the value of using historical data to supplement current geodetic methods. By incorporating all relevant data, it was shown that the region near the ETS zone could exhibit up to 20% partial locking. The accumulated strain has to be released at some point during the megathrust cycle, either through post seismic relaxation, aseismic creep, long-term slow slip events, or during a megathrust event. The potential for slip to extend into the ETS zone, as was seen in Japan (Kato et al., 2012), could have significant implications for large population centers such as Seattle, Portland, and Eugene, which are located near the ETS zone. This emphasizes the importance of improved geodetic monitoring of Cascadia and the continuation and maintenance of historical geodetic data.

Chapter III uses GPS and strainmeters to constrain tremor-derived slip models. These models are then used to investigate the relationship of tremor and slip during

major ETS events. The development of tremor-derived slip models has shown that using tremor as a proxy for slip can adequately fit geodetic observations, although some systematic differences exist along different regions of the fault. Current available tremor catalogs are limited to only providing spatial and temporal constraints of tremor activity. Future work in the development of comprehensive catalogs of LFEs and tremor that contain moment estimates could provide data relevant to improving tremor-derived slip models. The method I have developed assigns the same relative amount of slip to every tremor observation, which results in the slip associated with large slip patches being controlled by the density of tremor. Incorporating individual magnitudes to each event could potentially indicate that some regions of tremor represent more moment release than others and more accurately predict surface deformation.

Lastly, in Chapter IV, I develop an approach to include strainmeter observations into joint time-dependent inversions to investigate the temporal propagation of slip during the 2012 slow slip event. It was shown that, with an appropriate treatment of uncertainty of the strainmeter data, joint inversions can provide stable results that provide consistent estimates of both GPS and strain data. This has provided an improvement in the way strainmeters have previously been used to infer slip on the fault interface. The error analysis of the strainmeter data underscores the importance of improving upon the different sources of error in the strain data, namely the calibration and orientation. Calibration improvements can potentially be made by further developing current tidal models, or by using strain estimates of teleseismic waves that can be measured at the strainmeters as well as nearby seismic stations. Orientation corrections in Cascadia could also potentially be improved by using teleseismic waves, as was suggested by (Grant and Langston, 2009). Overall, the

addition of strain observations into joint inversions provides an independent geodetic constraint that improves our ability to resolve the temporal evolution of slow slip. However, improving the reliability of the strain data can potentially improve our ability to resolve finer scale details of slip.

APPENDIX A

SUPPLEMENTARY MATERIAL FOR CHAPTER II

This section contains a summary of the processing methods for the reported northern Washington leveling data. Supplementary figures, tables, and their associated captions that are referenced in the main text are also included in this section.

A.1. Washington uplift rate analysis

Our analysis of the tide gauge and leveling data in Oregon are fully documented in Burgette et al. (2009). Here we discuss our more recent analysis of the data in Washington.

A.1.1. Tide gauge analysis

Long records of relative sea level change have been collected at the western and eastern ends of the transect along the Strait of Juan de Fuca across Puget Sound, which provide high precision uplift rate estimates. The Neah Bay tide gauge has operated since 1934, and the Seattle tide gauge to the east has been in operation since 1899. There are two other multi-decadal records collected along the Strait of Juan de Fuca at Port Angeles and Port Townsend, which began in the 1970s.

Following our previous analysis strategy used for the Oregon portion of Cascadia (Burgette et al., 2009), we estimate relative uplift rates using a network adjustment approach, updated to better account for temporal and spatial correlations of noise in tide gauge time series, following Burgette et al. (2013). We use a rate of geocentric

sea level rise consistent with vertical stability of the Seattle tide gauge and regional sea level reconstructions (Burgette et al., 2009).

A.1.2. Leveling analysis

The National Geodetic Survey surveyed benchmarks with first-order leveling practices in at least two epochs along the Strait of Juan de Fuca. The initial observations were made in the early 1930s and 1940s and the most recent extensive survey was conducted in the mid-1970s. Repeated observations of benchmark height exist along the entire profile; however, there is an 11-year gap between the early surveys in the western and central parts of the profile, and all three surveys do not overlap on any benchmarks. Consequently, we reference the relative uplift rates from differenced leveling lines to the rate of relative uplift rate from the sea level analysis at the tide gauge in each section. Uncertainties of benchmark deformation vertical deformation rates are propagated from the relative tide gauge analysis and precisions of the relevant survey lines following Burgette et al. (2009). Uncertainty of the final geocentric uplift rate estimates includes the contribution from the geocentric sea level rise (Burgette et al., 2009).

The spatial trend of uplift rates in the western part of the profile, which is referenced to the Neah Bay vertical deformation rate, is consistent with the trend of the data from the central portion of the profile, which are tied to the Port Angeles tide gauge. This consistency suggests there is little systematic error in the uplift rates along the profile and the leveling random error model accurately characterizes the survey-related uncertainty in uplift rates.

On the east side of Puget Sound, the long-running Seattle tide gauge lies 50 to 70 km south of the 48 N latitude of the profile. We difference first order leveling

lines observed in 1974 and 1915 to estimate uplift rates at the latitude of the Strait of Juan de Fuca profile. These eastern benchmarks are consistent with vertical stability on the eastern end of the profile over the past century.

A.2. Figures

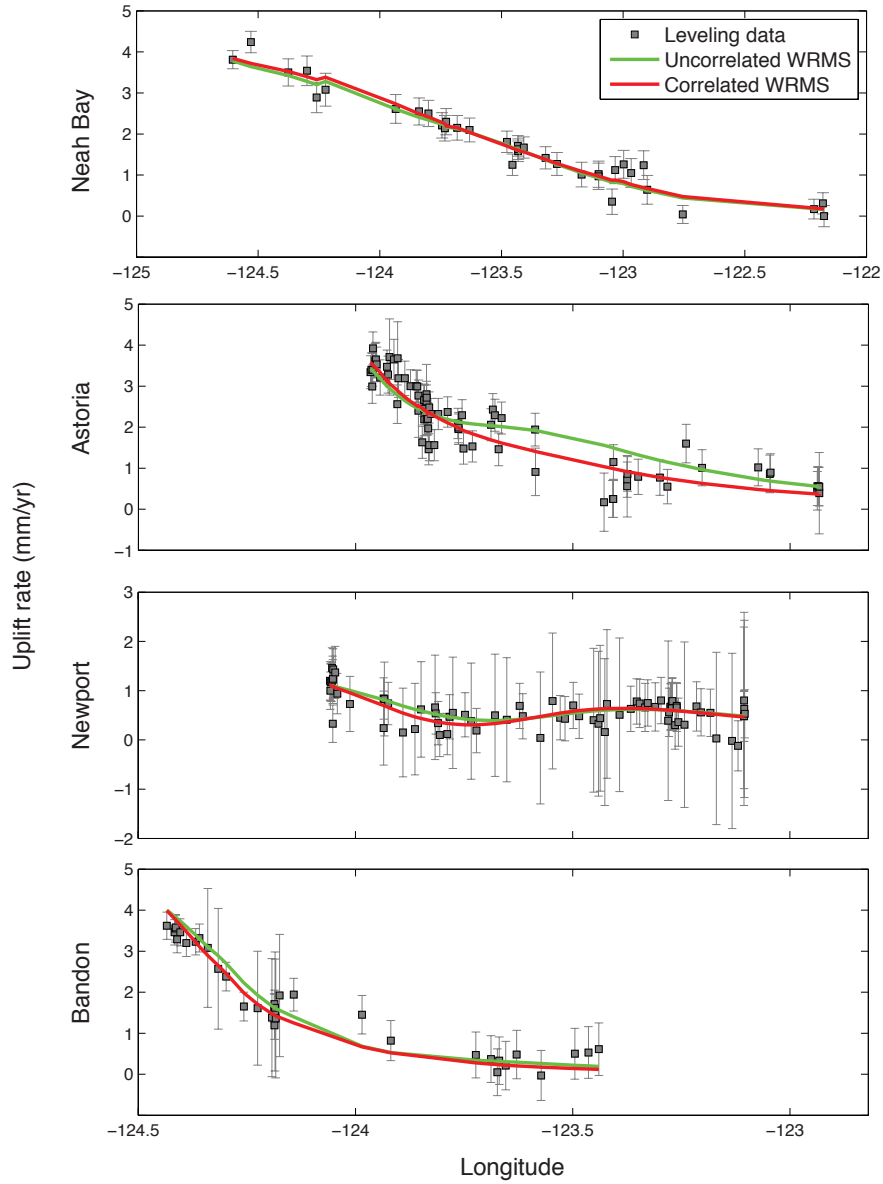


FIGURE A.1. Modeled fit results of the leveling profiles along Cascadia treating nearby leveling benchmark errors as correlated and implementing a full covariance in the optimization. Red and green lines indicate the best-fit modeled uplift rates at each leveling benchmark with and without including locking near the ETS zone respectively.

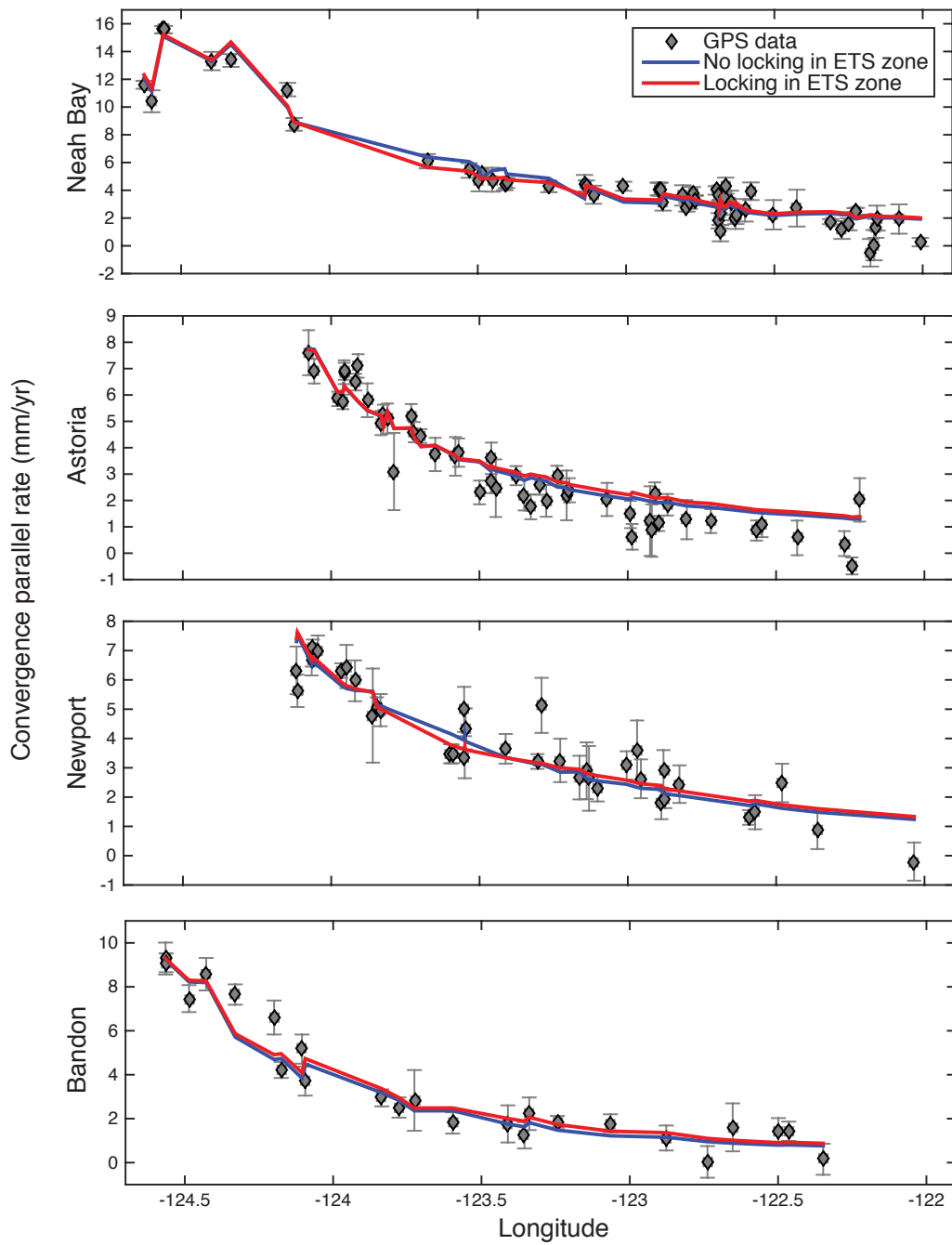


FIGURE A.2. Modeled fit results of the convergent parallel GPS velocities along the leveling profiles. Red and blue lines indicate the best-fit modeled velocities at each station with and without including locking near the ETS zone respectively. Error bars are one sigma.

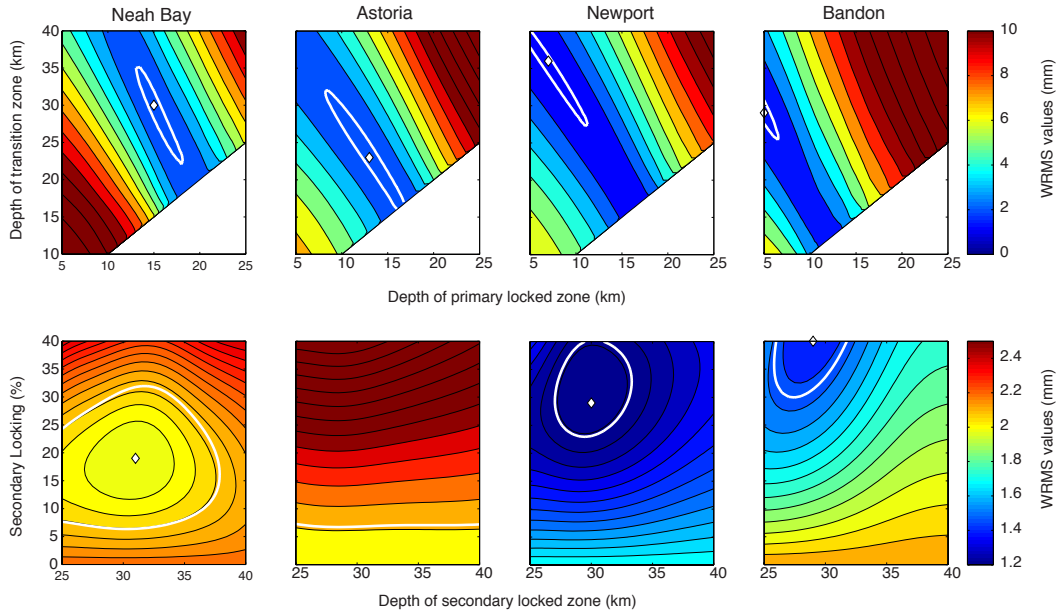


FIGURE A.3. Weighted root mean square (WRMS) misfit plotted as a function of model parameters for convergent parallel GPS velocities along the four leveling profiles. (a) Depths of the locked zone and transition zone. White areas fall outside of the modeled parameter space. (b) Depth and magnitude of secondary locking near the ETS zone. White diamonds mark the optimal fits. Acceptable models fall within the white contours, which encircle WRMS values within the 70% confidence level of the minimum WRMS.

A.3. Tables

| Leveling Results | | Primary locked zone depth (km) | Transition zone depth (km) | Secondary locking (%) | Secondary locked zone depth (km) | WRMS | Correlated WRMS |
|-------------------------|--------------|---|----------------------------------|-----------------------------|---|------|--------------------|
| Neah Bay | Uncorrelated | 17 | 35 | 4 | 33 | 0.80 | |
| | Correlated | 17 | 34 | 6 | 31 | | 4.80 |
| Astoria | Uncorrelated | 19 | 23.5 | 12 | 27 | 0.96 | |
| | Correlated | 21 | 21 | 27 | 27 | | 2.17 |
| Newport | Uncorrelated | 9.5 | 28.5 | 17 | 31.5 | 0.41 | |
| | Correlated | 8 | 31 | 15 | 33 | | 0.85 |
| Bandon | Uncorrelated | 10.5 | 18 | 0 | na | 0.57 | |
| | Correlated | 11 | 18 | 2 | 25 | | 2.02 |

TABLE A.1. Comparison of results assuming uncorrelated errors associated with the leveling data with results based assuming correlated errors.

| GPS Results | Neah Bay | Astoria [#] | Newport | Bandon |
|--|----------|----------------------|---------|--------|
| No Locking in ETS zone | | | | |
| Locked zone depth (km) | 13.5 | 13 | 5* | 5* |
| Transition zone depth (km) | 36.5 | 23.5 | 44 | 32.5 |
| WRMS (mm/yr) | 2 | 2.01 | 1.18 | 1.84 |
| Including Locking in ETS zone | | | | |
| Locked zone depth (km) | 15 | 12.5 | 7.5 | 5* |
| Transition zone depth (km) | 30 | 23 | 34.5 | 29 |
| Optimal ETS zone locking (%) | 19 | 10 | 31 | 40* |
| Depth ^{\$} of ETS zone locking | 31 | 26.5 | 29.5 | 29 |
| WRMS (mm/yr) | 1.98 | 2.11 | 1.14 | 1.39 |
| Statistically Significant [^] (90%) | No | na | No | Yes |

TABLE A.2. Model fits of the GPS data with and without including locking near the ETS zone.

The Astoria profile is better fit with no secondary locking. The secondary locking values are included to show that 10% secondary locking provides a statistically similar fit.

* Results are at the edge of the modeled parameter space.

\$ Midpoint depth of Gaussian secondary locking distribution.

[^] Statistical significance is calculated using an F-test.

| Latitude | Longitude | Rate (mm/yr) | Uncertainty (mm/yr) | Distance to TG (km) | pid | Tide Gauge | Epochs |
|----------|------------|-----------------|------------------------|------------------------|--------|-------------|-----------|
| 48.19000 | -124.22278 | 3.08 | 0.40 | 41.59 | TS0077 | NeahBay | 1975-1943 |
| 48.25472 | -124.25944 | 2.89 | 0.37 | 32.63 | TS0092 | NeahBay | 1975-1943 |
| 48.26361 | -124.29944 | 3.54 | 0.36 | 28.81 | TS0098 | NeahBay | 1975-1943 |
| 48.28306 | -124.37583 | 3.50 | 0.33 | 21.69 | TS0115 | NeahBay | 1975-1943 |
| 48.34833 | -124.52972 | 4.24 | 0.26 | 7.18 | TS0137 | NeahBay | 1975-1943 |
| 48.36694 | -124.60417 | 3.81 | 0.22 | -0.00 | TS0150 | NeahBay | 1975-1943 |
| 48.02278 | -122.99778 | 1.26 | 0.34 | 39.03 | TR0590 | PortAngeles | 1975-1932 |
| 48.05028 | -122.96694 | 1.05 | 0.35 | 43.12 | TR0594 | PortAngeles | 1975-1932 |
| 48.05389 | -122.90083 | 0.64 | 0.35 | 45.05 | TR0602 | PortAngeles | 1975-1932 |
| 48.05278 | -122.91556 | 1.24 | 0.35 | 46.58 | TR0603 | PortAngeles | 1975-1932 |
| 48.11389 | -123.47750 | 1.81 | 0.26 | -4.73 | TR0774 | PortAngeles | 1975-1932 |
| 48.11944 | -123.45500 | 1.25 | 0.26 | -2.48 | TR0776 | PortAngeles | 1975-1932 |
| 48.11972 | -123.43139 | 1.58 | 0.25 | -0.21 | TR0792 | PortAngeles | 1975-1932 |
| 48.11861 | -123.43139 | 1.63 | 0.25 | -0.00 | TR0794 | PortAngeles | 1975-1932 |
| 48.10944 | -123.40833 | 1.67 | 0.26 | 2.89 | TR0796 | PortAngeles | 1975-1932 |
| 48.11611 | -123.43250 | 1.71 | 0.25 | 0.38 | TR0797 | PortAngeles | 1975-1932 |
| 48.10694 | -123.31861 | 1.42 | 0.27 | 9.86 | TR0812 | PortAngeles | 1975-1932 |
| 48.10694 | -123.27194 | 1.27 | 0.28 | 13.16 | TR0817 | PortAngeles | 1975-1932 |
| 48.09333 | -123.17083 | 1.01 | 0.30 | 21.12 | TR0832 | PortAngeles | 1975-1932 |
| 48.07806 | -123.10083 | 1.02 | 0.32 | 27.92 | TR0847 | PortAngeles | 1975-1932 |
| 48.07972 | -123.10083 | 0.97 | 0.32 | 28.11 | TR0848 | PortAngeles | 1975-1932 |
| 48.08028 | -123.04528 | 0.35 | 0.31 | 26.71 | TR0851 | PortAngeles | 1975-1932 |
| 48.04639 | -123.03278 | 1.12 | 0.33 | 34.65 | TR0868 | PortAngeles | 1975-1932 |
| 48.15833 | -123.93444 | 2.61 | 0.35 | -44.76 | TR0892 | PortAngeles | 1975-1932 |
| 48.15083 | -123.83833 | 2.55 | 0.33 | -35.13 | TR0902 | PortAngeles | 1975-1932 |
| 48.13972 | -123.80000 | 2.50 | 0.32 | -31.40 | TR0905 | PortAngeles | 1975-1932 |
| 48.13611 | -123.74444 | 2.21 | 0.31 | -27.05 | TR0909 | PortAngeles | 1975-1932 |
| 48.16111 | -123.72722 | 2.30 | 0.32 | -29.89 | TR0912 | PortAngeles | 1975-1932 |
| 48.13639 | -123.73250 | 2.14 | 0.31 | -26.03 | TR0915 | PortAngeles | 1975-1932 |
| 48.12250 | -123.68222 | 2.15 | 0.30 | -21.84 | TR0922 | PortAngeles | 1975-1932 |
| 48.11806 | -123.63111 | 2.10 | 0.29 | -17.91 | TR0926 | PortAngeles | 1975-1932 |
| 48.11250 | -122.75500 | 0.04 | 0.22 | -999.0 | PT_tg | PortAngeles | 1975-1932 |
| 47.97944 | -122.21556 | 0.17 | 0.24 | 52.05 | SY0003 | Seattle | 1974-1915 |
| 48.10000 | -122.17417 | 0.00 | 0.26 | 68.19 | TR0177 | Seattle | 1974-1915 |
| 48.05139 | -122.17917 | 0.31 | 0.26 | 62.27 | TR0186 | Seattle | 1974-1915 |

TABLE A.3. Northern Washington uplift rates.

APPENDIX B

SUPPLEMENTARY MATERIAL FOR CHAPTER III

This section contains the supplementary figures for Chapter III.

Figures A1–A11. These figures contain details of the individual events analyzed in Chapter III. Slip distributions from GPS inversion and tremor locations include GPS locations that are shown in the top left panel. The inversion sensitivity is calculated following the methods of Loveless and Meade (2011).

B.1. Figures

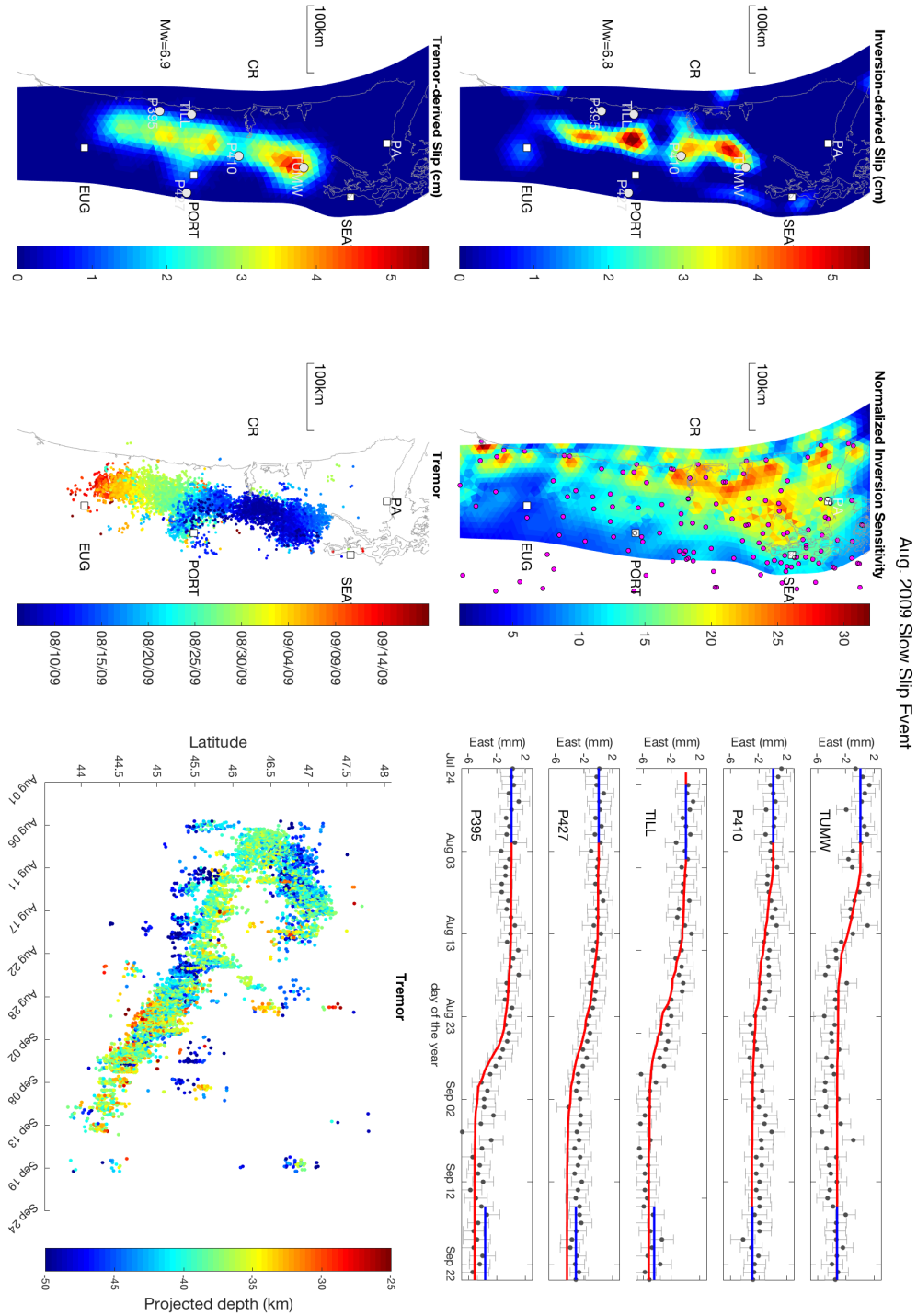


FIGURE B.1. 2009 Oregon (August).

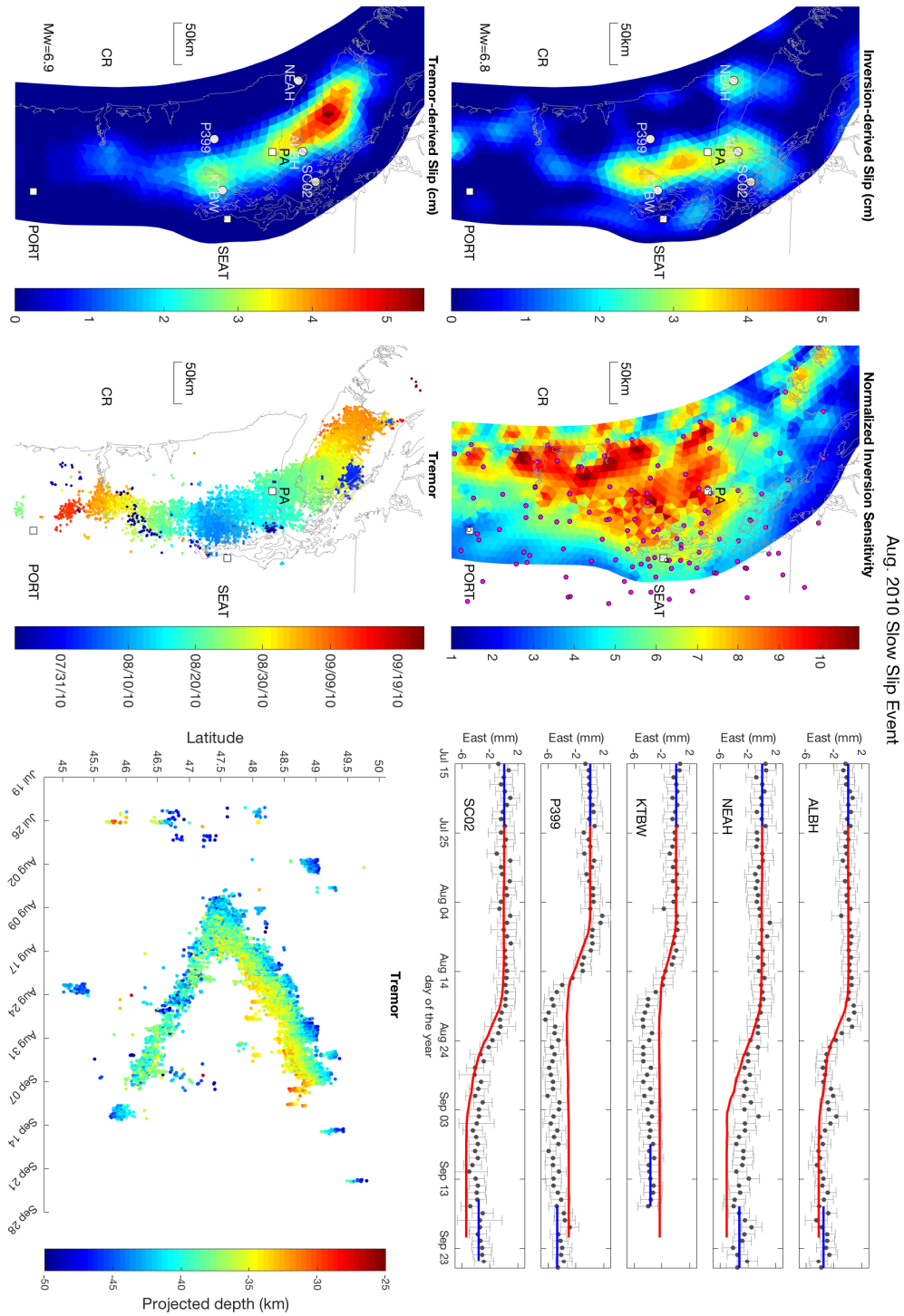


FIGURE B.2. 2010 Washington (August).

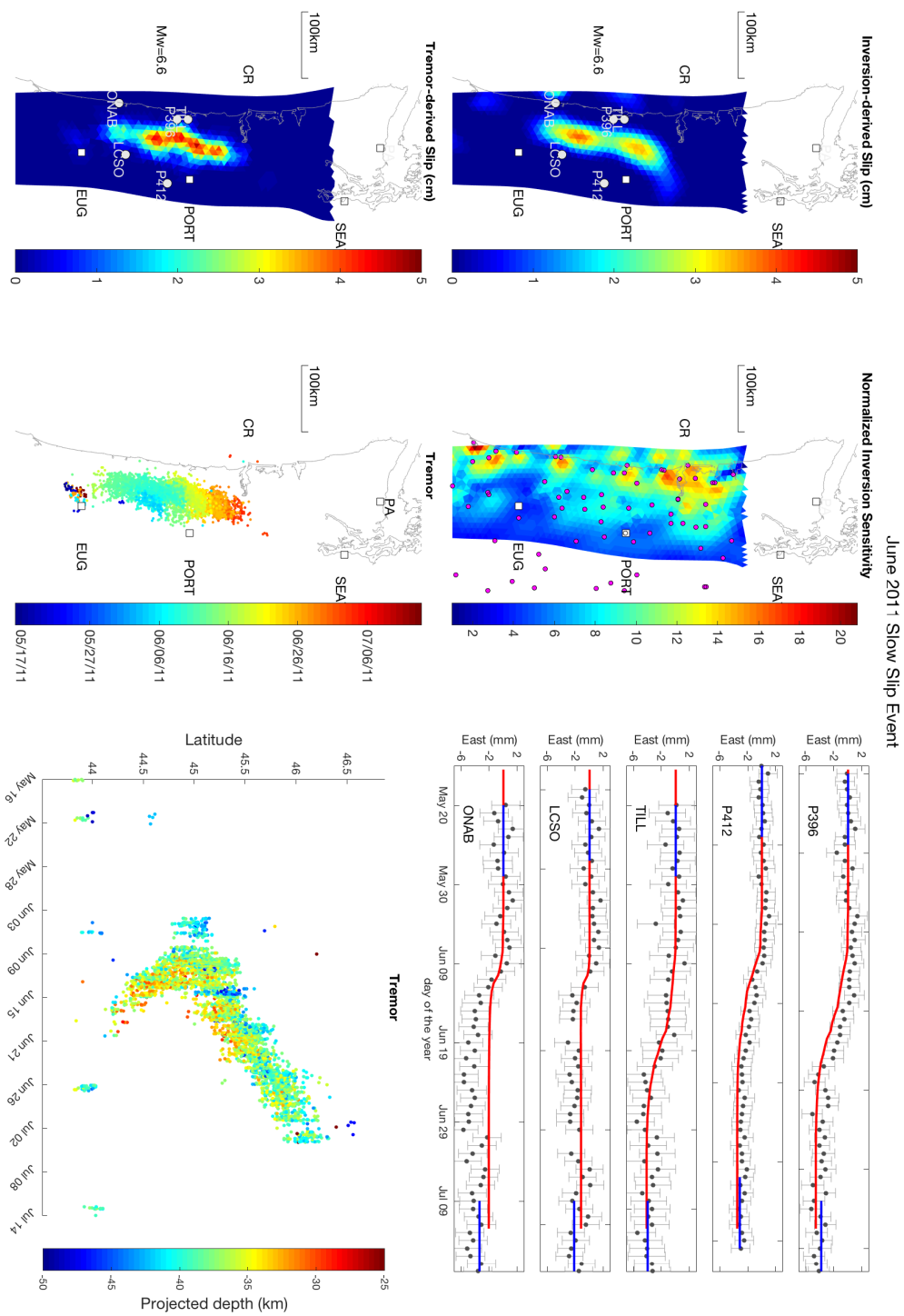


FIGURE B.3. 2011 Oregon (June).

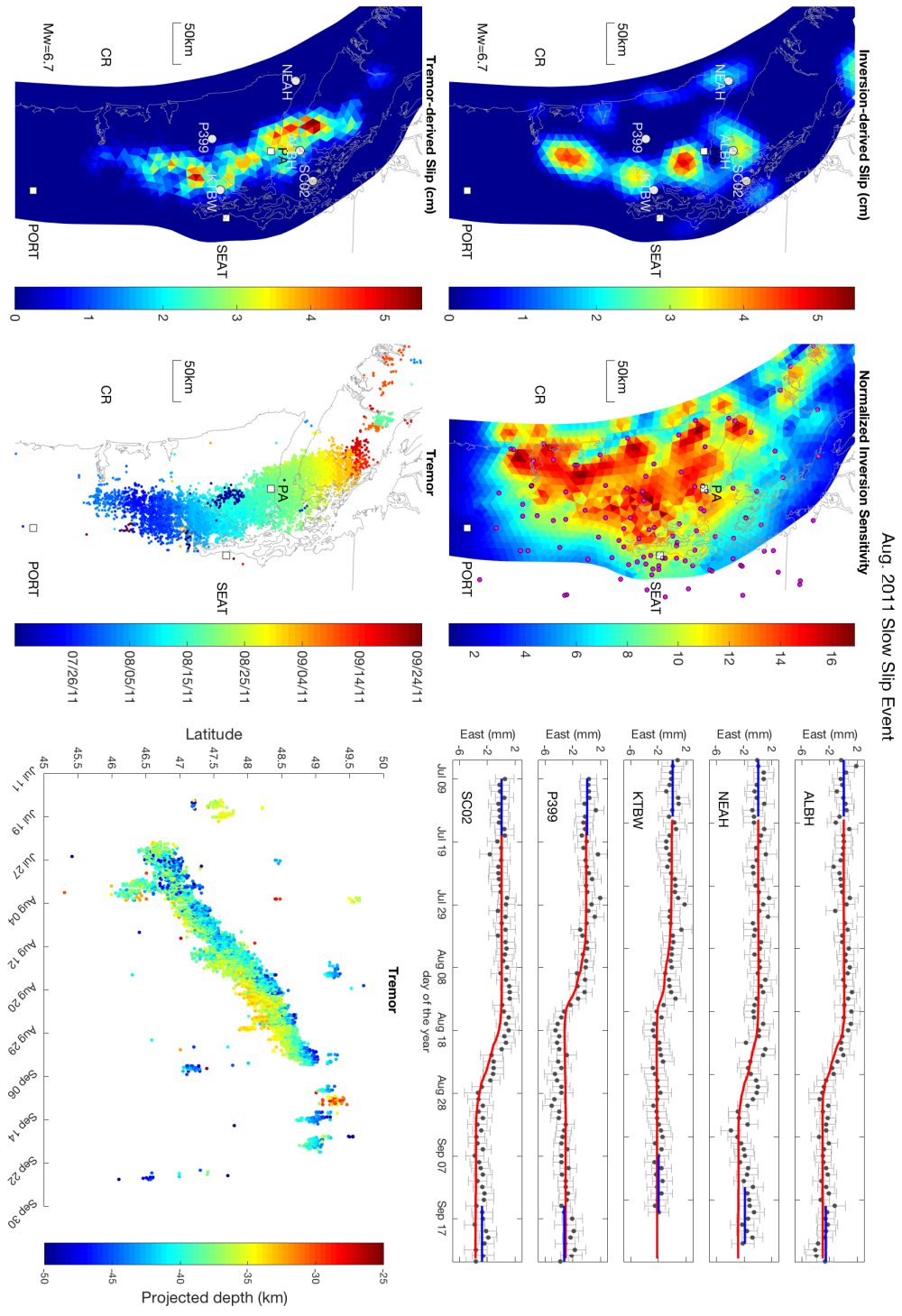


FIGURE B.4. 2011 Washington (August).

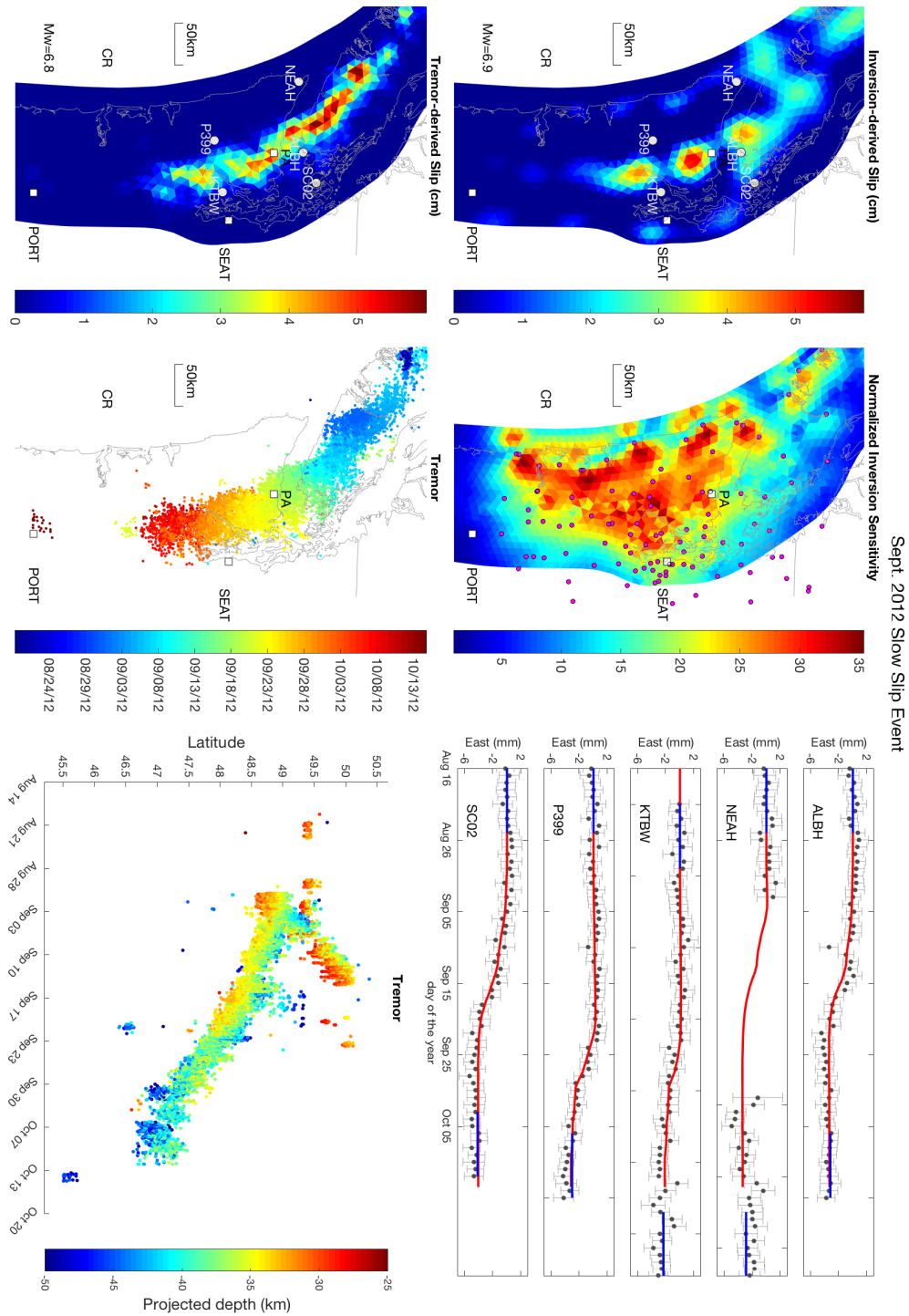


FIGURE B.5. 2012 Washington (September).

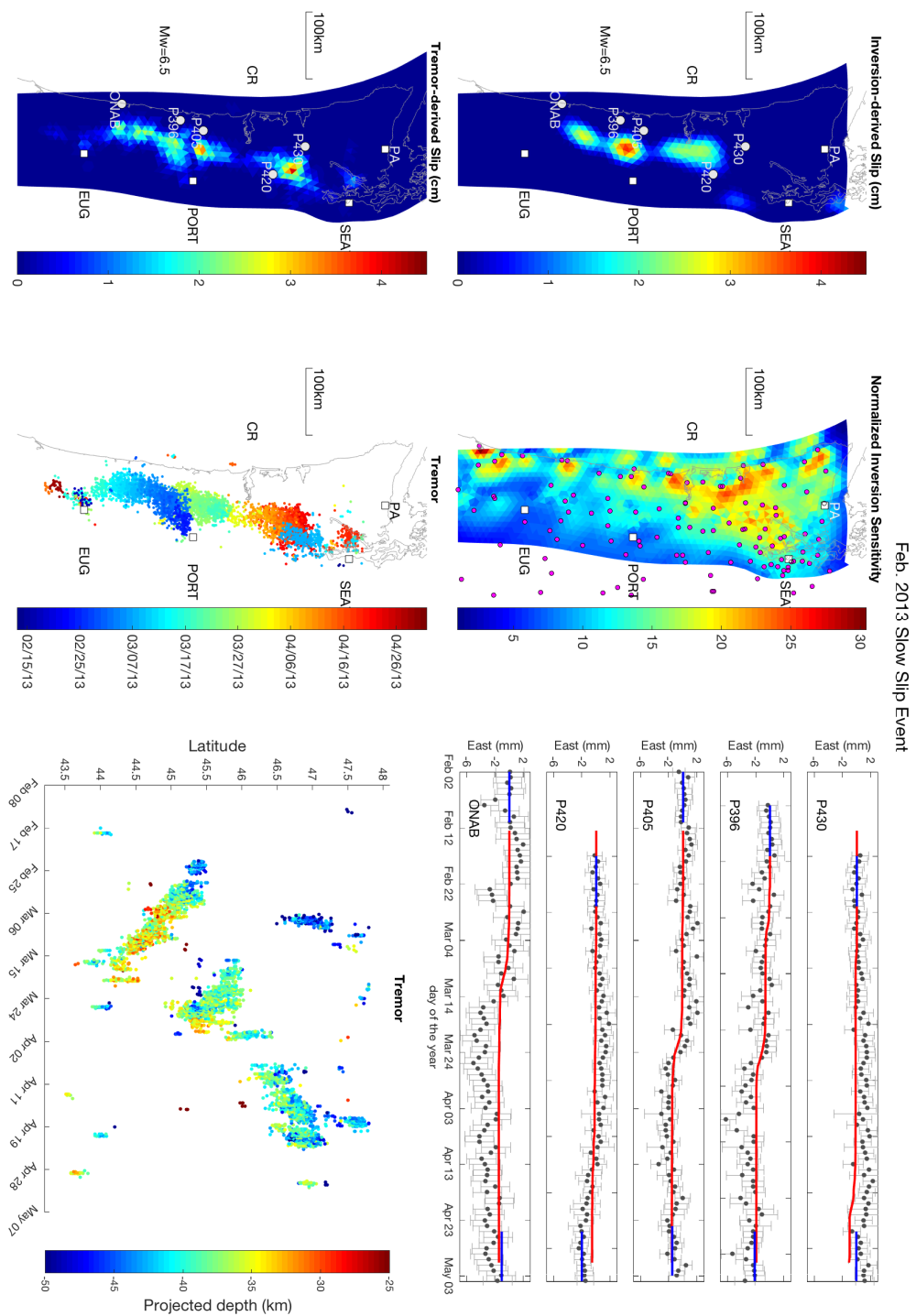


FIGURE B.6. 2013 Oregon (February).

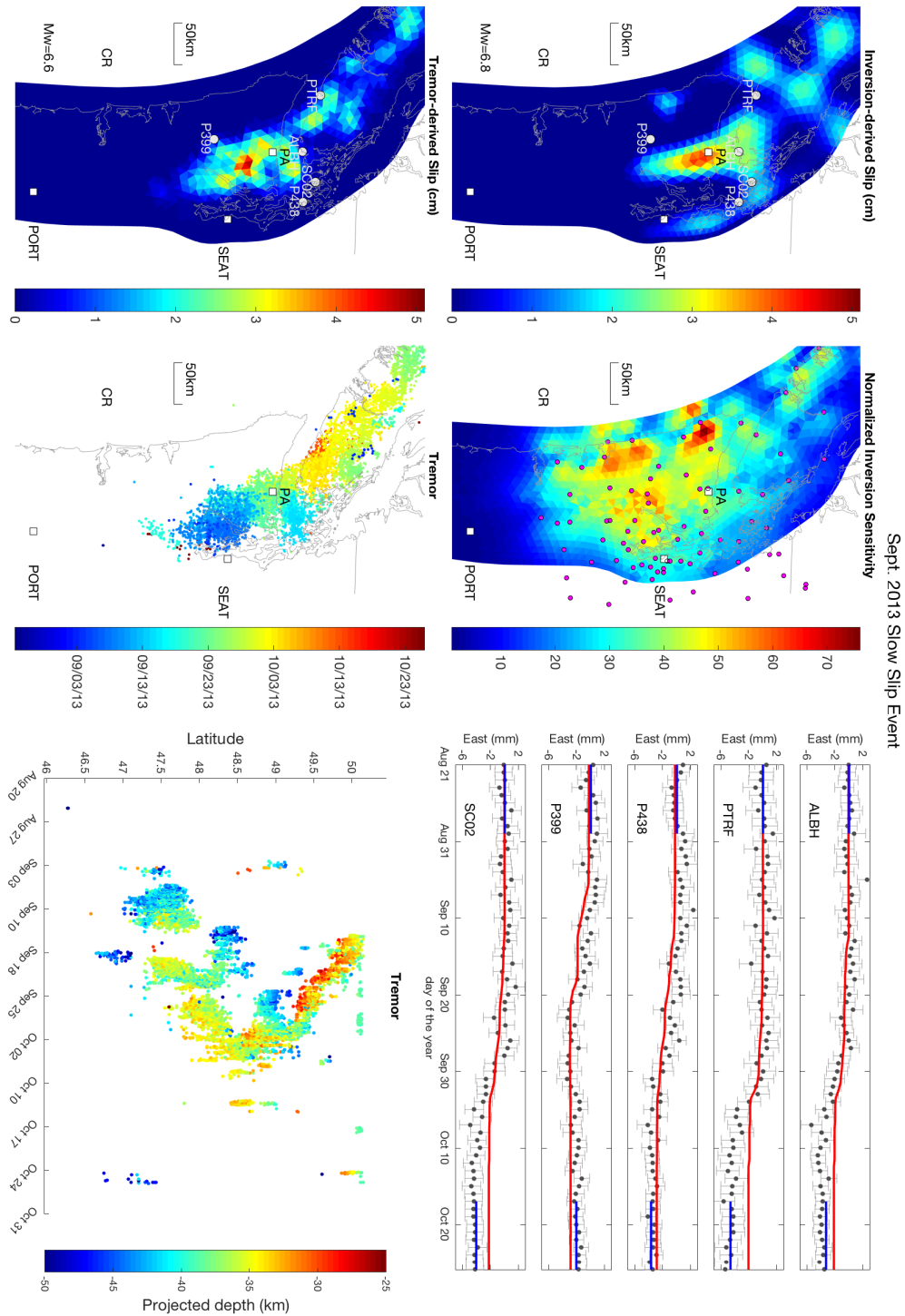


FIGURE B.7. 2013 Washington (September).

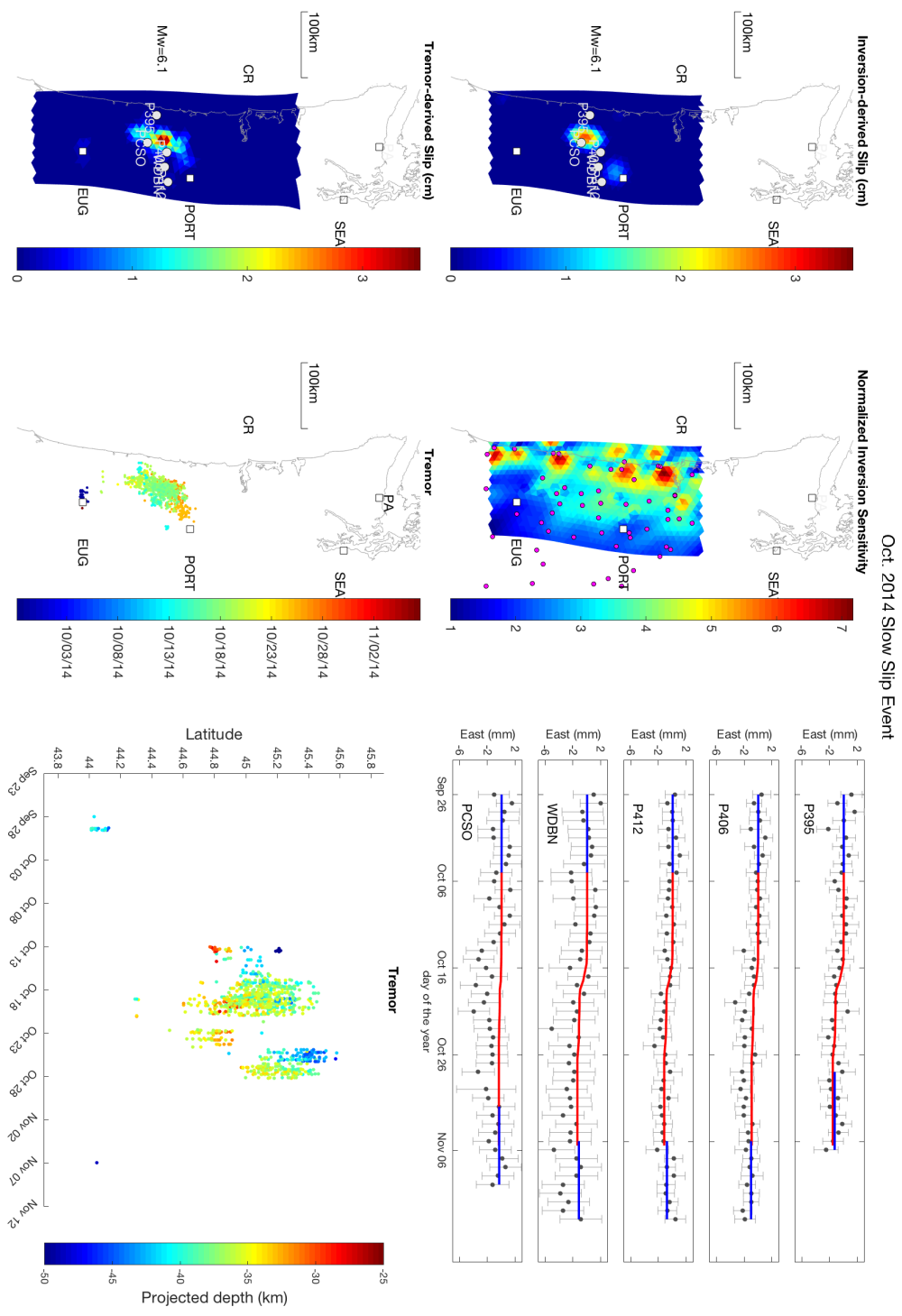


FIGURE B.8. 2014 Oregon (October).

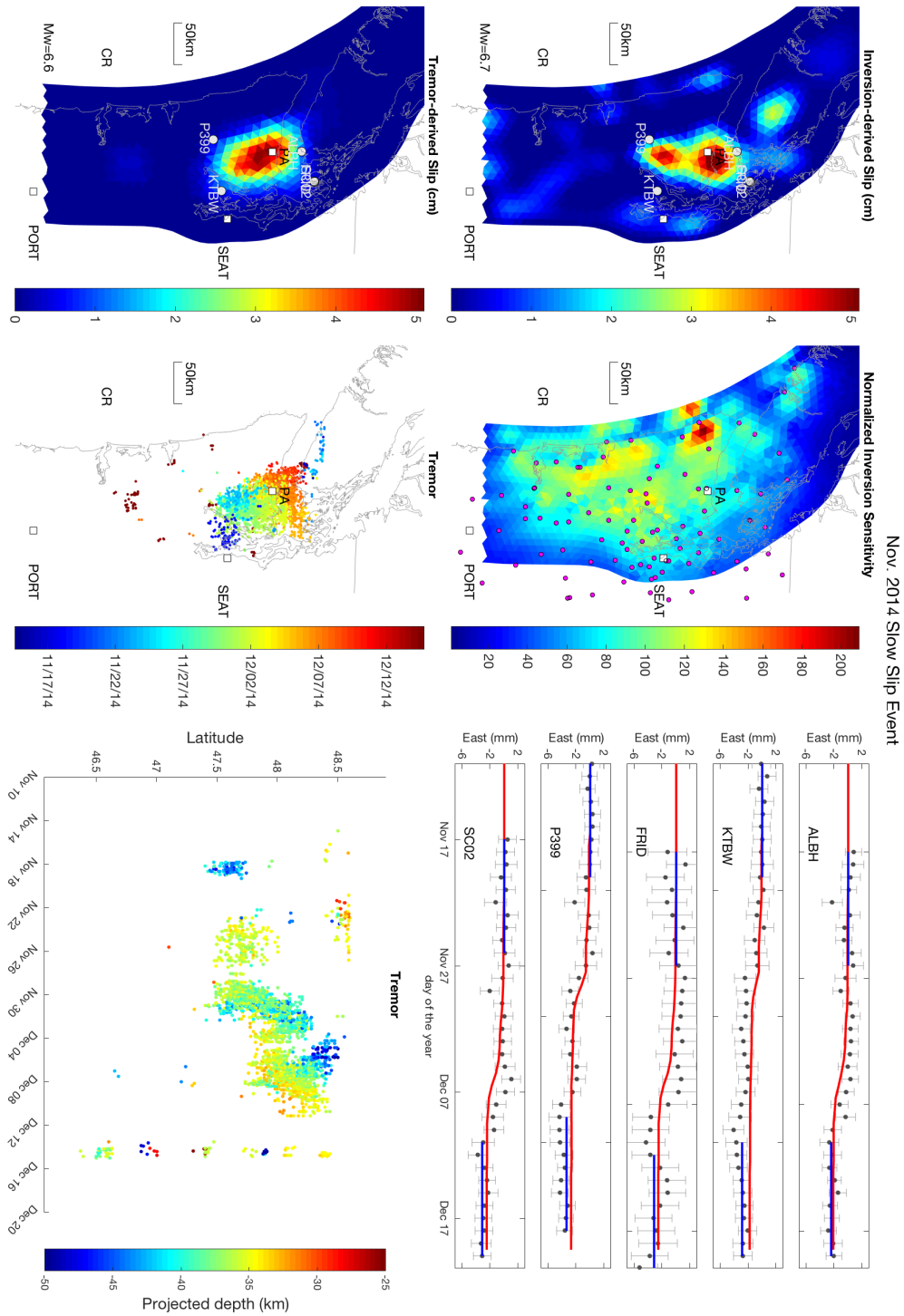


FIGURE B.9. 2014 Washington (November).

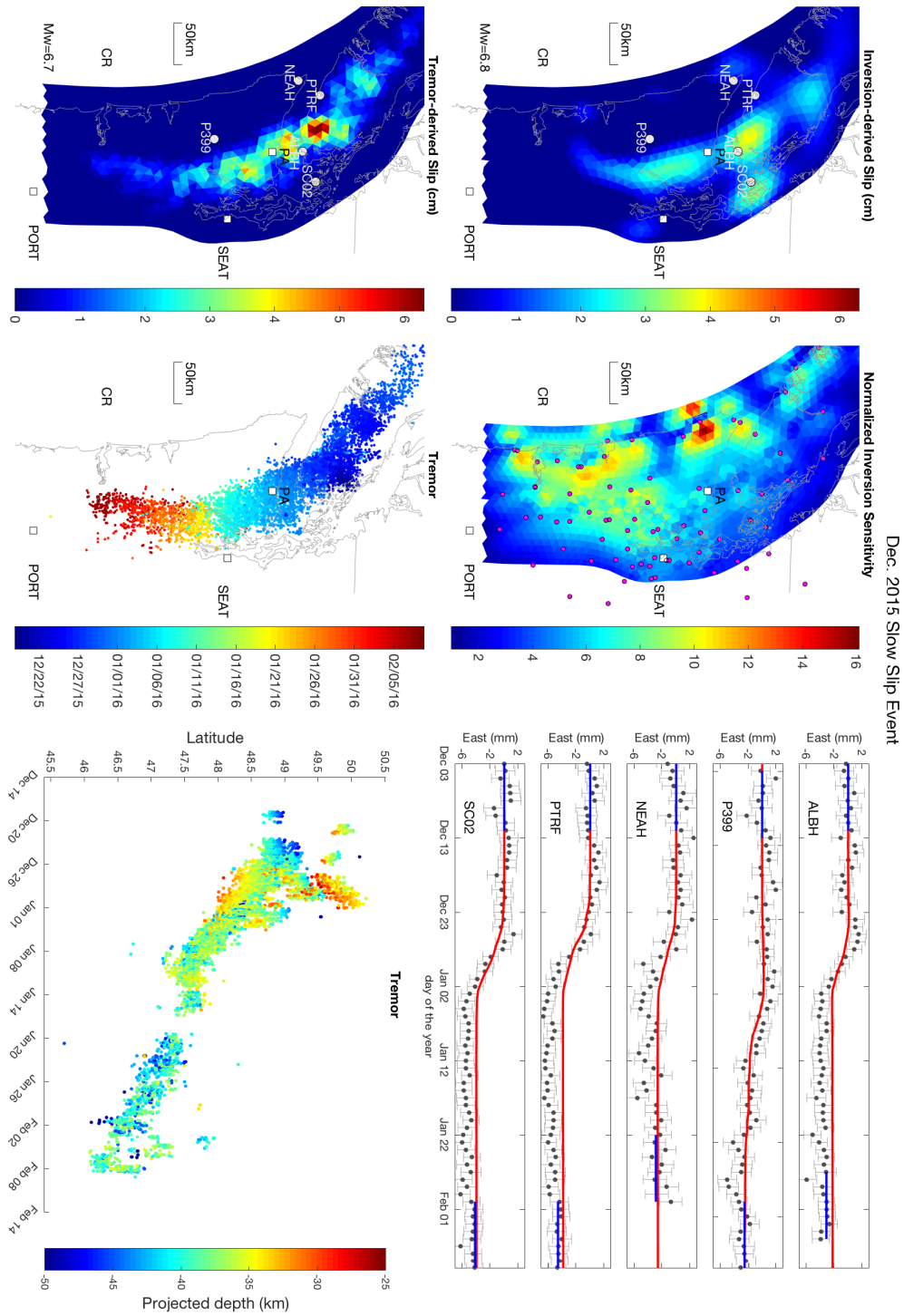


FIGURE B.10. 2015 Washington (December).

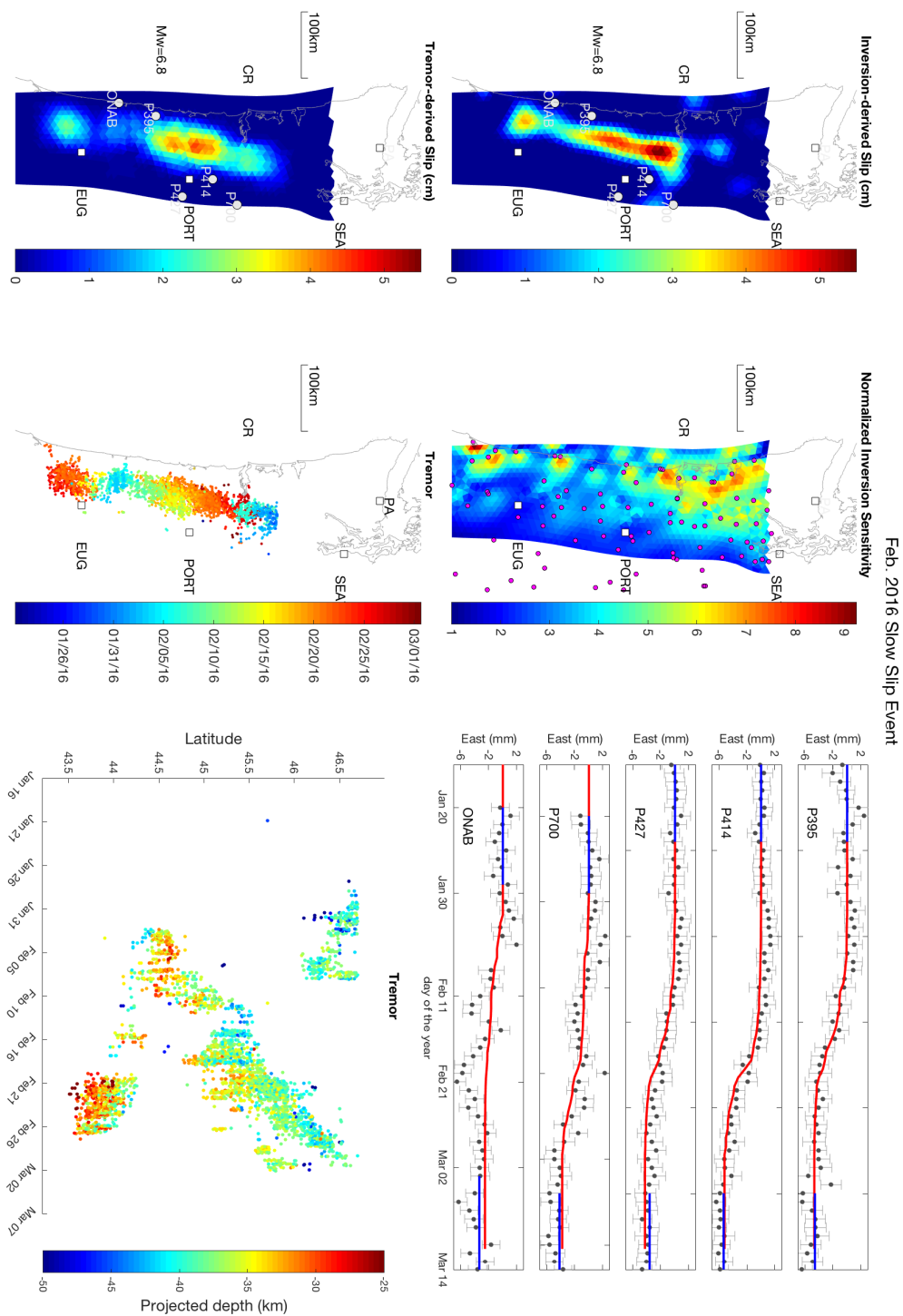


FIGURE B.11. 2016 Oregon (February).

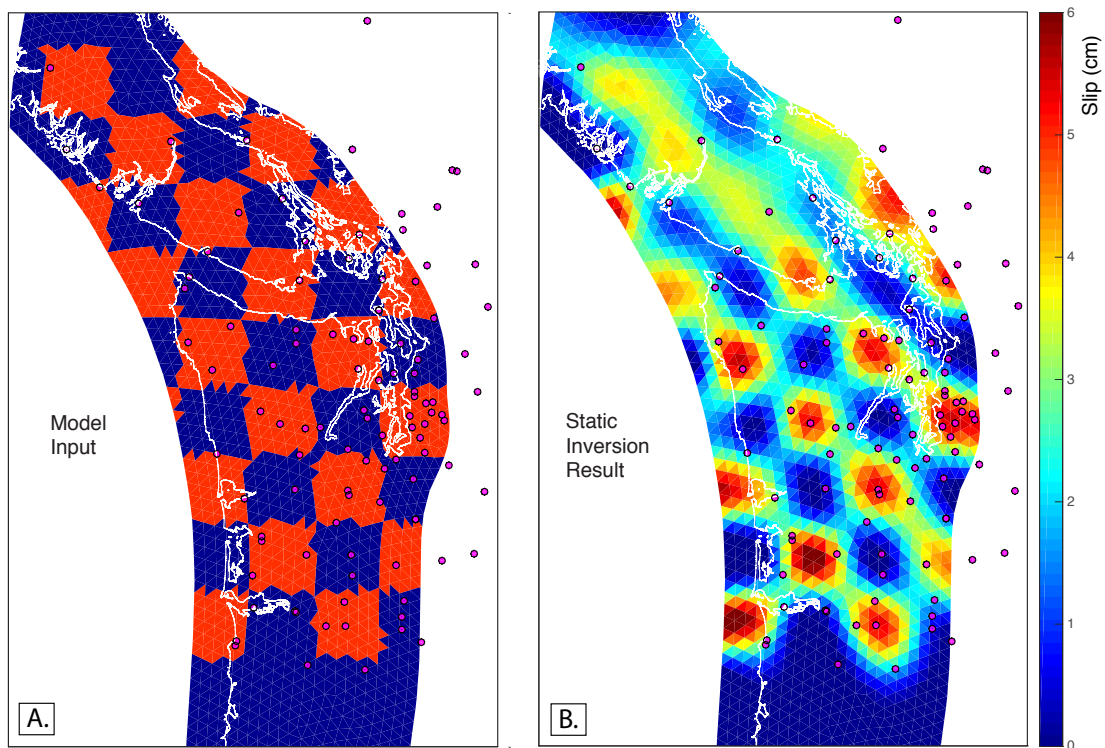


FIGURE B.12. Checkered board resolution test. Left panel is the input model. Right panel is the inversion result following the method described in Chapter 3. Magenta dots represent GPS stations used in the inversion.

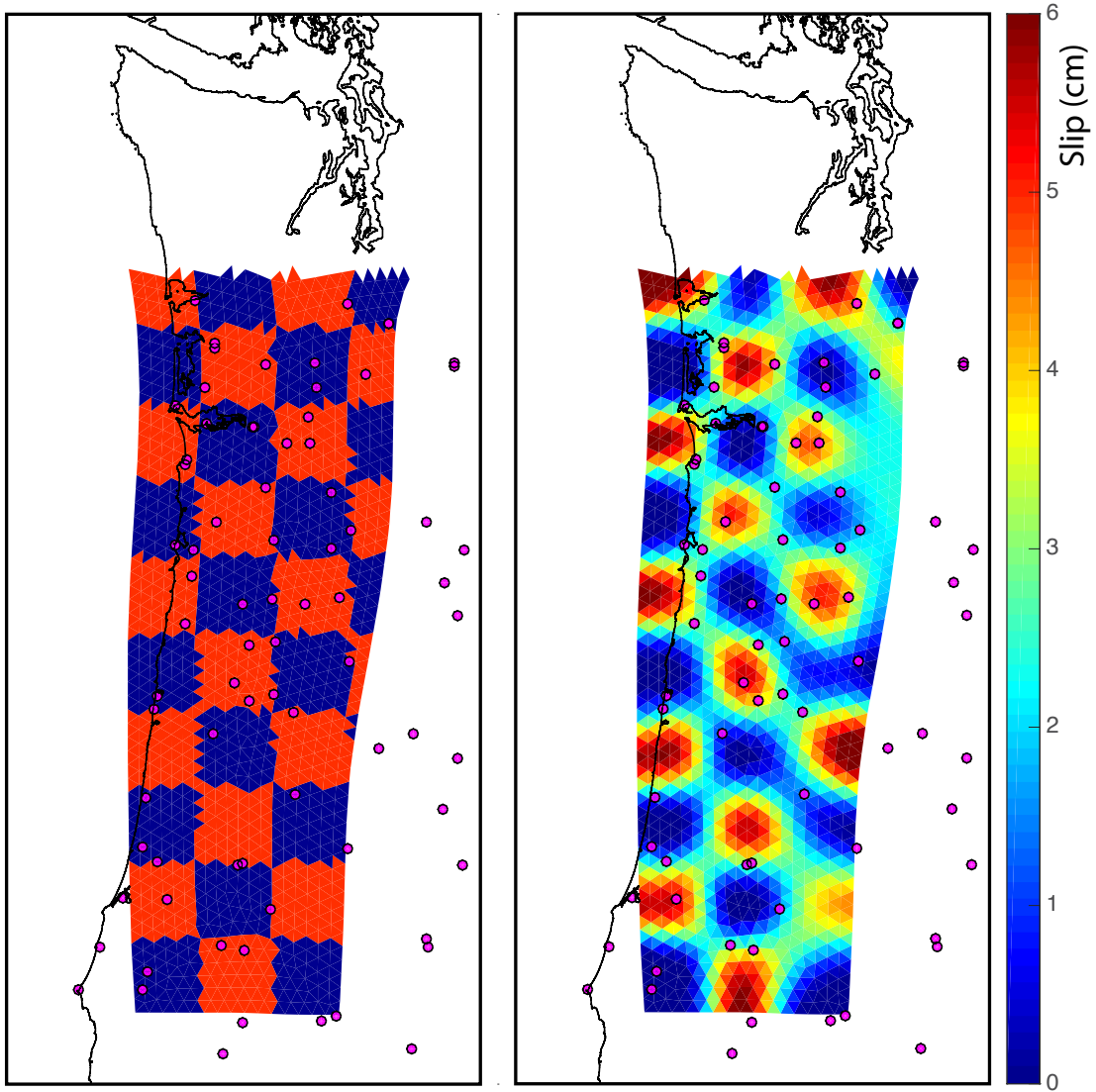


FIGURE B.13. Checkered board resolution test. Left panel is the input model. Right panel is the inversion result following the method described in Chapter 3. Magenta dots represent GPS stations used in the inversion.

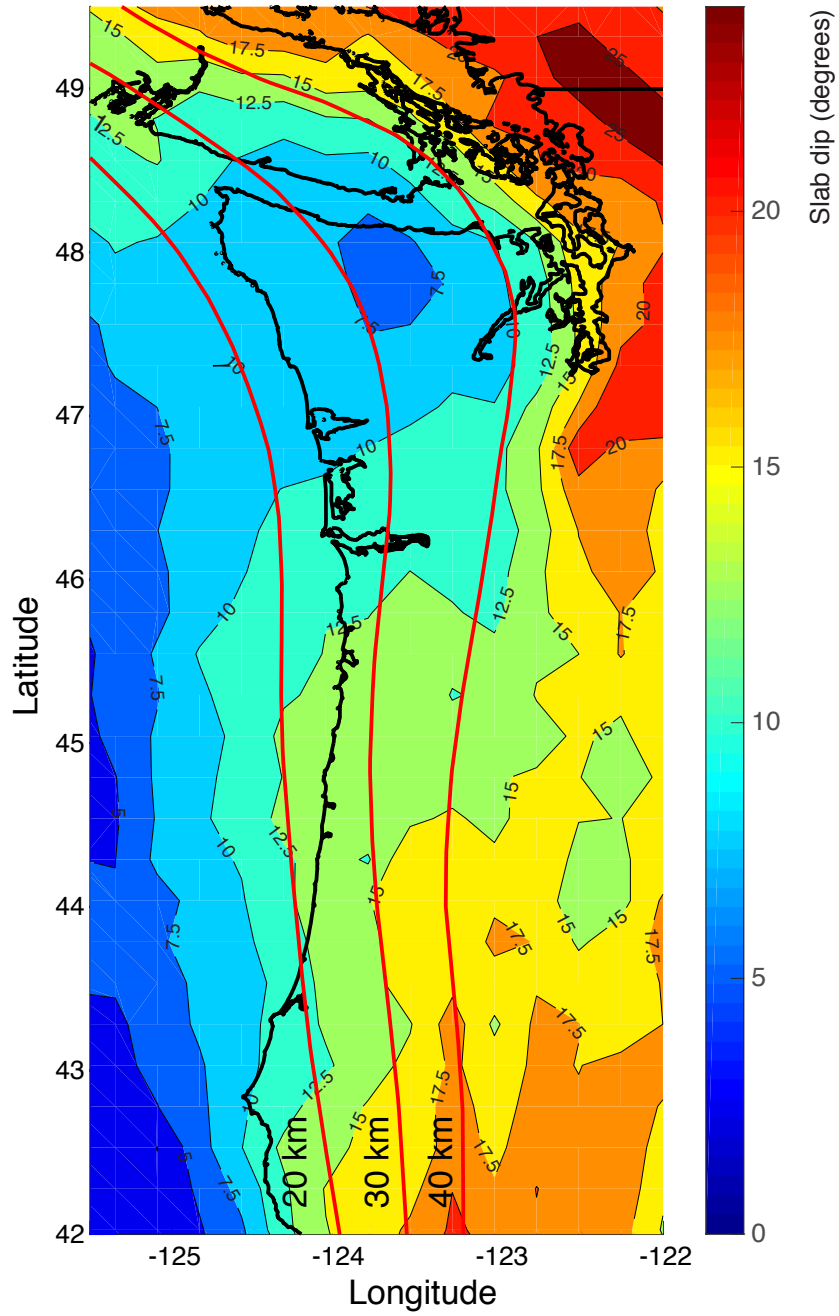


FIGURE B.14. Contour map of slab dip angle. Red lines represent depth contours of McCrory et al. (2012).

APPENDIX C

SUPPLEMENTARY MATERIAL FOR CHAPTER IV

This section contains the supplementary figures for Chapter IV.

C.1. Figures

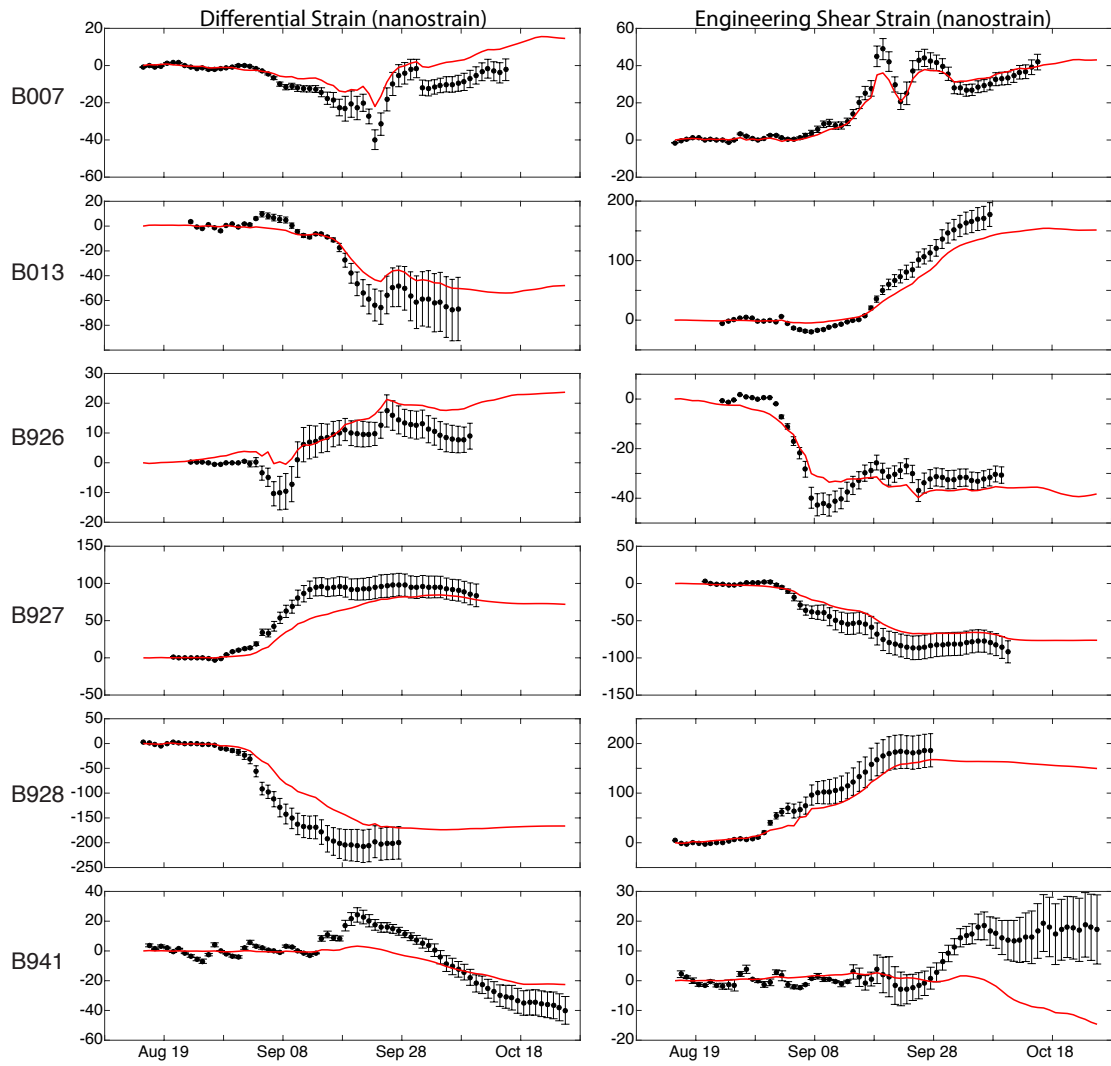


FIGURE C.1. Fits to strainmeter data with the joint inversion of the 2012 slow slip event not shown in figure 4.4.

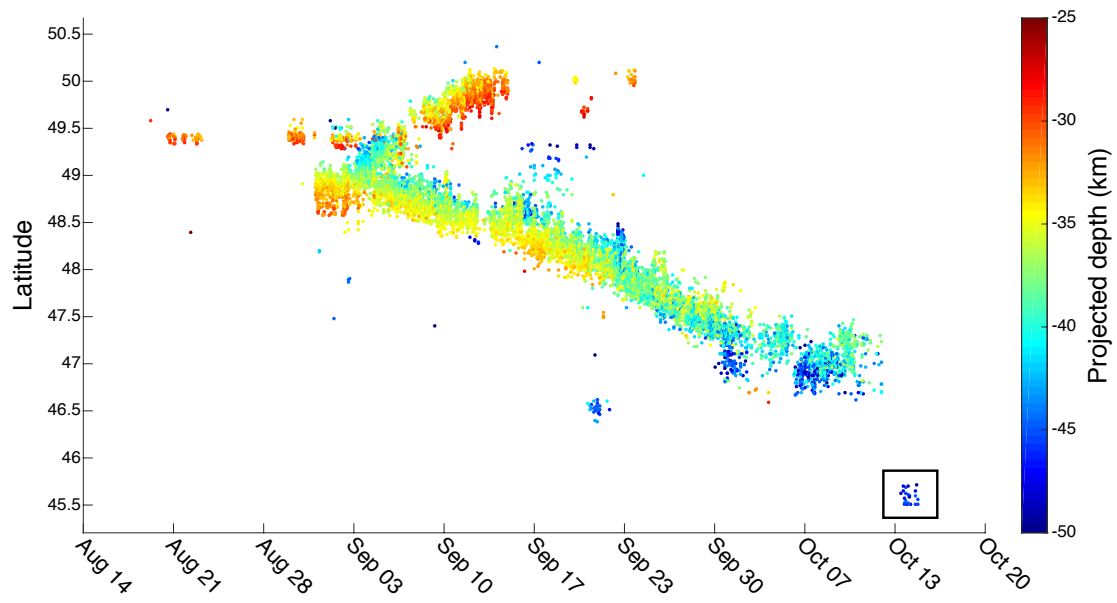


FIGURE C.2. Tremor data during the 2012 slow slip event in Cascadia. Colors represent the projected depth of tremor. Black box highlights tremor burst shown in figure 4.8.

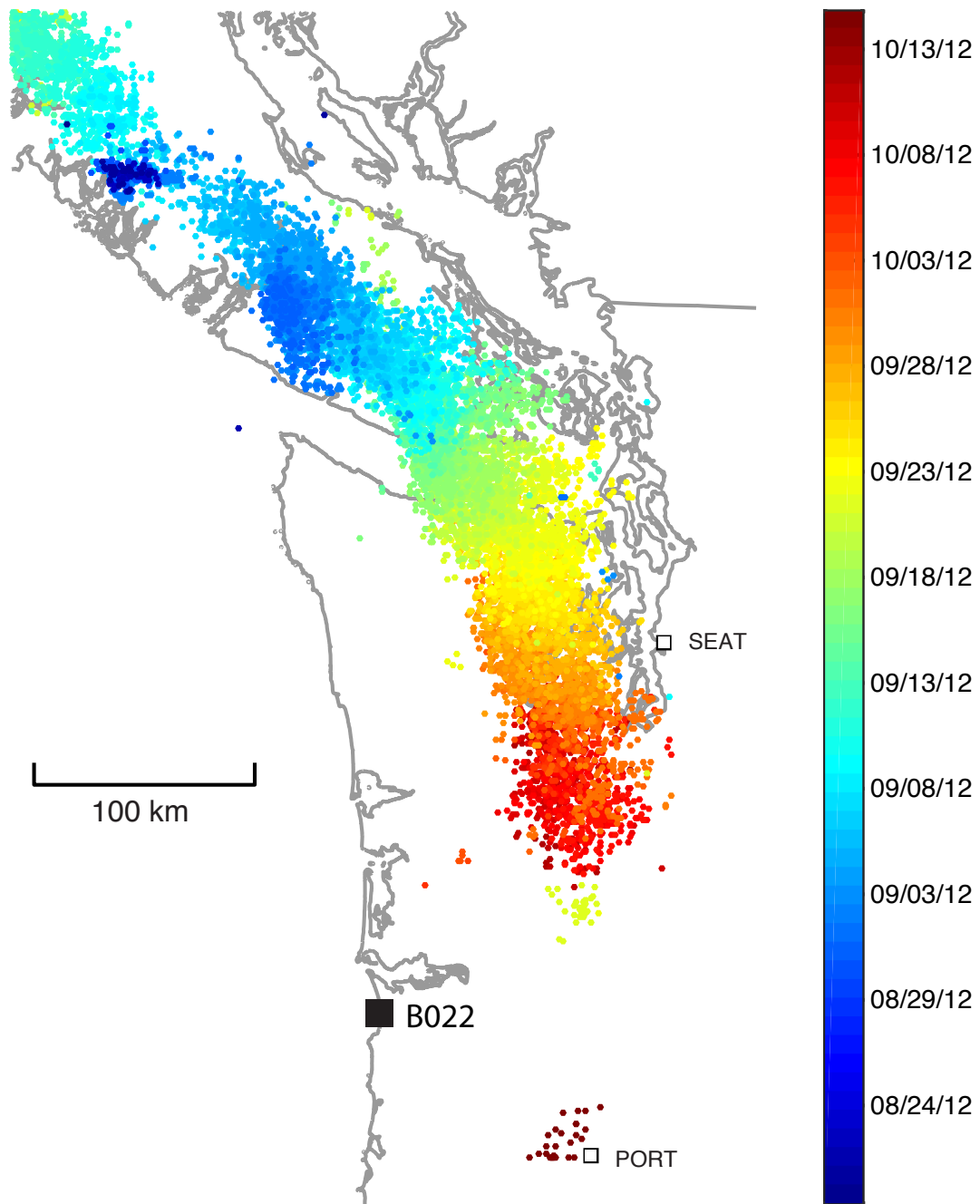


FIGURE C.3. Tremor data during the 2012 slow slip event. Colors represent the timing of individual tremor occurrences. Strainmeter B022 is shown in relation to tremor locations.

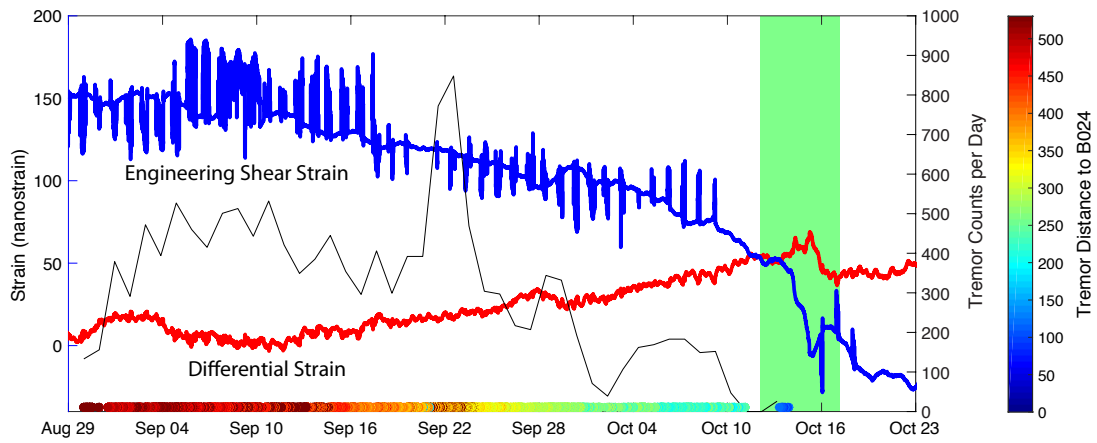


FIGURE C.4. Observed strain at strainmeter B024 during the 2012 slow slip event. Red and blue lines represent the differential and engineering shear strain components. Black line represents daily tremor activity. Colored dots along the x-axis show the distance of the tremor from B024. Green bar highlights increase in strain during a small burst of tremor.

REFERENCES CITED

- Agnew, D. C. (1992). The time-domain behavior of power-law noises. *Geophysical research letters*, 19(4):333–336.
- Agnew, D. C. (1996). Spotl: Some programs for oceantide loading. *SIO Ref. Ser.*, page 35.
- Agnew, D. C. (1997). Nloadf: A program for computing ocean-tide loading. *Journal of Geophysical Research: Solid Earth*, 102(B3):5109–5110.
- Aguiar, A. C., Melbourne, T. I., and Scrivner, C. W. (2009). Moment release rate of cascadia tremor constrained by gps. *Journal of Geophysical Research: Solid Earth*, 114(B7).
- Amiri-Simkooei, A., Tiberius, C., and Teunissen, s. P. (2007). Assessment of noise in gps coordinate time series: methodology and results. *Journal of Geophysical Research: Solid Earth*, 112(B7).
- Amoruso, A. and Crescentini, L. (2007). Inversion of levelling data: how important is error treatment? *Geophysical Journal International*, 171(3):1352–1362.
- Arndottir, T., Segall, P., and Matthews, M. (1992). Resolving the discrepancy between geodetic and seismic fault models for the 1989 loma prieta, california, earthquake. *Bulletin of the Seismological Society of America*, 82(5):2248–2255.
- Atwater, B. F. (1987). Evidence for great holocene earthquakes along the outer coast of washington state. *Science*, 236(4804):942–944.
- Audet, P., Bostock, M. G., Christensen, N. I., and Peacock, S. M. (2009). Seismic evidence for overpressured subducted oceanic crust and megathrust fault sealing. *Nature*, 457(7225):76–78.
- Barbour, A. J. and Agnew, D. C. (2011). Noise levels on plate boundary observatory borehole strainmeters in southern california. *Bulletin of the Seismological Society of America*, 101(5):2453–2466.
- Barbour, A. J., Agnew, D. C., and Wyatt, F. K. (2015). Coseismic strains on plate boundary observatory borehole strainmeters in southern california. *Bulletin of the Seismological Society of America*, 105(1):431–444.
- Bartlow, N. M., Miyazaki, S., Bradley, A. M., and Segall, P. (2011). Space-time correlation of slip and tremor during the 2009 cascadia slow slip event. *Geophysical Research Letters*, 38(18).

- Beroza, G. C. and Ide, S. (2011). Slow earthquakes and nonvolcanic tremor. *Annual review of Earth and planetary sciences*, 39:271–296.
- Bostock, M., Hyndman, R., Rondenay, S., and Peacock, S. (2002). An inverted continental moho and serpentinization of the forearc mantle. *Nature*, 417(6888):536–538.
- Bostock, M., Royer, A., Hearn, E., and Peacock, S. (2012). Low frequency earthquakes below southern vancouver island. *Geochemistry, Geophysics, Geosystems*, 13(11).
- Bostock, M., Thomas, A., Savard, G., Chuang, L., and Rubin, A. (2015). Magnitudes and moment-duration scaling of low-frequency earthquakes beneath southern vancouver island. *Journal of Geophysical Research: Solid Earth*, 120(9):6329–6350.
- Boyarko, D., Brudzinski, M., Porritt, R., Allen, R., and Tréhu, A. (2015). Automated detection and location of tectonic tremor along the entire cascadia margin from 2005 to 2011. *Earth and Planetary Science Letters*, 430:160–170.
- Brown, J. R., Beroza, G. C., Ide, S., Ohta, K., Shelly, D. R., Schwartz, S. Y., Rabbel, W., Thorwart, M., and Kao, H. (2009). Deep low-frequency earthquakes in tremor localize to the plate interface in multiple subduction zones. *Geophysical Research Letters*, 36(19).
- Brudzinski, M. R. and Allen, R. M. (2007). Segmentation in episodic tremor and slip all along cascadia. *Geology*, 35(10):907–910.
- Brudzinski, M. R., Hinojosa-Prieto, H. R., Schlanser, K. M., Cabral-Cano, E., Arciniega-Ceballos, A., Diaz-Molina, O., and DeMets, C. (2010). Nonvolcanic tremor along the oaxaca segment of the middle america subduction zone. *Journal of Geophysical Research: Solid Earth*, 115(B8).
- Burgette, R. J., Watson, C. S., Church, J. A., White, N. J., Tregoning, P., and Coleman, R. (2013). Characterizing and minimizing the effects of noise in tide gauge time series: relative and geocentric sea level rise around australia. *Geophysical Journal International*, page ggt131.
- Burgette, R. J., Weldon, R. J., and Schmidt, D. A. (2009). Interseismic uplift rates for western oregon and along-strike variation in locking on the cascadia subduction zone. *Journal of Geophysical Research: Solid Earth*, 114(B1).
- Calvert, A. J., Preston, L. A., and Farahbod, A. M. (2011). Sedimentary underplating at the cascadia mantle-wedge corner revealed by seismic imaging. *Nature Geoscience*, 4(8):545–548.

- Chapman, J. S. and Melbourne, T. I. (2009). Future cascadia megathrust rupture delineated by episodic tremor and slip. *Geophysical Research Letters*, 36(22).
- Chen, W.-P. and Molnar, P. (1983). Focal depths of intracontinental and intraplate earthquakes and their implications for the thermal and mechanical properties of the lithosphere. *Journal of Geophysical Research: Solid Earth*, 88(B5):4183–4214.
- Colella, H. V., Dieterich, J. H., and Richards-Dinger, K. (2013). Spatial and temporal patterns of simulated slow slip events on the cascadia megathrust. *Geophysical Research Letters*, 40(19):5101–5107.
- Delahaye, E., Townend, J., Reyners, M., and Rogers, G. (2009). Microseismicity but no tremor accompanying slow slip in the hikurangi subduction zone, new zealand. *Earth and Planetary Science Letters*, 277(1):21–28.
- Dragert, H. and Wang, K. (2011). Temporal evolution of an episodic tremor and slip event along the northern cascadia margin. *Journal of Geophysical Research: Solid Earth*, 116(B12).
- Dragert, H., Wang, K., and James, T. S. (2001). A silent slip event on the deeper cascadia subduction interface. *Science*, 292(5521):1525–1528.
- Frank, W., Shapiro, N., Husker, A., Kostoglodov, V., Bhat, H., and Campillo, M. (2015). Along-fault pore-pressure evolution during a slow-slip event in guerrero, mexico. *Earth and Planetary Science Letters*, 413:135–143.
- Gao, H., Humphreys, E. D., Yao, H., and van der Hilst, R. D. (2011). Crust and lithosphere structure of the northwestern us with ambient noise tomography: Terrane accretion and cascade arc development. *Earth and Planetary Science Letters*, 304(1):202–211.
- Ghosh, A., Vidale, J. E., and Creager, K. C. (2012). Tremor asperities in the transition zone control evolution of slow earthquakes. *Journal of Geophysical Research: Solid Earth*, 117(B10).
- Ghosh, A., Vidale, J. E., Sweet, J. R., Creager, K. C., and Wech, A. G. (2009). Tremor patches in cascadia revealed by seismic array analysis. *Geophysical Research Letters*, 36(17).
- Ghosh, A., Vidale, J. E., Sweet, J. R., Creager, K. C., Wech, A. G., and Houston, H. (2010a). Tremor bands sweep cascadia. *Geophysical Research Letters*, 37(8).
- Ghosh, A., Vidale, J. E., Sweet, J. R., Creager, K. C., Wech, A. G., Houston, H., and Brodsky, E. E. (2010b). Rapid, continuous streaking of tremor in cascadia. *Geochemistry, Geophysics, Geosystems*, 11(12).

- Gladwin, M. T. and Hart, R. (1985). Design parameters for borehole strain instrumentation. *pure and applied geophysics*, 123(1):59–80.
- Goldfinger, C., Nelson, C. H., and Johnson, J. E. (2003). Holocene earthquake records from the cascadia subduction zone and northern san andreas fault based on precise dating of offshore turbidites. *Annual Review of Earth and Planetary Sciences*, 31(1):555–577.
- Gomberg, J. et al. (2010). Slow-slip phenomena in cascadia from 2007 and beyond: A review. *Geological Society of America Bulletin*, 122(7-8):963–978.
- Grant, E. and Langston, C. (2009). Gladwin tensor strain-meter calibration and wave gradiometry applications. In *AGU Fall Meeting Abstracts*, volume 1, page 0070.
- Hart, R., Gladwin, M. T., Gwyther, R., Agnew, D. C., and Wyatt, F. K. (1996). Tidal calibration of borehole strain meters: Removing the effects of small-scale inhomogeneity. *Journal of Geophysical Research: Solid Earth*, 101(B11):25553–25571.
- Hawthorne, J. and Rubin, A. (2013). Short-time scale correlation between slow slip and tremor in cascadia. *Journal of Geophysical Research: Solid Earth*, 118(3):1316–1329.
- Hawthorne, J. C. and Rubin, A. M. (2010). Tidal modulation of slow slip in cascadia. *Journal of Geophysical Research: Solid Earth*, 115(B9).
- Hel-Or, Y. and Werman, M. (1996). Constraint fusion for recognition and localization of articulated objects. *International Journal of Computer Vision*, 19(1):5–28.
- Hiramatsu, Y., Watanabe, T., and Obara, K. (2008). Deep low-frequency tremors as a proxy for slip monitoring at plate interface. *Geophysical Research Letters*, 35(13).
- Hirose, H., Hirahara, K., Kimata, F., Fujii, N., and Miyazaki, S. (1999). A slow thrust slip event following the two 1996 hyuganada earthquakes beneath the bungo channel, southwest japan. *Geophysical Research Letters*, 26(21):3237–3240.
- Hirose, H. and Obara, K. (2005). Repeating short-and long-term slow slip events with deep tremor activity around the bungo channel region, southwest japan. *Earth, planets and space*, 57(10):961–972.
- Hodgkinson, K., Langbein, J., Henderson, B., Mencin, D., and Borsa, A. (2013). Tidal calibration of plate boundary observatory borehole strainmeters. *Journal of Geophysical Research: Solid Earth*, 118(1):447–458.

- Holtkamp, S. and Brudzinski, M. R. (2010). Determination of slow slip episodes and strain accumulation along the cascadia margin. *Journal of Geophysical Research: Solid Earth*, 115(B4).
- Houston, H., Delbridge, B. G., Wech, A. G., and Creager, K. C. (2011). Rapid tremor reversals in cascadia generated by a weakened plate interface. *Nature Geoscience*, 4(6):404–409.
- Husker, A. L., Kostoglodov, V., Cruz-Atienza, V. M., Legrand, D., Shapiro, N. M., Payero, J. S., Campillo, M., and Huesca-Pérez, E. (2012). Temporal variations of non-volcanic tremor (nvt) locations in the mexican subduction zone: Finding the nvt sweet spot. *Geochemistry, Geophysics, Geosystems*, 13(3).
- Hyndman, R. and Wang, K. (1995). The rupture zone of cascadia great earthquakes from current deformation and the thermal regime. *Journal of Geophysical Research: Solid Earth*, 100(B11):22133–22154.
- Ide, S., Beroza, G. C., Shelly, D. R., and Uchide, T. (2007). A scaling law for slow earthquakes. *Nature*, 447(7140):76–79.
- Ito, Y., Hino, R., Kido, M., Fujimoto, H., Osada, Y., Inazu, D., Ohta, Y., Inuma, T., Ohzono, M., Miura, S., et al. (2013). Episodic slow slip events in the japan subduction zone before the 2011 tohoku-oki earthquake. *Tectonophysics*, 600:14–26.
- Ito, Y., Obara, K., Shiomi, K., Sekine, S., and Hirose, H. (2007). Slow earthquakes coincident with episodic tremors and slow slip events. *Science*, 315(5811):503–506.
- Johnston, M. and Linde, A. (2002). 36 implications of crustal strain during conventional, slow, and silent earthquakes. *International Geophysics*, 81:589–605.
- Kato, A. and Nakagawa, S. (2014). Multiple slow-slip events during a foreshock sequence of the 2014 iquique, chile mw 8.1 earthquake. *Geophysical Research Letters*, 41(15):5420–5427.
- Kato, A., Obara, K., Igarashi, T., Tsuruoka, H., Nakagawa, S., and Hirata, N. (2012). Propagation of slow slip leading up to the 2011 mw 9.0 tohoku-oki earthquake. *Science*, 335(6069):705–708.
- Katsumata, A. and Kamaya, N. (2003). Low-frequency continuous tremor around the moho discontinuity away from volcanoes in the southwest japan. *Geophysical Research Letters*, 30(1).

- Kim, Y., Clayton, R., and Jackson, J. (2010). Geometry and seismic properties of the subducting cocos plate in central mexico. *Journal of Geophysical Research: Solid Earth*, 115(B6).
- Kostoglodov, V., Husker, A., Shapiro, N. M., Payero, J. S., Campillo, M., Cotte, N., and Clayton, R. (2010). The 2006 slow slip event and nonvolcanic tremor in the mexican subduction zone. *Geophysical Research Letters*, 37(24).
- Krogstad, R. D., Schmidt, D. A., Weldon, R. J., and Burgette, R. J. (2016). Constraints on accumulated strain near the ets zone along cascadia. *Earth and Planetary Science Letters*, 439:109–116.
- La Rocca, M., Creager, K. C., Galluzzo, D., Malone, S., Vidale, J. E., Sweet, J. R., and Wech, A. G. (2009). Cascadia tremor located near plate interface constrained by s minus p wave times. *Science*, 323(5914):620–623.
- Langbein, J. (2004). Noise in two-color electronic distance meter measurements revisited. *Journal of Geophysical Research: Solid Earth*, 109(B4).
- Langbein, J. (2008). Noise in gps displacement measurements from southern california and southern nevada. *Journal of Geophysical Research: Solid Earth*, 113(B5).
- Langbein, J. (2010). Effect of error in theoretical earth tide on calibration of borehole strainmeters. *Geophysical Research Letters*, 37(21).
- Langbein, J. (2012). Estimating rate uncertainty with maximum likelihood: differences between power-law and flicker–random-walk models. *Journal of Geodesy*, 86(9):775–783.
- Langbein, J. (2015). Borehole strainmeter measurements spanning the 2014 mw6.0 south napa earthquake, california: The effect from instrument calibration. *Journal of Geophysical Research: Solid Earth*, 120(10):7190–7202.
- Langbein, J. and Johnson, H. (1997). Correlated errors in geodetic time series: Implications for time-dependent deformation. *Journal of Geophysical Research: Solid Earth*, 102(B1):591–603.
- Lawson, C. L. and Hanson, R. J. (1995). *Solving least squares problems*, volume 15. SIAM.
- Loveless, J. P. and Meade, B. J. (2011). Spatial correlation of interseismic coupling and coseismic rupture extent of the 2011 mw= 9.0 tohoku-oki earthquake. *Geophysical Research Letters*, 38(17).
- Mao, A., Harrison, C. G., and Dixon, T. H. (1999). Noise in gps coordinate time series. *Journal of Geophysical Research: Solid Earth*, 104(B2):2797–2816.

- Mazzotti, S., Lambert, A., Courtier, N., Nykolaishen, L., and Dragert, H. (2007). Crustal uplift and sea level rise in northern cascadia from gps, absolute gravity, and tide gauge data. *Geophysical Research Letters*, 34(15).
- McCaffrey, R. (2009). Time-dependent inversion of three-component continuous gps for steady and transient sources in northern cascadia. *Geophysical Research Letters*, 36(7).
- McCaffrey, R., King, R. W., Payne, S. J., and Lancaster, M. (2013). Active tectonics of northwestern us inferred from gps-derived surface velocities. *Journal of Geophysical Research: Solid Earth*, 118(2):709–723.
- McCaffrey, R., Long, M. D., Goldfinger, C., Zwick, P. C., Nabelek, J. L., Johnson, C. K., and Smith, C. (2000). Rotation and plate locking at the southern cascadia subduction zone. *Geophysical Research Letters*, 27(19):3117–3120.
- McCrorry, P. A., Blair, J. L., Oppenheimer, D. H., and Walter, S. R. (2004). *Depth to the Juan de Fuca slab beneath the Cascadia subduction margin: A 3-D model for sorting earthquakes*. Citeseer.
- McCrorry, P. A., Blair, J. L., Waldhauser, F., and Oppenheimer, D. H. (2012). Juan de fuca slab geometry and its relation to wadati-benioff zone seismicity. *Journal of Geophysical Research: Solid Earth*, 117(B9).
- McCrorry, P. A., Hyndman, R. D., and Blair, J. L. (2014). Relationship between the cascadia fore-arc mantle wedge, nonvolcanic tremor, and the downdip limit of seismogenic rupture. *Geochemistry, Geophysics, Geosystems*, 15(4):1071–1095.
- McGuire, J. J. and Segall, P. (2003). Imaging of aseismic fault slip transients recorded by dense geodetic networks. *Geophysical Journal International*, 155(3):778–788.
- Melbourne, T. I., Szeliga, W. M., Miller, M. M., and Santillan, V. M. (2005). Extent and duration of the 2003 cascadia slow earthquake. *Geophysical Research Letters*, 32(4).
- Miller, M. M., Johnson, D. J., Rubin, C. M., Dragert, H., Wang, K., Qamar, A., and Goldfinger, C. (2001). Gps-determination of along-strike variation in cascadia margin kinematics: Implications for relative plate motion, subduction zone coupling, and permanent deformation. *Tectonics*, 20(2):161–176.
- Miller, M. M., Melbourne, T., Johnson, D. J., and Sumner, W. Q. (2002). Periodic slow earthquakes from the cascadia subduction zone. *Science*, 295(5564):2423–2423.

- Nedimović, M. R., Hyndman, R. D., Ramachandran, K., and Spence, G. D. (2003). Reflection signature of seismic and aseismic slip on the northern cascadia subduction interface. *Nature*, 424(6947):416–420.
- Nicholson, T., Bostock, M., and Cassidy, J. (2005). New constraints on subduction zone structure in northern cascadia. *Geophysical Journal International*, 161(3):849–859.
- Obara, K. (2002). Nonvolcanic deep tremor associated with subduction in southwest japan. *Science*, 296(5573):1679–1681.
- Obara, K., Tanaka, S., Maeda, T., and Matsuzawa, T. (2010). Depth-dependent activity of non-volcanic tremor in southwest japan. *Geophysical Research Letters*, 37(13).
- Ochi, T. and Kato, T. (2013). Depth extent of the long-term slow slip event in the tokai district, central japan: A new insight. *Journal of Geophysical Research: Solid Earth*, 118(9):4847–4860.
- Payero, J. S., Kostoglodov, V., Shapiro, N., Mikumo, T., Iglesias, A., Pérez-Campos, X., and Clayton, R. W. (2008). Nonvolcanic tremor observed in the mexican subduction zone. *Geophysical Research Letters*, 35(7).
- Peacock, S. M., Christensen, N. I., Bostock, M. G., and Audet, P. (2011). High pore pressures and porosity at 35 km depth in the cascadia subduction zone. *Geology*, 39(5):471–474.
- Peng, Z. and Gombert, J. (2010). An integrated perspective of the continuum between earthquakes and slow-slip phenomena. *Nature Geoscience*, 3(9):599–607.
- Petersen, M. D., Moschetti, M. P., Powers, P. M., Mueller, C. S., Haller, K. M., Frankel, A. D., Zeng, Y., Rezaeian, S., Harmsen, S. C., Boyd, O. S., et al. (2014). Documentation for the 2014 update of the united states national seismic hazard maps. Technical report, US Geological Survey.
- Peterson, C. L. and Christensen, D. H. (2009). Possible relationship between nonvolcanic tremor and the 1998–2001 slow slip event, south central alaska. *Journal of Geophysical Research: Solid Earth*, 114(B6).
- Pollitz, F. F., Bürgmann, R., and Segall, P. (1998). Joint estimation of afterslip rate and postseismic relaxation following the 1989 loma prieta earthquake. *Journal of Geophysical Research*, 103(B11):26–975.
- Reverso, T., Marsan, D., Helmstetter, A., and Enescu, B. (2016). Background seismicity in bosu peninsula, japan: Long-term acceleration, and relationship with slow slip events. *Geophysical Research Letters*.

- Roeloffs, E. (2010). Tidal calibration of plate boundary observatory borehole strainmeters: Roles of vertical and shear coupling. *Journal of Geophysical Research: Solid Earth*, 115(B6).
- Rogers, G. and Dragert, H. (2003). Episodic tremor and slip on the cascadia subduction zone: The chatter of silent slip. *Science*, 300(5627):1942–1943.
- Ruiz, S., Metois, M., Fuenzalida, A., Ruiz, J., Leyton, F., Grandin, R., Vigny, C., Madariaga, R., and Campos, J. (2014). Intense foreshocks and a slow slip event preceded the 2014 iquique mw 8.1 earthquake. *Science*, 345(6201):1165–1169.
- Savage, J., Svarc, J., Prescott, W., and Murray, M. (2000). Deformation across the forearc of the cascadia subduction zone at cape blanco, oregon. *Journal of Geophysical Research: Solid Earth*, 105(B2):3095–3102.
- Schmidt, D. and Gao, H. (2010). Source parameters and time-dependent slip distributions of slow slip events on the cascadia subduction zone from 1998 to 2008. *Journal of Geophysical Research: Solid Earth*, 115(B4).
- Schwartz, S. Y. and Rokosky, J. M. (2007). Slow slip events and seismic tremor at circum-pacific subduction zones. *Reviews of Geophysics*, 45(3).
- Segall, P., Burgmann, R., and Matthews, M. (2000). Time-dependent triggered afterslip following the 1989 loma prieta earthquake. *J. geophys. Res.*, 105(B3):5615–5634.
- Segall, P., Jónsson, S., and Agústsson, K. (2003). When is the strain in the meter the same as the strain in the rock? *Geophysical research letters*, 30(19).
- Segall, P. and Matthews, M. (1997). Time dependent inversion of geodetic data. *Journal of Geophysical Research*, 102:22–391.
- Segall, P., Rubin, A. M., Bradley, A. M., and Rice, J. R. (2010). Dilatant strengthening as a mechanism for slow slip events. *Journal of Geophysical Research: Solid Earth*, 115(B12).
- Shelly, D. R., Beroza, G. C., and Ide, S. (2007a). Complex evolution of transient slip derived from precise tremor locations in western shikoku, japan. *Geochemistry, Geophysics, Geosystems*, 8(10).
- Shelly, D. R., Beroza, G. C., and Ide, S. (2007b). Non-volcanic tremor and low-frequency earthquake swarms. *Nature*, 446(7133):305–307.
- Shelly, D. R., Beroza, G. C., Ide, S., and Nakamura, S. (2006). Low-frequency earthquakes in shikoku, japan, and their relationship to episodic tremor and slip. *Nature*, 442(7099):188–191.

- Szeliga, W., Melbourne, T., Santillan, M., and Miller, M. (2008). Gps constraints on 34 slow slip events within the cascadia subduction zone, 1997–2005. *Journal of Geophysical Research: Solid Earth*, 113(B4).
- Szeliga, W., Melbourne, T. I., Miller, M. M., and Santillan, V. M. (2004). Southern cascadia episodic slow earthquakes. *Geophysical Research Letters*, 31(16).
- Tamura, Y., Sato, T., Ooe, M., and Ishiguro, M. (1991). A procedure for tidal analysis with a bayesian information criterion. *Geophysical Journal International*, 104(3):507–516.
- Taylor, J. (1997). *Introduction to error analysis, the study of uncertainties in physical measurements*, volume 1.
- Thomas, A. L. (1993). *Poly3D: A three-dimensional, polygonal element, displacement discontinuity boundary element computer program with applications to fractures, faults, and cavities in the Earth's crust*. PhD thesis, Stanford University.
- Uchida, N. and Matsuzawa, T. (2013). Pre-and postseismic slow slip surrounding the 2011 tohoku-oki earthquake rupture. *Earth and Planetary Science Letters*, 374:81–91.
- Vallee, M., Nocquet, J.-M., Battaglia, J., Font, Y., Segovia, M., Regnier, M., Mothes, P., Jarrin, P., Cisneros, D., Vaca, S., et al. (2013). Intense interface seismicity triggered by a shallow slow slip event in the central ecuador subduction zone. *Journal of Geophysical Research: Solid Earth*, 118(6):2965–2981.
- Verdonck, D. (2005). An inverse dislocation model of surface deformation in western washington. *Tectonophysics*, 395(3):179–191.
- Vidale, J. E., Hotovec, A. J., Ghosh, A., Creager, K. C., and Gombert, J. (2011). Tiny intraplate earthquakes triggered by nearby episodic tremor and slip in cascadia. *Geochemistry, Geophysics, Geosystems*, 12(6).
- Wang, K., Dragert, H., Kao, H., and Roeloffs, E. (2008). Characterizing an uncharacteristic ets event in northern cascadia. *Geophysical Research Letters*, 35(15).
- Wang, K., He, J., Dragert, H., and James, T. S. (2001). Three-dimensional viscoelastic interseismic deformation model for the cascadia subduction zone. *Earth, Planets and Space*, 53(4):295–306.
- Wang, K., Wells, R., Mazzotti, S., Hyndman, R. D., and Sagiya, T. (2003). A revised dislocation model of interseismic deformation of the cascadia subduction zone. *Journal of Geophysical Research: Solid Earth*, 108(B1).

- Wdowinski, S., Bock, Y., Zhang, J., Fang, P., and Genrich, J. (1997). Southern california permanent gps geodetic array: Spatial filtering of daily positions for estimating coseismic and postseismic displacements induced by the 1992 landers earthquake. *Journal of Geophysical Research: Solid Earth*, 102(B8):18057–18070.
- Wech, A. G. (2010). Interactive tremor monitoring. *Seismological Research Letters*, 81(4):664–669.
- Wech, A. G. and Bartlow, N. M. (2014). Slip rate and tremor genesis in cascadia. *Geophysical Research Letters*, 41(2):392–398.
- Wech, A. G. and Creager, K. C. (2008). Automated detection and location of cascadia tremor. *Geophysical Research Letters*, 35(20).
- Wech, A. G. and Creager, K. C. (2011). A continuum of stress, strength and slip in the cascadia subduction zone. *Nature Geoscience*, 4(9):624–628.
- Wech, A. G., Creager, K. C., and Melbourne, T. I. (2009). Seismic and geodetic constraints on cascadia slow slip. *Journal of Geophysical Research: Solid Earth*, 114(B10).
- Wells, R. E. and Simpson, R. W. (2001). Northward migration of the cascadia forearc in the northwestern us and implications for subduction deformation. *Earth, Planets and Space*, 53(4):275–283.
- Williams, C. A. and Wallace, L. M. (2015). Effects of material property variations on slip estimates for subduction interface slow-slip events. *Geophysical Research Letters*, 42(4):1113–1121.
- Williams, S. D., Bock, Y., Fang, P., Jamason, P., Nikolaidis, R. M., Prawirodirdjo, L., Miller, M., and Johnson, D. J. (2004). Error analysis of continuous gps position time series. *Journal of Geophysical Research: Solid Earth*, 109(B3).
- Wyatt, F. (1989). Displacement of surface monuments- vertical motion. *Journal of Geophysical Research*, 94:1655–1664.
- Zhang, J., Bock, Y., Johnson, H., Fang, P., Williams, S., Genrich, J., Wdowinski, S., and Behr, J. (1997). Southern california permanent gps geodetic array: Error analysis of daily position estimates and site velocities. *Journal of Geophysical Research: Solid Earth*, 102(B8):18035–18055.